Radar Sensitivity and Antenna Scan Pattern Study for a Satellite-Based Radar Wind Sounder (RAWS)

Michael A. Stuart

Radar Systems and Remote Sensing Laboratory
University of Kansas Center for Research, Inc.
2291 Irving Hill Road,Lawrence, Kansas 66045-2969
913/864-4835 * FAX: 913/864-7789 * OMNET: KANSAS.U.RSL * TELEX: 706352

RSL Technical Report 9550-2

November 1992

Supported by:

NASA Marshall Space Flight Center
Marshall Space Flight Center AL 35812

Grant NAG8-893

Radar Sensitivity and Antenna Scan Pattern Study for a Satellite Based Radar Wind Sounder (RAWS)

by

Michael A. Stuart

B.S.E.E., Texas Tech University, Lubbock, Texas, 1985
M.S.E.E., University of Kansas, 1992

TABLE OF CONTENTS

LIST OF FIGURES

LIST OF TABLES

ABSTRACT

Modeling global atmospheric circulations and forecasting the weather would improve greatly if worldwide information on winds aloft were available. Recognition of this led to the inclusion of the LAser Wind Sounder (LAWS) system to measure Doppler shifts from aerosols in the planned for Earth Observation System (EOS) [Curran, 1987]. However, gaps will exist in LAWS coverage where heavy clouds are present. The RAdar Wind Sensor (RAWS) is an instrument that could fill these gaps by measuring Doppler shifts from clouds and rain.

Previous studies conducted at the University of Kansas show RAWS as a feasible instrument. This thesis pertains to the signal-to-noise ratio (SNR) sensitivity, transmit waveform, and limitations to the antenna scan pattern of the RAWS system. A drop-size distribution model is selected and applied to the radar range equation for the sensitivity analysis. Six frequencies are used in computing the SNR for several cloud types to determine the optimal transmit frequency. The results show the use of two frequencies, one higher frequency (94 GHz) to obtain sensitivity for thinner cloud, and a lower frequency (24 GHz) for better penetration in rain, provide ample SNR.

The waveform design supports covariance estimation processing. This estimator eliminates the Doppler ambiguities compounded by the selection of such high transmit frequencies, while providing an estimate of the mean frequency. The unambiguous range and velocity computation shows them to be within acceptable limits.

After defining the waveform and computing the standard deviation of the estimator, the scan pattern limitations are given. Wind-measurement error, comprised of velocity uncertainty and antenna pointing errors, is determined for three antenna scan patterns. The design goal for the RAWS system is to limit the wind-speed error to less than 1 ms^{-1}. Due to linear dependence between vectors for a three-vector scan pattern, a reasonable wind-speed error is unattainable. Only the two-vector scan pattern falls within the wind-error limits for azimuth angles between 16° to 70°. However, this scan only allows two components of the wind to be determined. As a result, a technique is then shown, based on the *Z-R-V* relationships, that permits the vertical component (i.e., rain) to be computed. Thus the horizontal wind components may be obtained from the covariance estimator and the vertical component from the reflectivity factor.

Finally, a new candidate system is introduced which summarizes the parameters taken from previous RAWS studies, or those modified in this thesis.

CHAPTER 1

INTRODUCTION

1.1 HISTORY OF RADAR AND APPLICATIONS

Over the past 50 years, radar technology has grown far beyond the meaning of the acronym: RAdar Detection And Ranging. The development of radar stemmed from the necessity for accurate navigation and long range detection of enemy targets during the second world war. The first radars utilized an unmodulated continuous wave (CW) waveform that provided only Doppler information. These experimental radars detected the interference produced between the direct signal received from the transmitter and the Doppler-frequency-shifted signal reflected by a moving target [Skolnik, 1980]. The need for accurate range information was realized early and more sophisticated modulation techniques, such as frequency modulation CW (FM-CW) and pulsed CW, were implemented. These techniques gave rise to the moving target indicator (MTI) and synthetic aperture (SAR) radars for detecting moving targets and increasing cross-range resolution, respectively. Although radar was originally developed to satisfy surveillance and weapon control requirements for the military, there have been significant civil applications for the safe travel of aircraft, ships, and spacecraft; the remote sensing of the environment, especially the weather; and law enforcement, as well as many other applications. The use of pulse-Doppler radar technology, using modern digital signal-processing and advanced display technology, has advanced to the point where the United States is replacing its existing non-Doppler weather radar network with a next-generation Doppler system (NEXRAD). This system will provide quantitative and automated real-time information on storms, precipitation, hurricanes, tornadoes, and a host of other important weather phenomena [Skolnik, 1990]. In research areas, numerous ground-based VHF and UHF Doppler radar systems are measuring turbulence and local wind, while some microwave radar systems are measuring cloud returns [Lhermitte, 1988]. However, few space-borne Doppler radar systems have been studied for global wind measurement purposes.

1.2 WEATHER PREDICTION

Accurate prediction of weather is important to agriculture, transportation, flood control, and many other industries. Global system models relevant to climate are assuming increasing importance. Current global atmospheric models use pressure measurements and thermodynamic properties to calculate the effects of wind for use in Numerical Weather Prediction (NWP) models. Inputs to the NWP models are temperature, pressure and wind at different heights. However, direct wind measurements could significantly improve the NWP model performance [Kalnay, 1985]. Global twice-daily measurements, with the accuracies and resolutions summarized in Table 1.1, would result in more accurate medium-range (up to five days) forecasts in the Northern Hemisphere, where most of the conventional, ground-based, wind sensors (rawinsonde network) operate. In the Southern Hemisphere, where ground-based sensors are scarce because of the larger ocean areas, major improvements are possible [Baker, 1985].

Table 1.1 Global and synoptic scale observational requirements.

Horizontal resolution	100 km (meso-α scale)
Vertical resolution	1 km (0.5 km in boundary layer and in the vicinity of the jet stream)
Temporal resolution	6 hours
Accuracy of the wind component	1-2 m/s in lower troposphere 2-5 m/s in upper troposphere
Directional accuracy	± 10 degrees

Table 1.2 presents characteristics of four cloud classifications. Both the widespread irregular stirring and regular ascent cloud classes, characterized by a large horizontal extent, support the immense resolution cells as given in Table 1.1.

Today's operational wind-velocity observing systems are fixed on the ground or on towers, and mobile on ships, aircraft or balloons. These techniques are limited to local observations that do not lend themselves to a global perspective. Global-scale

Table 1.2 Principal classes of clouds [Mason, 1957].

Kind of vertical motion	*Typical vertical speed (cm sec^{-1})*	*Kind of cloud*	*Name in international cloud classification*	*Typical horizontal extent (km)*	*Typical thickness (km)*	*Typical life of particles (min)*	*Typical kind of precipitation*
Orographic disturbances	10^2–10^3	Lenticular or wave clouds	Species 'lenticularis'	10 occasionally up to 10^2	1 occasionally up to 10	10 occasionally up to 10^2	nil occasional intensification of existing precipitation
Widespread irregular stirring	1–10	Low-level, shallow layer clouds, fog	Stratus, stratocumulus	10^2–10^3	< 1	10^2 ?	nil, or slight snow or drizzle
Widespread regular ascent	5–20	Multi-layer clouds, continuous in precipitation	Cirrus, cirrostratus, altostratus, altocumulus, nimbostratus	10^3	Individually 1, in precipitation 10	up to 10^3	Prolonged moderate snow or rain
Local penetrative convection	1–5.10^2 3–20.10^2	Cumuliform clouds	Cumulus, cumulonimbus	1 10	1 10	10 20	nil Showers of rain, hail, or snow (thunderstorms)

measurements require satellite-based systems. The laser atmospheric wind sounder (LAWS) was proposed for this purpose as part of the EOS. The LAWS system will determine the wind-vector by measuring the Doppler shift of the signal scattered from aerosols in the atmosphere with a conically scanned optical sensor. Successive measurements from different directions will provide global coverage of wind-vector profiles throughout the troposphere. These measurements will have a spatial scale of 100 km by 100 km at 1 km height intervals, and an expected accuracy of better than 1 ms^{-1} [Curran, 1987]. If, however, dense clouds are present, LAWS will be unable to measure the winds below the cloud tops. Thus an instrument that can penetrate clouds is necessary and is the basis for the radar wind sounder (RAWS). Although a feasible satellite radar cannot measure the winds in clear air as does LAWS, it can measure Doppler shifts of the reflections from hydrometeors that form the clouds. With the RAWS and LAWS systems operating in tandem, the measurement of wind vectors in both clear and cloudy conditions would be possible. Moreover, RAWS can be used in the role of measuring rain rates (like TRMM), and ocean-surface winds (like N-SCATT and ERS-1).

1.3 THE RADAR WIND SOUNDER

The RAWS study pertains to the trade-offs involved in designing a satellite-borne radar to measure wind vectors. The primary tasks related to the RAWS study are to determine:

1 - scattering and attenuation models,
2 - required radar sensitivity,
3 - optimal frequencies,
4 - needed antenna size,
5 - suitable scan pattern,
6 - removal of the ambiguity imposed by range and Doppler-frequency sizes,
7 - spectrum measurements,
8 - system configuration,
9 - performance as a rain sensor,
10 - performance as an ocean-surface wind sensor.

Previous efforts were accomplished by two University of Kansas graduate students: Weizhaung Xin [Xin, 1990] and Tim Propp. Xin studied items 1-6, to a lesser degree item 7, and developed a candidate system selected after preliminary study of frequencies and sensitivities. The candidate system parameters are shown in Table 1.3.

Table 1.3 Original RAWS candidate system parameters.

Altitude	830 km
Target Volume Coverage	100 km x 100 km x 20 km
Look Angles (from vertical)	30° and 35°
PRF	3500 Hz
Transmit Frequencies	10 GHz and 35 GHz
Pulse Width (Compressed)	1 μsec
Time-Bandwidth Product	20
Antenna Diameter	8 m
Scan Period	10 sec
Vertical Resolution	2 km (10 GHz) and 1 km (35 GHz)
Peak Power	3000 W
Receiver Noise Figure	4 dB
Transmitter Losses	1.5 dB
Receiver Losses	1.5 dB
Spacecraft Speed	7.5 km/s

Xin analyzed two frequencies that allowed for higher sensitivity for clouds (35 GHz) and more penetration for rain (10 GHz). The power was selected to be on the order of that used in current and planned space-borne SARs. The antenna size was selected large enough to allow reasonable vertical resolution in clouds and rain, along with adequate resolution of individual cells. An orbit height was chosen that would give a reasonable coverage swath. Although a lower orbit would allow more sensitive measurements, a higher one would produce a wider swath. The need for three independent measurements to compute all three components of the wind (and rain) vector led to the use of a conical scan pattern with beams at two depression angles, allowing four observations per scan. Figure 1.1 illustrates the scan pattern. Xin concluded that the antenna scan would require an electronic squint to obtain a sufficient number of samples while reducing the effects of decorrelation.

Xin also studied several waveforms and estimators to eliminate the range and Doppler ambiguities while providing an accurate first moment (mean frequency) estimate. Xin concluded that a covariance estimator with a special modulated pulse-pair waveform produced the least error. The modulation required the first pulse of the pulse-pair to be up-chirped while the second pulse was down-chirped. The chirp modulation allowed the receiver to distinguish between the two pulses permitting the pulse-pair to remain unambiguous in range provided the inter-pair spacing was large enough.

Propp continued the analysis of the RAWS program by conducting a detailed study of the radar sensitivity issue. He began by searching for an accurate cloud drop-size distribution model to be used in the radar sensitivity calculations. From this literature search, the Deirmendjian distribution model was chosen and used in a system signal-to-noise ratio (SNR) computer program written by Propp. The results generated for this thesis are based on a modified version of Propp's SNR program.

1.4 OUTLINE

This thesis concludes the satellite-based Doppler radar sensitivity analysis and further defines the antenna scan pattern. Building on the efforts of Xin and Propp, the key issues presented include:

- verification of Deirmendjian model with available measured data,
- validation of the Rayleigh criterion,
- inclusion of atmospheric gas attenuation in SNR program,
- selection of optimal frequency(s),
- study of waveform parameters to minimize range and Doppler ambiguities,
- study of optimal scan pattern.

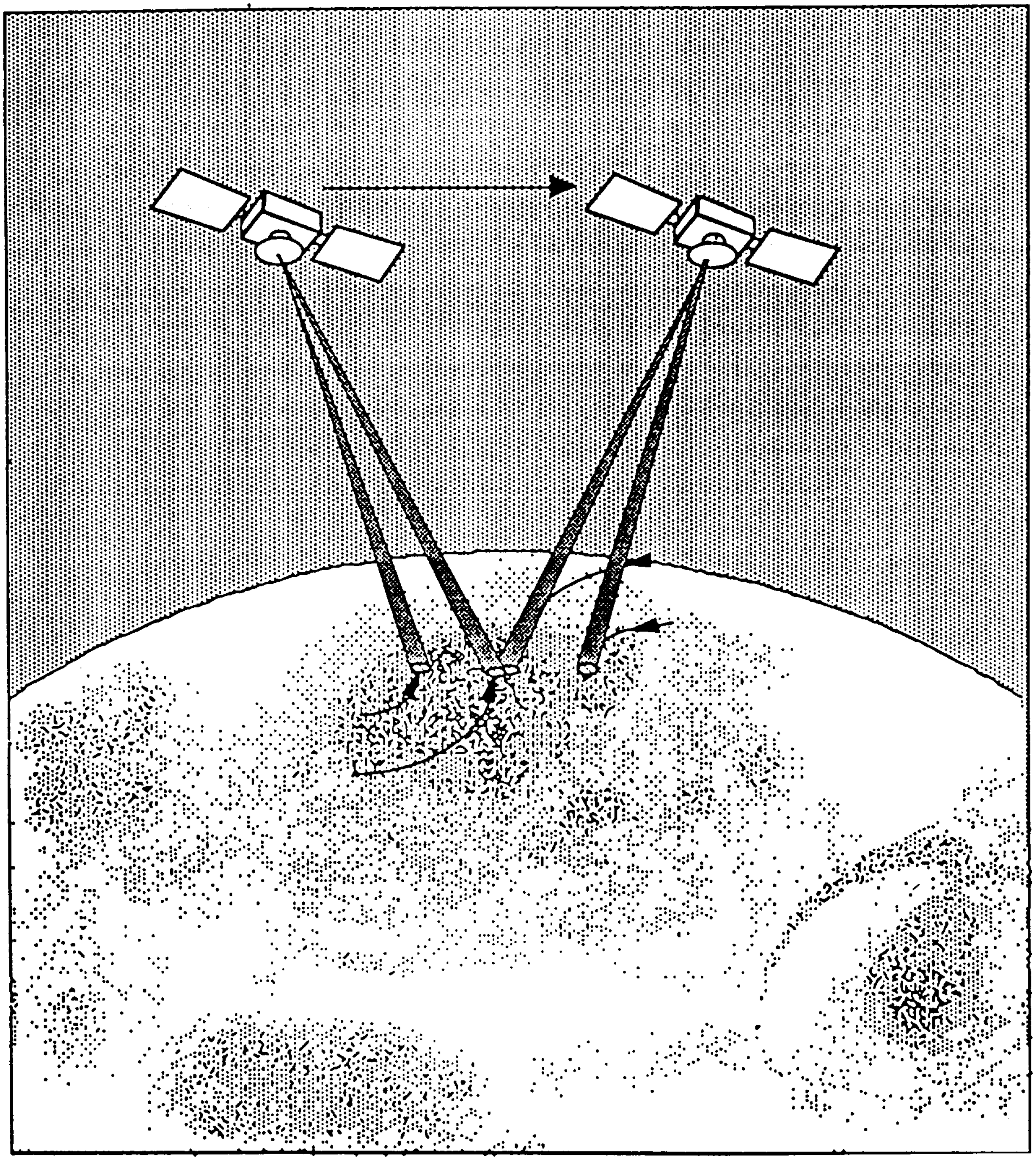

Figure 1.1 RAWS Conical Scan Pattern [Xin, 1990].

Chapter 2 gives a review on the theory of radar scattering from particles as well as details on the drop-size distributions studied. The specific parameters used in the SNR calculations are presented and the differences to the original candidate system of Table 1.3 discussed. The SNR data is analyzed for six frequencies and the optimum frequency(s) determined.

In Chapter 3 a review of the weather echo's statistical properties is given along with the development of the covariance estimator. The transmit waveform is defined based on the computation and validation of the unambiguous range and velocity.

Chapter 4 defines the two wind-error contributors, velocity uncertainty and antenna pointing-angle errors, used to determine the optimal antenna scan pattern. The maximum wind-error is calculated for three antenna scan patterns and specific issues discussed for each one.

Chapter 5 presents modifications to the candidate system of Table 1.3. A number of parameters, and the associated definitions, are shown.

Chapter 6 presents conclusions and suggestions on further study.

CHAPTER 2

RAWS SENSITIVITY STUDY

2.1 BACKSCATTERING AND ATTENUATION FROM CLOUDS

This section presents the formulas used to model the backscatter, attenuation, and scattering cross-sections of clouds, for both Mie and Rayleigh scattering. These formulas are then introduced into the radar range equation for calculating the system signal-to-noise ratio (SNR). The effect of atmospheric gaseous attenuation is also discussed and included in the SNR equation.

2.1.1 RADAR CROSS-SECTION

The radar cross-sections are based on an electromagnetic wave of power density S_i (Wm^{-2}) incident upon a suspended material particle of geometrical cross-sectional area A. A fraction of the incident power is absorbed by the particle, and an additional fraction is scattered by the particle in all directions. Three parameters model the behavior of the electromagnetic waves in the presence of such particles: the absorption, the scattering and the backscattering (i.e., the scattering in the direction of the radiation source) of the electromagnetic energy [Ulaby, 1981]. The ratio of absorbed power P_a to incident power density S_i is defined as the absorption cross-section, Q_a:

$$Q_a = \frac{P_a}{S_i} . \qquad \mathrm{m}^2 \qquad (2.1)$$

The ratio of Q_a to the physical cross-section A is known as the absorption efficiency factor, ξ_a. For a spherical particle of radius r, $A=\pi r^2$ resulting in

$$\xi_a = \frac{Q_a}{\pi r^2} . \qquad (2.2)$$

Consider an incident plane wave traveling in the z-direction, $S_S(\theta,\phi)$ is the power density of the radiation scattered in the direction (θ,ϕ) at a distance R from the particle. The total power scattered by the particle is the integral of $S_S(\theta,\phi)$ over the spherical surface of radius R centered on the particle; mathematically,

$$P_S = \int S_S(\theta,\phi)R^2\,d\Omega\,. \qquad \mathrm{W} \qquad (2.3)$$

Similar to the absorption cross-section, the scattering cross-section, Q_S, and scattering efficiency factor ξ_S are defined as

$$Q_S = \frac{P_S}{S_i}\,, \qquad \mathrm{m}^2 \qquad (2.4)$$

$$\xi_S = \frac{Q_S}{\pi r^2}\,. \qquad (2.5)$$

The extinction (or attenuation) cross-section, Q_e, is defined as the total power removed from the incident electromagnetic wave and is the sum of the absorption and scattering cross-sections:

$$Q_e = Q_a + Q_S\,. \qquad \mathrm{m}^2 \qquad (2.6)$$

Likewise for the extinction efficiency factor,

$$\xi_e = \xi_a + \xi_S\,. \qquad (2.7)$$

The radar backscattering cross-section, σ_b, is defined as the power density scattered in the backwards direction towards the radiation source, $S_S(\theta=\pi,\phi)$, such that σ_b

multiplied by the incident power density S_i would be equal to the total power radiated by an equivalent isotropic radiator. At a distance R from the scatterer, $S_s(\pi,\phi)$ is given by

$$S_s(\pi,\phi) = \frac{S_i \, \sigma_b}{4\pi R^2}, \qquad \text{Wm}^{-2} \qquad (2.8)$$

or by solving for the radar backscattering cross-section [Ulaby, 1981],

$$\sigma_b = 4\pi R^2 \frac{S_s(\pi,\phi)}{S_i}, \qquad \text{m}^2 \qquad (2.9)$$

2.1.2 MIE SCATTERING

The calculation of the absorption, scattering, and backscattering cross-sections for an arbitrary shape is very difficult. However, the solution for a dielectric sphere of radius r was derived by Mie [Mie, 1908]. The results are given in the form of converging series:

$$\xi_s(n,\chi) = \frac{2}{\chi^2} \sum_{l}^{\infty} (2l + 1)(|a_l|^2 + |b_l|^2), \qquad (2.10)$$

$$\xi_e(n,\chi) = \frac{2}{\chi^2} \sum_{l}^{\infty} (2l + 1)\mathrm{Re}\{a_l + b_l\}, \qquad (2.11)$$

and

$$\xi_b(n,\chi) = \frac{\sigma_b}{\pi r^2} = \frac{1}{\chi^2} \left| \sum_{l}^{\infty} (-1)^l (2l + 1)(a_l - b_l) \right|^2, \qquad (2.12)$$

with χ defined as

$$\chi = k_b r = \frac{2\pi r}{\lambda_b} = \frac{2\pi r}{\lambda_o} \sqrt{\varepsilon'_{rb}}, \qquad (2.13)$$

and n as

$$n = \frac{n_p}{n_b} = \sqrt{\frac{\varepsilon_{cp}}{\varepsilon_{cb}}} \equiv \sqrt{\varepsilon_c} \tag{2.14}$$

where: a_l and b_l are known as the Mie coefficients,

k_b = the wave number in the background medium,

ε'_{rb} = the real part of the relative dielectric constant of the background medium,

λ_b = the wavelength in the background medium,

λ_o = the free-space wavelength,

n = complex index of refraction of the particle relative to the background medium,

n_p = complex index of refraction of the particle material,

n_b = complex index of refraction of the background medium,

ε_{cp} = complex dielectric constant of the particle material,

ε_{cb} = complex dielectric constant of the background medium,

ε_c = complex dielectric constant of the particle relative to the background medium.

When the background medium is air, as is true in the atmosphere, then $\varepsilon'_{rb} = 1$, $n_b = 1$, and $\lambda_b = \lambda_o$. The equations for the Mie coefficients are not repeated here but can be obtained from several references [Mie, 1908; Ulaby, 1981].

2.1.3 RAYLEIGH-APPROXIMATION SCATTERING

When the particle size being measured is much smaller than the wavelength of the incident wave such that $|n\chi| \ll 0.5$ is satisfied, the Mie expression for ξ_s and ξ_e may be expressed by only the first two terms of the Mie series (2.10) and (2.11) and take the form

$$\xi_s = \frac{8}{3}\chi^4 |K|^2, \tag{2.15}$$

and

$$\xi_e = 4\,\chi\,\mathrm{Im}(-K) + \frac{8}{3}\chi^4 |K|^2, \tag{2.16}$$

where $$K = \frac{n^2 - 1}{n^2 + 2} = \frac{\varepsilon_c - 1}{\varepsilon_c + 2}. \qquad (2.17)$$

The absorption efficiency factor can then be obtained by subtracting (2.16) from (2.15) resulting in:

$$\xi_a = \xi_e - \xi_s = 4\,\chi\, \mathrm{Im}(-K)\,. \qquad (2.18)$$

The corresponding scattering and absorption cross-sections for a single spherical scatterer can now be determined using (2.2) and (2.5):

$$Q_a = \frac{\lambda^2}{\pi}\chi^3\,\mathrm{Im}(-K), \qquad \mathrm{m}^2 \qquad (2.19)$$

and $$Q_s = \frac{2\lambda^2}{3\pi}\chi^6|K|^2 \qquad \mathrm{m}^2 \qquad (2.20)$$

For small values of χ, and finite values of n, it can be shown [Kerr, 1951] that (2.12) reduces to

$$\xi_b = 4\,\chi^4\,|K|^2, \qquad (2.21)$$

and $$\sigma_b = \pi r^2 \xi_b = \frac{64\pi^5}{\lambda^4} r^6\,|K|^2, \qquad \mathrm{m}^2 \qquad (2.22)$$

in the Rayleigh region defined by $|n\chi| < 0.5$ [Ulaby, 1981].

Equations (2.19), (2.20) and (2.22) indicate that to determine the cross-sections for a spherical particle of radius r at a given wavelength λ, only the values for $|K|^2$ and $\mathrm{Im}(-K)$ are required. For water, the value of $|K|^2$ is approximately equal to 0.9 for frequencies between 3 GHz to 30 GHz and temperatures from 0°C to 20°C, while $\mathrm{Im}(-K)$ increases with frequency [Ulaby, 1981]. Particular values of $|K|^2$ and $\mathrm{Im}(-K)$ are tabulated in a number of sources [Battan, 1973; Meneghini, 1990] and are also attainable from the Debye equation [Ulaby, 1986] used in conjunction with (2.17). For ice particles, the real value of n_i (the complex index of refraction for ice) is approximately frequency- and temperature-independent and is given by

$$\mathrm{Re}(n_i) = 1.78. \tag{2.23}$$

The imaginary part of n_i varies with frequency and temperature but its value is much smaller than $\mathrm{Re}(n_i)$. This implies $|n_i| \approx \mathrm{Re}(n_i)$. Tables 2.1 and 2.2 present values of $|K|^2$ and Im(-K) for both water and ice, respectively.

Table 2.1 $|K|^2$ and Im(-K) values for water clouds [Battan, 1973].

Quantity	Temperature (°C)	Wavelength (Cm)			
		10	3.21	1.24	0.62
n	20	8.88	8.14	6.15	4.44
	10	9.02	7.80	5.45	3.94
	0	8.99	7.14	4.75	3.45
	− 8	. . . .	6.48	4.15	3.10
κ	20	0.63	2.00	2.86	2.59
	10	0.90	2.44	2.90	2.37
	0	1.47	2.89	2.77	2.04
	− 8	. . . .	. . . .	2.55	1.77
$\|K\|^2$	20	0.928	0.9275	0.9193	0.8926
	10	0.9313	0.9282	0.9152	0.8726
	0	0.9340	0.9300	0.9055	0.8312
	− 8	. . . .	. . . .	0.8902	0.7921
Im($-K$) . . .	20	0.00474	0.01883	0.0471	0.0915
	10	0.00688	0.0247	0.0615	0.1142
	0	0.01102	0.0335	0.0807	0.1441
	− 8	. . . .	. . . .	0.1036	0.1713

SOURCE: Gunn and East 1954.

Table 2.2 $|K|^2$ and Im(-K) values for ice clouds [Battan, 1973].

Quantity	Temperature (°C)	Value
n	All temperatures when $\rho = 0.92$ gm/cm^3	1.78
κ	0	2.4×10^{-3}
	−10	7.9×10^{-4}
	−20	5.5×10^{-4}
$\|K\|^2$	All temperatures when $\rho = 1$	0.197
Im($-K$)	0	9.6×10^{-4}
	−10	3.2×10^{-4}
	−20	2.2×10^{-4}

SOURCE: Gunn and East 1954.

As indicated earlier, the Rayleigh approximation only applies when the particle diameters are small compared to the incident wavelength. For computational purposes, this implies $|n\chi| < 0.5$. The Mie and Rayleigh approximation for the extinction and scatter efficiency factors, ξ_e and ξ_s, of water clouds are shown in Figures 2.1a, b, and c.

Ice clouds may contain particles with radii up to about 10 mm, but due to the smaller refractive index (see Tables 2.1 and 2.2), the Rayleigh criterion is applicable up to about 70 GHz for ξ_e, and up to 200 GHz for ξ_b [Ulaby, 1981].

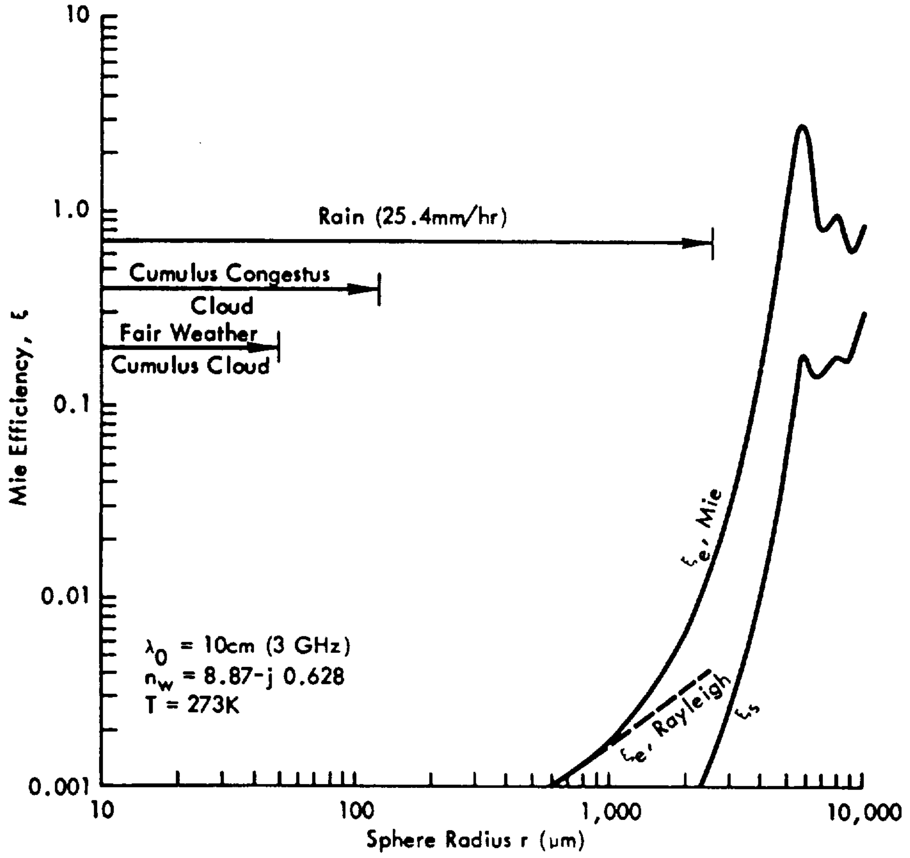

(a)

Figure 2.1 Mie efficiency factors for scattering and extinction by a water sphere as a function of drop radius at: (a) 3 GHz, (b) 30 GHz, and (c) 300 GHz. Horizontal arrows indicate range of drop radii [Fraser, 1975].

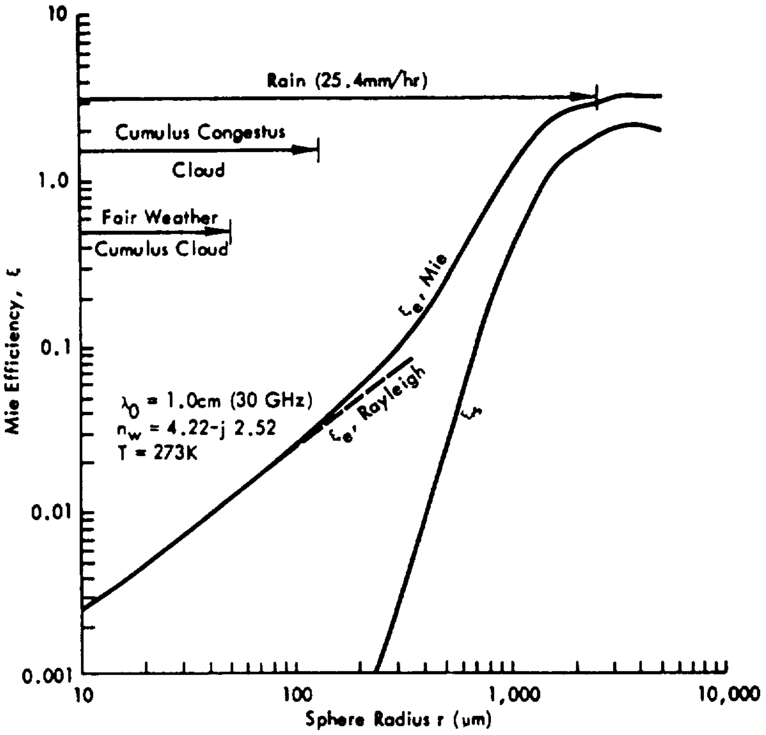

Rain (25.4mm/hr)
Cumulus Congestus
Cloud
Fair Weather
Cumulus Cloud
ζ_e, Mie
ζ_e, Rayleigh
ζ_s
λ_0 = 1.0cm (30 GHz)
n_w = 4.22-j 2.52
T = 273K
Mie Efficiency, ζ
10
1.0
0.1
0.01
0.001
10
100
1,000
10,000
Sphere Radius r (μm)

(b)

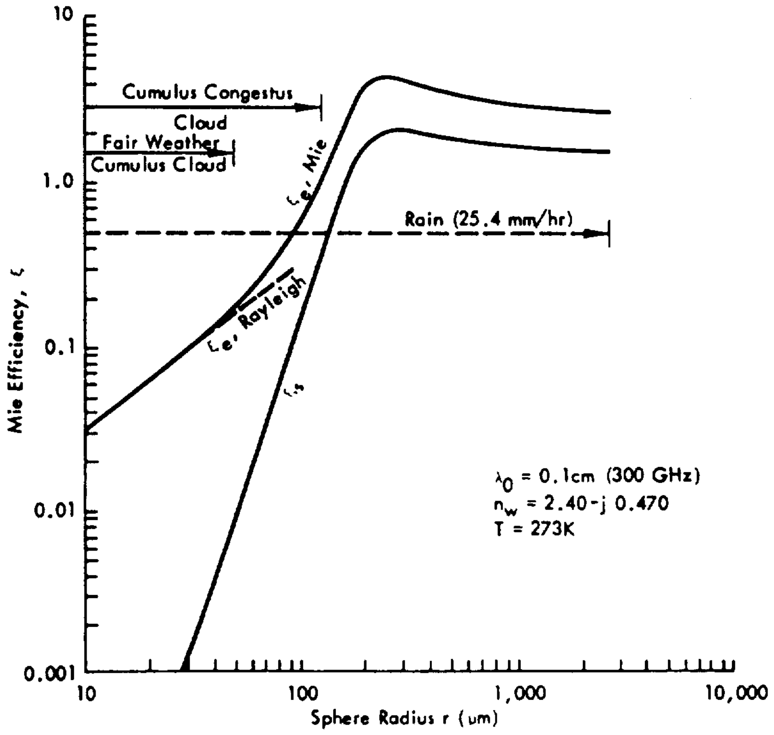

Cumulus Congestus
Cloud
Fair Weather
Cumulus Cloud
Rain (25.4 mm/hr)
ζ_e, Mie
ζ_e, Rayleigh
ζ_s
λ_0 = 0.1cm (300 GHz)
n_w = 2.40-j 0.470
T = 273K
Mie Efficiency, ζ
10
1.0
0.1
0.01
0.001
10
100
1,000
10,000
Sphere Radius r (μm)

(c)

2.1.4 VOLUME SCATTERING

In a cloud resolution volume, the scatterers (water or ice particles) are randomly distributed within the volume, so there are no coherent phase relationships between the fields scattered by the individual particles. This assumption allows the use of non-coherent scattering theory when computing the average absorption and backscattering within the volume. Additionally, the concentration of particles is usually small enough to support the assumption that shadowing effects can be ignored.

The volume scattering coefficient, κ_S, is the total scattering cross-section per unit volume, and its units are $(\mathrm{Npm}^{-3}) \times \mathrm{m}^2 = \mathrm{Npm}^{-1}$. The volume scattering coefficient is defined by

$$\kappa_S = \int_{r_{\min}}^{r_{\max}} p(r) Q_S dr \qquad \mathrm{Npm}^{-1} \qquad (2.24)$$

where $p(r)$ represents the drop-size distribution (number of drops per m^3 per unit increment of r), Q_S is the scattering cross-section of a sphere with radius r, and $r_{\max}$ and $r_{\min}$ are the upper and lower limits of the drop radii contained in the cloud. If the Rayleigh criterion is satisfied, (2.20) can be substituted into (2.24) resulting in

$$\kappa_S = \frac{2\pi^5}{\lambda^4} |K|^2 \sum_{i=1}^{N} D_i^6 \qquad \mathrm{Npm}^{-1} \qquad (2.25)$$

where N is the total number of droplets per unit volume of the cloud and D_i is the diameter of the i^{th} droplet per unit volume.

Similarly the volume absorption coefficient can be determined by

$$\kappa_a = \int_{r_{\min}}^{r_{\max}} p(r) Q_a dr \qquad \mathrm{Npm}^{-1} \qquad (2.26)$$

and using (2.19) yields

$$\kappa_a = \frac{\pi^2}{\lambda} \mathrm{Im}(-K) \sum_{i=1}^{N} D_i^3 . \quad \mathrm{Npm}^{-1} \tag{2.27}$$

By use of the following equation for water content per cubic meter

$$m_v = 10^6 \times \frac{\pi}{6} \sum_{i=1}^{N} D_i^3 , \qquad \mathrm{gm}^{-3} \tag{2.28}$$

the volume absorption coefficient becomes

$$\kappa_a = \frac{6\pi}{\lambda} \mathrm{Im}(-K)\, m_v\, 10^{-6} . \quad \mathrm{Npm}^{-1} \tag{2.29}$$

The volume extinction coefficient can be obtained in the same manner, i.e.,

$$\kappa_e = \int_{r_{\min}}^{r_{\max}} p(r)(Q_s + Q_a)dr \qquad \mathrm{Npm}^{-1}$$

$$\kappa_e = \kappa_a + \kappa_s . \qquad \mathrm{Npm}^{-1} \tag{2.30}$$

Note that for smaller droplet radii the value of the absorption cross-section Q_a dominates in determining the extinction cross-section Q_e (see Figure 2.1). This is due to the D^6 scattering-coefficient dependence as compared with the D^3 absorption-coefficient dependence in the Rayleigh region. Since the cloud volume-extinction coefficient κ_e is the sum of κ_s and κ_a, it is approximately equal to the volume absorption coefficient κ_a for the smaller droplet radii.

As with the scattering and absorption volume coefficients, a similar definition is used for the volume backscatter coefficient, σ_V, that of a summation (or integral) of backscattering cross-sections of the individual drops in a unit volume:

$$\sigma_V = \int_{r_{\min}}^{r_{\max}} p(r)\sigma_b dr. \qquad \text{m}^{-1} \qquad (2.31)$$

Substituting (2.22) into (2.31) yields

$$\sigma_V = \frac{\pi^5}{\lambda^4} |K|^2 \sum_{i=1}^{N} D_i^6, \qquad \text{m}^{-1} \qquad (2.32\text{a})$$

$$\sigma_V = \frac{\pi^5}{\lambda^4} |K|^2 Z\, 10^{-18}, \qquad \text{m}^{-1} \qquad (2.32\text{b})$$

where Z is the reflectivity factor and is the summation of all the droplet diameters per unit volume. The 10^{-18} factor allows for Z to be expressed in units of $\text{mm}^6\ \text{m}^{-3}$, commonly used in the meteorology community.

2.1.5 ATTENUATION BY ATMOSPHERIC GASES

Electromagnetic waves suffer attenuation due to absorption by atmospheric gases in addition to the attenuation caused by the water droplets. The two primary gases of concern are oxygen and water vapor. In the frequency range from 10 to 100 GHz the only significant contributors to gaseous attenuation are a water-vapor absorption band centered at 22.235 GHz and an oxygen band that extends from 53.5 to 65.2 GHz. These absorption bands result in "windows" where low attenuation to radio waves occurs. Figure 2.2 illustrates the one-way attenuation due to atmospheric gases at zenith. For an arbitrary elevation angle, the zenith attenuation value must be multiplied by the cosecant of the elevation angle α, giving

$$L_a(\alpha) = 2\, A_z \csc(\alpha) \qquad \text{dB} \qquad (2.33)$$

where $L_a(\alpha)$ is the total two-way atmospheric gaseous attenuation, A_z is the zenith one-way atmospheric gaseous attenuation as shown in Figure 2.2, and α is the elevation angle [Ippolito, 1989].

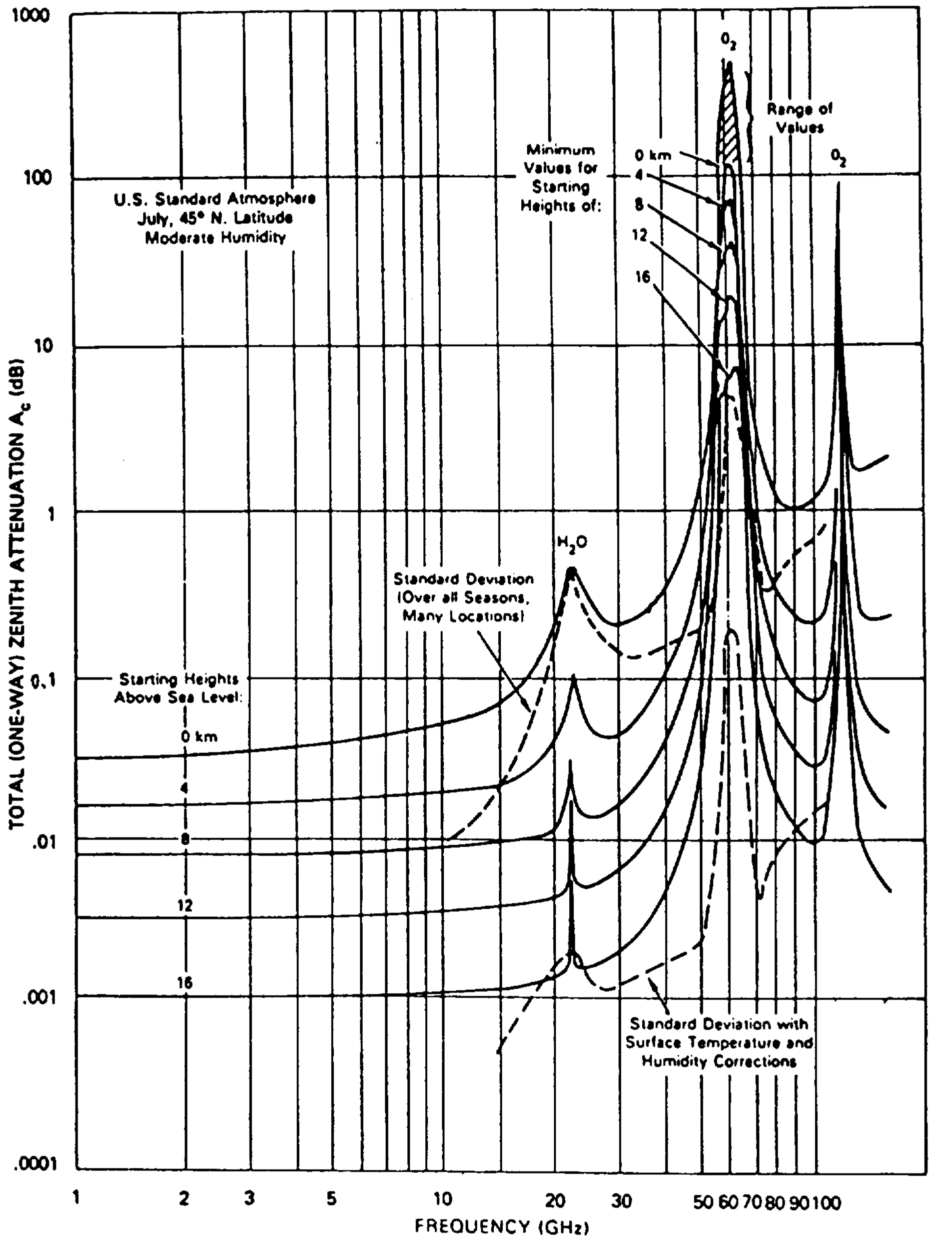

Figure 2.2 Total zenith attenuation versus frequency [Ippolito, 1989].

2.1.6 RADAR RANGE EQUATION

The radar range equation has many forms depending on the application and the desired variables with which to work. The basic radar range equation is given by

$$P_r = \frac{P_t G^2 \lambda^2 \sigma}{(4\pi)^3 R^4 L_t L_r L_a(\alpha)} e^{-2\gamma} \qquad \text{W} \qquad (2.34)$$

where P_r = peak received power, W,
P_t = peak transmitted power, W,
G = antenna gain along the beam axis,
λ = wavelength, m,
R = range to scattering volume, m,
L_t = transmitter losses,
L_r = receiver losses,
γ = one-way path attenuation, Np,
L_a = two-way atmospheric gas attenuation , dB,
α = antenna elevation angle, deg,
σ = radar cross-section of scattering volume.

The attenuation, γ, is the sum of the attenuation coefficient due to clouds and precipitation, integrated along the path R [Ulaby, 1981]:

$$\gamma = \int_0^R (\kappa_{ec} + \kappa_{ep}) dr \qquad \text{Np} \qquad (2.35)$$

where κ_{ec}, and κ_{ep} are the cloud and precipitation extinction coefficients, respectively.

The radar cross-section, σ, is equal to the volume backscatter coefficient σ_v integrated over the volume contributing to the received power. For a narrow-beam antenna with 3 dB-power beamwidths of β_θ and β_ϕ, this volume at a range R is

$$V=\pi\left(\frac{R\beta_\theta}{2}\right)\left(\frac{R\beta_\phi}{2}\right)\left(\frac{c\tau_p}{2}\right) \qquad \mathrm{m}^3 \qquad (2.36)$$

where c is the speed of light and τ_p is the pulse length. Assuming a Gaussian-shaped antenna pattern, V must be reduced by a factor of 2 ln(2) to describe the equivalent volume that accounts for the echo power received by a the two-way antenna pattern from distributed clutter [Skolnik, 1980]. With the radar cross-section defined as

$$\sigma=\sigma_v V \qquad \mathrm{m}^2 \qquad (2.37)$$

the final form of the range equation becomes

$$P_r=\frac{P_t G^2 \lambda^2 \beta_\theta\, \beta_\phi c\tau_p}{1024 \ln(2) \pi^2 R^2 L_t L_r L_a(\alpha)}\ \sigma_v\, \mathrm{e}^{-2\gamma}. \ \ \mathrm{W} \qquad (2.38)$$

The signal-to-noise ratio (SNR) can then be determined by first calculating the receiver noise power, P_n, and dividing this value into (2.38). This results in

$$\mathrm{SNR}=\frac{P_t G^2 \lambda^2 \beta_\theta\, \beta_\phi c\tau_p}{1024 \ln(2) \pi^2 R^2 L_t L_r L_a(\alpha) P_n}\ \sigma_v\, \mathrm{e}^{-2\gamma}. \qquad (2.39)$$

where $P_n = kT_0BN_F$ (2.40)

k = Boltzmann's constant, 1.38×10^{-23},

T_o = ambient temperature, 290 K,

B = receiver bandwidth, Hz,

N_F = receiver noise figure.

2.2 SIGNAL-TO-NOISE RATIO STUDY

2.2.1 CLOUD MODELS

In the Rayleigh region, (2.29) indicates only the water content, m_V, of the cloud is necessary in calculating the attenuation. However, in generating values for the backscatter coefficient, σ_V, knowledge of either the drop-size distribution or the reflectivity factor (in the Rayleigh region), is required. All parameters involved in the SNR calculation are relatively easy to measure or model with the exceptions of $p(r)$ and Z. Many physicists have devoted considerable effort in accurately modeling these parameters. Figure 2.3 illustrates examples of measured drop-size distribution for several cloud types [Mason, 1957].

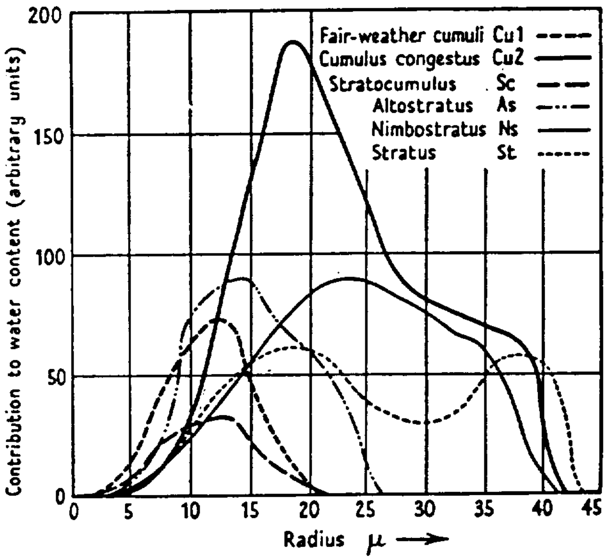

Figure 2.3 The mean droplet-size distribution of various cloud types [Mason, 1957].

For most water clouds, the distribution has a sharp rise in concentration for low values of droplet radii followed by a gradual decrease for the larger drop sizes. This general shape is evident in the distributions shown in Figure 2.3.

Xin reviewed several distribution models, including the log normal, modified gamma distribution and the Khrigian-Mazin distributions [Xin, 1990]. Propp studied a generalized case of the Khrigian-Mazin distribution developed by Deirmendjian [Deirmendjian, 1964]. The Deirmendjian model used here is given by

$$n(r) = \mathrm{A}\, r^{\mathrm{C}_1} \exp(-\mathrm{B} r^{\mathrm{C}_2}) \qquad \mu\mathrm{m}^{-4} \qquad (2.41)$$

where

$$\mathrm{A} = \frac{m_v \mathrm{C}_2 \mathrm{B}^{\left(\frac{\mathrm{C}_1+4}{\mathrm{C}_2}\right)}}{\frac{4}{3}\pi \times 10^6 \Gamma\left(\frac{\mathrm{C}_1+4}{\mathrm{C}_2}\right)},$$

$$\mathrm{B} = \frac{\mathrm{C}_1}{\mathrm{C}_2 r_c^{\mathrm{C}_2}},$$

Γ = gamma function,

m_v = mass density of the cloud, g m^{-3},

r_c = mode radius, μm,

C_1 and C_2 = shape parameters.

This distribution is based on a modified gamma function which reduces to the gamma function when $\mathrm{C}_2 = 1$. Values for r_c, C_1 and C_2 where given by Deirmendjian for 10 cloud types [Deirmendjian, 1969] and later expanded to include 19 various cloud types by Reifenstein and Gaut [Reifenstein, 1971]. Only 17 of the 19 cloud types are analyzed. The "Fog Layer, Ground to 150 ft." (20-3) and "Hazy, Heavy" (20-4) clouds have been excluded due to their limited altitude and extremely small water content, respectively. Table 2.3 summarizes these parameters [Chahine, 1983]. Note that a water cloud implies a non-precipitating cloud.

Table 2.3 Properties of standard cloud models.

Cloud Model	Cloud Name	Cloud Base	Cloud Top	*mv*	*rc*	C1	C2	Prin. Comp.
1-A-1	Cirrostratus	4000	6000	0.1	40	6	0.5	I
1-M-1	Cirrostratus	5000	7000	0.1	40	6	0.5	I
1-T-1	Cirrostratus	6000	8000	0.1	40	6	0.5	I
10-1	Altocumulus	2400	2900	0.15	10	6	0.5	W
14-1	Altocumulus	2400	2900	0.15	10	6	1	W
20-1	Low-Lying Stratus	150	650	0.25	10	6	1	W
20-2	Low-Lying Stratus	500	1000	0.25	10	6	1	W
21-1C	Drizzle, 0.2 mm/hr	1000	1500	1	10	6	0.5	W
21-1B		500	1000	2	10	6	0.5	W
21-1A		0	500	1	20	6	0.5	R
21-2D	Steady Rain, 3 mm/hr	1000	1500	1	10	6	0.5	W
21-2C		500	1000	2	10	6	0.5	W
21-2B		150	500	1	10	6	0.5	W
21-2A		0	150	0.2	200	5	0.5	R
21-3D	Steady Rain, 15 mm/hr	2000	4000	2	10	6	0.5	W
21-3C		1000	2000	3	10	6	0.5	W
21-3B		300	1000	2	10	6	0.5	W
21-3A		0	300	1	200	5	0.5	R
22-1	Stratocumulus	330	660	0.25	10	6	0.5	W
22-2	Stratocumulus	660	1320	0.25	10	6	0.5	W
25-1C	Fair Weather Cumulus	1500	2000	0.5	10	6	0.5	W
25-1B		1000	1500	1	10	6	0.5	W
25-1A		500	1000	0.5	10	6	0.5	W
25-2C	Cumulus, 2.4 mm/hr	1000	3000	2	20	6	0.2	W
25-2B		500	1000	1	20	6	0.2	W
25-2A		0	500	0.1	400	5	0.5	R
25-3C	Cumulus, 12 mm/hr	1000	4000	4	10	6	0.2	W
25-3B		400	1000	2	20	6	0.2	W
25-3A		0	400	0.5	400	5	0.5	R
25-4E	Cumulus Congestus	2500	3000	0.5	20	5	0.3	W
25-4D		2000	2500	1	20	5	0.3	W
25-4C		1600	2000	0.8	20	5	0.3	W
25-4B		1200	1600	0.5	15	5	0.4	W
25-4A		1000	1200	0.3	10	6	0.5	W
26-1F	Cumulonimbus, 150 mm/hr	8000	10000	0.2	40	6	0.5	I
26-1E		6000	8000	3	10	6	0.2	W
26-1D		4000	6000	4	10	6	0.2	W
26-1C		1000	4000	8	10	6	0.2	W
26-1B		300	1000	7	20	6	0.2	W
26-1A		0	300	6.3	400	5	0.2	R

The Deirmendjian model supports several cloud types each having one or more horizontal layer(s) for which the composition (water, ice, or rain), mass density, mode radius, two shape parameters, and altitude limits are specified. The maximum concentration will occur at the mode radius, and the two shape parameters will control the shapes of the distribution's rising and falling edges. The ability to model many different cloud types at various altitudes is a major advantage of the Deirmendjian model. The comparison of a sample Deirmendjian distribution given in Figure 2.4 with the data shown in Figure 2.3 reveals a good correlation between the shapes of the Deirmendjian model and measured results.

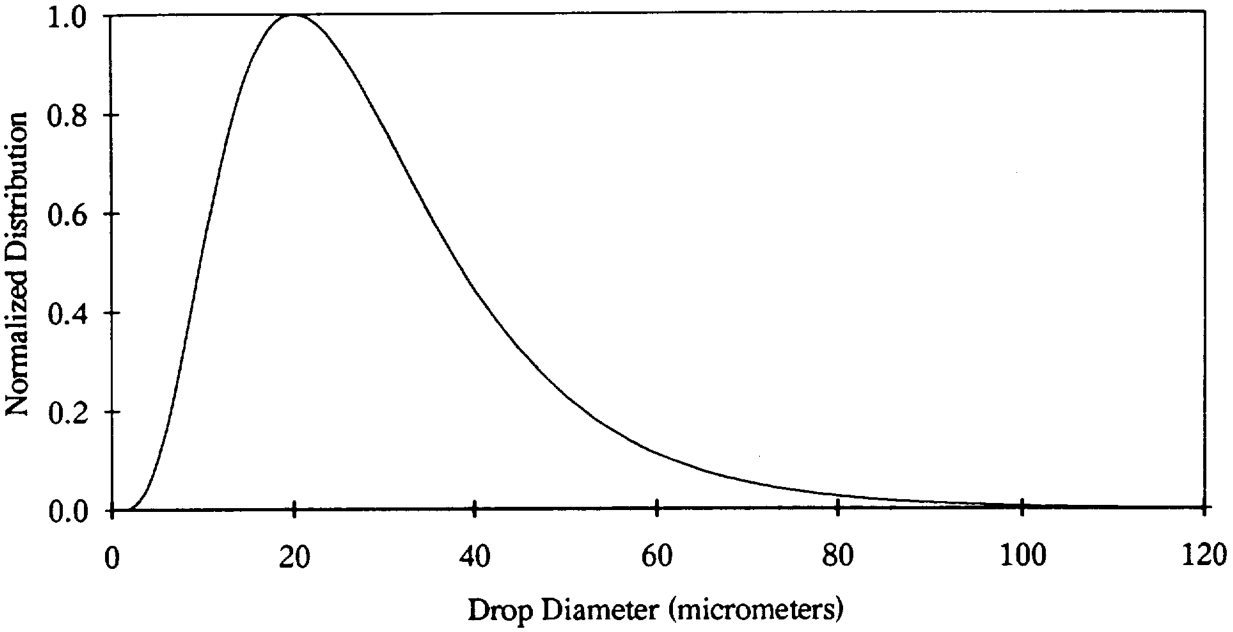

Figure 2.4 Normalized Deirmendjian distribution of top layer for the steady rain @ 3 mm/hr model (21-2).

The drop-size distribution enters into the SNR equation (2.39) in the calculation of the radar volume backscatter coefficient σ_V (2.32), and (if the Rayleigh approximation is satisfied) in the calculation of the reflectivity factor Z using:

$$Z = \int_0^{D_{\max}} n(D) D^6 dD. \qquad (2.42)$$

where $D_{\max}$ is the largest drop diameter of the distribution $n(D)$ to contribute significantly to the reflectivity factor. Since Z is a function of D^6, the larger droplets greatly influence the value of Z. The reflectivity factor is commonly used by meteorologists as a measure of return signal strength of the weather echo. Due to the wide dynamic range of weather returns, radar meteorologists use a logarithmic scale $\mathrm{dB}Z = 10\log_{10} Z$, where Z is in units of $\mathrm{mm}^6\ \mathrm{m}^{-3}$. Precipitation produces dBZ values ranging from near 0 dBZ to larger that 60 dBZ in regions of heavy rainfall and hail [Doviak, 1984]. Many formulas have been developed to compute the reflectivity factor with minimal knowledge of the drop-size distribution. One such equation, developed by Atlas, is given by the expression

$$Z = G\left(\frac{6}{\pi}\right) D_o^3 \left(\frac{m_V}{\rho}\right) \times 10^{-6} \quad \mathrm{mm}^6\ \mathrm{m}^{-3} \qquad (2.43)$$

where D_o is the median volume diameter (a diameter such that half the liquid-water content is contained in the drops with smaller diameters) in meters, m_V is the liquid water content in gm^{-3}, ρ is the density of the scattering material in gm^{-3} ($10^6\ \mathrm{gm}^{-3}$ for water), and G is a constant that was shown to equal 1.35 [Atlas, 1953]. This equation is based on the original work of Trabert [Trabert, 1901], and the further study of aufm Kampe and Weickmann [Weickmann, 1952], to define a relationship between visibility, water content, and droplet size. The value of G was computed from data generated by Boucher [Boucher, 1952] based on measurements by Diem [Diem, 1948]. A second model developed by Atlas and Bartoff is given by the simple equation

$$Z = 0.048\, m_V^2. \qquad \mathrm{mm}^6\ \mathrm{m}^{-3} \qquad (2.44)$$

This equation is the result of a regression algorithm applied to Boucher's data [Atlas, 1954]. Note that both reflectivity factor equations only require minimal information about the drop distribution, i.e., D_0 and m_v.

2.2.2 VERIFICATION OF CLOUD MODEL

This section discusses the steps taken to verify the reflectivity factors calculated from the Deirmendjian model with either measured data sets or proven models. Each of the three cloud principal components (water, rain, and ice) is presented separately.

2.2.2.1 WATER LAYERS

Very few measurements are available to verify the drop-size distribution and reflectivity-factor models. Gossard published four data sets that either calculate the reflectivity factor using the drop-size distribution, or by the use of (2.43) [Gossard, 1983]. These data are taken from the works of Weickmann-aufm Kampe [Weickmann, 1953], Squires [Squires, 1958], Diem [Diem, 1948], and Breed [Breed, 1976], and are shown in Tables 2.4, 2.5, and 2.6.

Table 2.4 Cloud parameters by Weickmann-aufm Kampe and Squires.

	Cloud type	Number density (N) (m^{-3})	Water content (M) M($g\ m^{-3}$)	Reflectivity Z ($mm^6\ m^{-3}$)	Median diameter (D_o) (m)	6th power mean diameter (m)	Atlas Barthoff (Z) Z ($mm^6\ m^{-3}$)	$N_T D_o^*$ ($mm^6\ m^{-3}$)
Weickmann-aufm Kampe	Fair weather cumulus	302×10^6	1.0		32×10^{-6}		0.0845	
	Cumulus congestus	64×10^6	3.9		108×10^{-6}		12.7	
	Cumulonimbus	72×10^6	2.5		108×10^{-6}		8.1	
		$\sum_i N_i$ (m^{-3})	$\rho \frac{\pi}{6} \sum_i N_i D_i^3$ ($g\ m^{-3}$)	$\sum_i N_i D_i^6$ ($mm^6\ m^{-3}$)				
Squires	Continental cumulus	495×10^6	0.35	1.82×10^{-3}	13.2×10^{-6}	12.4×10^{-6}	2.1×10^{-3}	2.6×10^{-3}
	Trade wind cumulus	72.5×10^6	0.81	5.3×10^{-2}	26.5×10^{-6}	30.0×10^{-6}	3.9×10^{-2}	2.5×10^{-2}
	Hawaiian dark stratus	23.3×10^6	0.335	4.0×10^{-2}	34.0×10^{-6}	34.7×10^{-6}	3.4×10^{-2}	3.6×10^{-2}
	Hawaiian orographic	5.2×10^6	0.523	1.35	92.0×10^{-6}	80.0×10^{-6}	1.05	3.15

Table 2.5 Cloud parameters by Diem.

	$M = \frac{\pi}{6}\sum_i N_i D_i^3$,	$Z = \sum_i N_i D_i^6$	
Diem's cloud types	M (g m^{-3})	Z (mm^6 m^{-3})	D_o (m)
CU_1	0.32	1.18×10^{-3}	11.2×10^{-6}
CU_2	0.87	2.76×10^{-2}	20.6×10^{-6}
SC	0.09	3.53×10^{-4}	10.1×10^{-6}
AS	0.28	2.40×10^{-3}	12.8×10^{-6}
NS	0.40	1.40×10^{-2}	23.4×10^{-6}
ST	0.29	1.29×10^{-2}	24.1×10^{-6}

Table 2.6 Cloud parameters by Breed.

N_T (m^{-3})	$\bar{D}$ (μm)	M (g m^{-3})	D_o (μm)	Z (mm^6 m^{-3})
687	8.4	.216	30.8	.0163
72	7.4	.015	27.2	7.8×10^{-4}
487	9.7	.234	35.6	2.7×10^{-2}
565	9.3	.236	34.1	2.4×10^{-2}
461	9.9	.233	36.3	2.9×10^{-2}
559	9.7	.405	35.5	4.7×10^{-2}
104	7.1	.028	26.1	1.3×10^{-3}
64	8.3	.027	30.5	2.0×10^{-3}
209	8.1	.085	29.7	5.8×10^{-3}
352	9.5	.234	34.9	2.6×10^{-2}

Since the data do not support the shape parameters needed by the Deirmendjian model, no direct comparison can be made between the Deirmendjian distribution and the data sets. However, since (2.43) and (2.44) only depend on D_o and m_v, it is possible to compare these models to the data for validation and, if one accurately represents the data, use it to validate the Deirmendjian model. For these comparisons, the data given by Weickmann-aufm Kampe and Breed must be discarded since the reflectivity factor for these data were computed using (2.43). It should also be noted that the Diem data set is questionable since both (2.43) and (2.44) were derived using Diem's measurements. Tables 2.7 and 2.8 present the comparison of the Diem and Squires data with the reflectivity factor models (2.43) and (2.44).

Table 2.7 Comparison of data sets with reflectivity factor model (2.43).

Cloud Type	Cloud Type Reflectivity Factor (dBZ)	Atlas Model (2.43) Reflectivity Factor (dBZ)	Delta (dB)
Diem:			
Stratocumulus	-34.5	-36.2	-1.7
Altostratus	-26.2	-28.2	-2.0
Stratus	-18.9	-19.8	-0.9
Fair Weather Cumulus	-29.3	-29.4	-0.1
Nimbostratus	-18.5	-18.8	-0.3
Cumulus Congestus	-15.6	-17.1	-1.5
Squires:			
Hawaiian Dark Stratus	-14.0	-14.7	-0.7
Continental Cumulus	-27.4	-26.8	0.6
Hawaiian Orographic	1.3	0.2	-1.1
Trade Wind Cumulus	-12.8	-14.1	-1.3

Table 2.8 Comparison of data sets with reflectivity factor model (2.44).

Cloud Type	Cloud Type Reflectivity Factor (dBZ)	Atlas Model (2.44) Reflectivity Factor (dBZ)	Delta (dB)
Diem:			
Stratocumulus	-34.5	-34.1	-0.4
Altostratus	-26.2	-24.2	-2.0
Stratus	-18.9	-23.9	-5.0
Fair Weather Cumulus	-29.3	-23.1	-6.2
Nimbostratus	-18.5	-21.1	2.6
Cumulus Congestus	-15.6	-14.4	-1.2
Squires:			
Hawaiian Dark Stratus	-14.0	-22.7	8.7
Continental Cumulus	-27.4	-22.3	-5.1
Hawaiian Orographic	1.3	-18.8	20.1
Trade Wind Cumulus	-12.8	-15.0	2.3

The fourth column, "Delta", indicates the difference in dB between the data sets and the models. As seen from Table 2.7, (2.43) underestimates the data sets by < 2 dB, while Table 2.8 shows (2.44) has as much as 20.1 dB of error. This implies equation (2.43) models the reflectivity factor accurately for clouds defined by the Diem and Squires data, characterized by D_O<92 μm and m_V<0.87 gm^{-3}, and thus will be used to verify the Deirmendjian model.

Next the reflectivity factors were calculated from (2.43) based on the Deirmendjian model and associated parameters as shown in Table 2.3. Since the data sets are only valid for non-precipitating clouds, only the Deirmendjian water-clouds were used. The values of D_O must first be computed for each of the Deirmendjian water-cloud layers for use in (2.43). This is accomplished by noting the water content can be expressed as

$$m_V = \frac{4\pi}{3} \times 10^6 \int_0^{r_{\max}} n(r) r^3 dr. \qquad \text{gm}^{-3} \qquad (2.45)$$

Making a change of variables with the relationship $D=2r$, the values of D_O were obtained by numerically solving for D_O in the equation

$$\frac{\pi}{12} \times 10^6 \int_0^{D_O} n(D) D^3 dD = 0.5. \qquad (2.46)$$

The values calculated for D_0 are given in Table 2.9.

Table 2.9 Summary of D_o, D_{max}, and reflectivity factor values for both the Deirmendjian model and (2.43).

Cloud Type	*mv* (g/m3)	Dmax (um)	*Do* (um)	Deirmendjian (dBZ)	Atlas (2.43) (dBZ)
10-1(w)	0.15	200	53.8	-10.1	-12.2
14-1(w)	0.15	200	32.4	-18.5	-18.8
20-1(w)	0.25	200	32.4	-16.3	-16.6
20-2(w)	0.25	200	32.4	-16.3	-16.6
21-1C(w)	1	200	53.8	-1.9	-4.0
21-1B(w)	2	200	53.8	1.2	-1.0
21-2D(w)	1	200	53.8	-1.9	-4.0
21-2C(w)	2	200	53.8	1.2	-1.0
21-2B(w)	1	200	53.8	-1.9	-4.0
21-3D(w)	2	200	53.8	1.2	-1.0
21-3C(w)	3	200	53.8	2.9	0.8
21-3B(w)	2	200	53.8	1.2	-1.0
22-1(w)	0.25	200	53.8	-7.9	-10.0
22-2(w)	0.25	200	53.8	-7.9	-10.0
25-1C(w)	0.5	200	53.8	-4.9	-7.0
25-1B(w)	1	200	53.8	-1.9	-4.0
25-1A(w)	0.5	200	53.8	-4.9	-7.0
25-2C(w)	2	6000	498	35.4	28.0
25-2B(w)	1	6000	498	32.4	25.0
25-3C(w)	4	6000	250	29.5	22.1
25-3B(w)	2	6000	498	35.5	28.0
25-4E(w)	0.5	2000	274	19.3	14.2
25-4D(w)	1	2000	274	22.3	17.2
25-4C(w)	0.8	2000	274	21.4	16.3
25-4B(w)	0.5	2000	126	7.5	4.1
25-4A(w)	0.3	200	53.8	-7.1	-9.2
26-1E(w)	3	6000	250	28.2	20.8
26-1D(w)	4	6000	250	29.5	22.1
26-1C(w)	8	6000	250	32.5	25.1
26-1B(w)	7	6000	498	40.9	33.5

With the values of D_o computed, the difference between the Deirmendjian model and (2.43) can be calculated. The results are illustrated in Figure 2.5, where the error is defined as the reflectivity factor produced by (2.43) subtracted from the Deirmendjian reflectivity factor (both reflectivity factors calculated in units of dBZ).

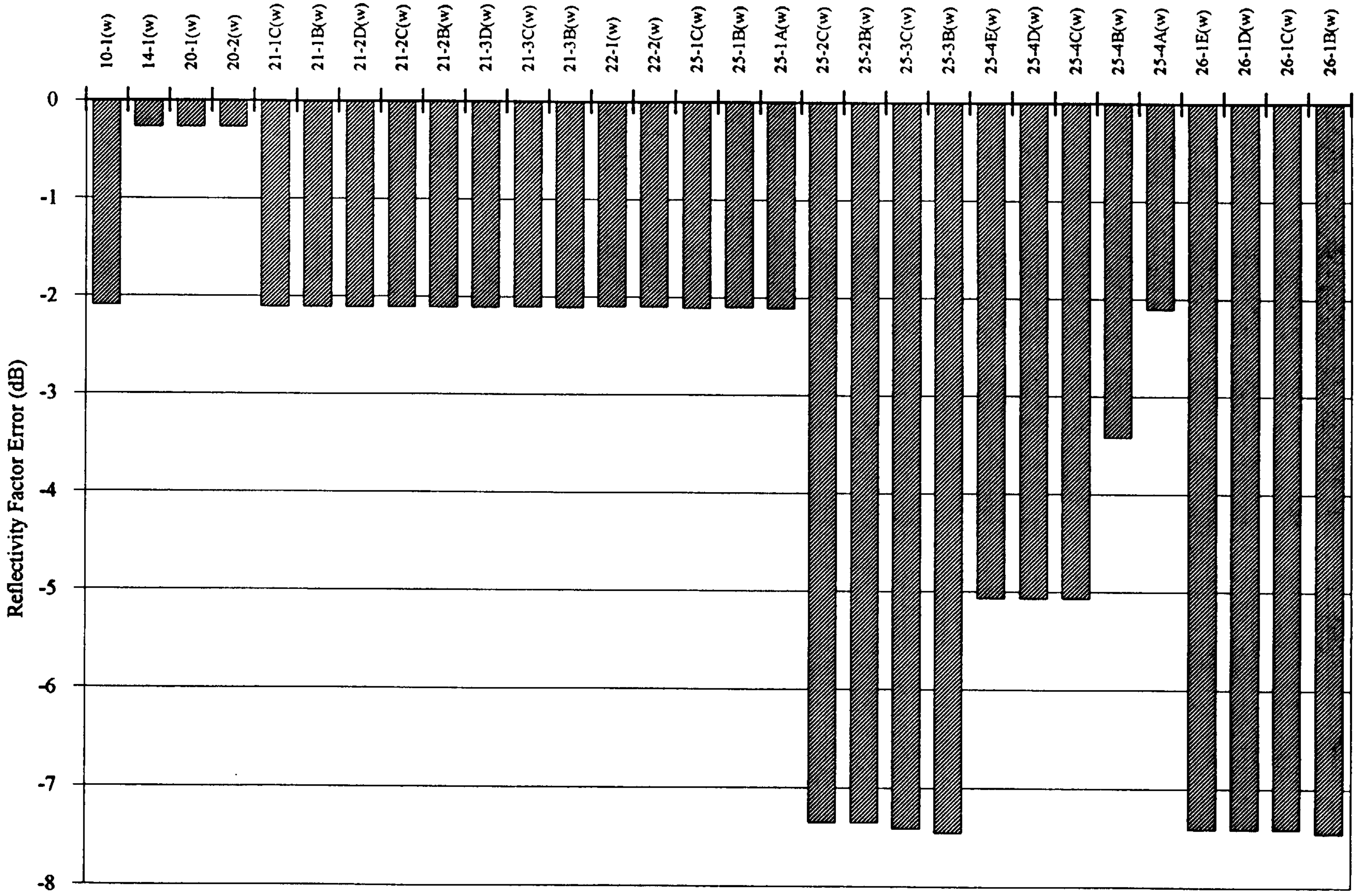

Figure 2.5 Comparison of reflectivity factor generated by Deirmendjian water clouds with Atlas/Bartoff model (2.43).

Table 2.10 summarizes the values shown in Figure 2.5 for all of the Deirmendjian water-cloud layers. The 18 layers which produce the least error have the smallest values of D_0, < 54 μm. This is in agreement with the range of median diameters seen in the data sets. Table 2.10 reveals (2.43) underestimates, by approximately the same amount as the data (i.e., < 2 dB), the reflectivity factor computed by the Deirmendjian model for small-droplet clouds. Thus, for the small-droplet clouds, the Deirmendjian model accurately models the data.

Table 2.10 Summary of Atlas/Bartoff underestimation of Deirmendjian water-cloud model reflectivity factors.

Number of Layers	Underestimation	Value of D_0
18	2.2 dB	54 μm
4	5.2 dB	275 μm
8	7.4 dB	500 μm

The layers with larger errors (cloud model numbers 25-2, 25-3, 25-4 and 26-1) have considerably higher values of D_0 (see Table 2.9) and are highly questionable since precipitation is known to occur with drop radii > 100 μm [Sauvageot, 1992]. This 100 μm threshold would imply an upper limit to (2.42) of $D_{\max} = 200$ μm. To arrive at values of Z within 2 dB of Z computed with $D_{\max} = \infty$ for these large-droplet clouds, $D_{\max}$ had to equal 2000 or 6000 μm. Although this is unrealistic for water clouds, it is not of much concern since in the Rayleigh region (2.27) indicates the extinction coefficient is proportional to the D^3 while (2.32) indicates that the backscatter coefficient is proportional to D^6. This implies that as the droplet radii increase, the backscatter cross-section becomes larger relative to the extinction cross-section, and the SNR increases. Thus the system sensitivity is limited by the small-droplet clouds. However these large-droplet cloud models also have increased water content which will limit the radar's sensitivity to rain beneath these clouds implying they can be used as a measure of how well the system can detect rain.

The range of values for Z within the 18 practical layers is -18.5 to 2.9 dBZ with D_0 equal to either 32.4 or 53.8 μm. A complete set of both Z and D_0 values is shown in

Table 2.9. It is interesting to note that only two sets of model parameters (i.e., r_C, C1, C2, and m_V), with the exception of m_V, are required for all 18 water-cloud layers. The above analysis indicates that the Deirmendjian model accurately represents the reflectivity factor for the thinner clouds, which is an important result given the minimum system SNR will depend on the returns from such clouds.

2.2.2.2 RAIN LAYERS

The drop-size distribution for rain has been studied by several authors [Laws, 1943, Wexler, 1948; Marshall, 1948; Best, 1950]. Among these, Law-Parsons and Marshall-Palmer distributions are the most widely used and compare reasonably well with one another [Ulaby, 1981]. Marshall and Palmer developed a drop-size distribution based on measurements made at the ground surface for rainfall rates between 1 and 23 $\mathrm{mm hr^{-1}}$. This distribution is given by

$$p(D) = N_o e^{-bD}, \qquad \mathrm{m^{-4}} \qquad (2.47)$$

where N_O is a constant equal to 8.0×10^6 $\mathrm{m^{-4}}$, D is the drop diameter in meters, and b is a variable related to the rain rate R_r by the equation

$$b = 4100 R_r^{-0.21}. \qquad (2.48)$$

Table 2.11 summarizes the comparison of the reflectivity factors generated with the Deirmendjian rain-cloud distributions and the Marshall-Palmer distribution, using (2.42).

Table 2.11 Comparison of reflectivity factor for Deirmendjian rain-cloud distribution and Marshall-Palmer distribution.

Cloud Type	R_r (mmhr^{-1})	Deirmendjian Rain Cloud Reflectivity Factor (dBZ)	Marshall-Palmer Rain Cloud Reflectivity Factor (dBZ)	Delta (dB)
21-1A(r)	0.2	7.2	14.4	-7.3
21-2A(r)	3	32.5	31.7	0.8
21-3A(r)	15	39.5	42.0	-2.5
25-2A(r)	2.4	38.5	30.3	8.2
25-3A(r)	12	45.5	40.6	4.9
26-1A(r)	150	85.2	56.7	28.6

Table 2.11 shows that only the cloud types 21-2A(r) and 21-3A(r) are within 3 dB of the Marshall-Palmer reflectivity factors, however, the first and last cloud type are not within the Marshall-Palmer model rain rate limits: 1 to 23 mmhr^{-1}. Although an uncertainty of 8.2 dB is large, ample SNR should be available from the rain returns at the lower frequencies due to the D^6 dependence of Z. As seen in the previous section, the large-droplet clouds (i.e., 25-2, 25-3, and 26-1) also provide excessive attenuation which aids in minimizing the effects of the over-estimated values of Z shown in Table 2.11.

The values for $D_{\max}$ used in (2.42) are given in Table 2.12.

Table 2.12 Values of $D_{\max}$ used in calculation of Table 2.11.

Cloud Type	$D_{\max}$ (μm)
21-1A(r)	400
21-2A(r)	4000
21-3A(r)	4000
25-2A(r)	6000
25-3A(r)	6000
26-1A(r)	50000

All values in Table 2.12 are reasonable with the exception of 26-1A(r), where $D_{\max} = 5$ cm!

2.2.2.3 ICE LAYERS

Ice crystals in clouds can attain sizes an order of magnitude larger than water droplets. Hence, the reflectivity factor of an ice cloud may be several orders of magnitude larger than that of a water cloud with the same liquid water content. Also, due to the extremely small value of Im(-K) shown in Table 2.2, the attenuation in ice clouds is negligible per (2.29). Because of these two factors, sufficient SNR should be obtainable from the ice clouds. Table 2.13 presents the reflectivity factors obtained for the Deirmendjian ice-cloud distributions using (2.42) and the listed values of $D_{\max}$.

Table 2.13 Summary of reflectivity factor for Deirmendjian ice-cloud distributions.

Cloud Type	$D_{\max}$ (μm)	Deirmendjian Ice Cloud Reflectivity Factor (dBZ)
1-A-1(i)	1000	6.2
1-M-1(i)	1000	6.2
1-T-1(i)	1000	6.2
26-1F(i)	1000	9.2

2.2.3 CALCULATIONS OF SNR

In the analysis of the SNR, six frequencies where evaluated: 94, 35, 24, 17, 14 and 10 GHz. Other parameters used in the SNR calculations were taken from the candidate system shown in Table 1.3, with the following exceptions:

1 - the altitude used is 525 km in an effort to remain compatible with the current design of the LAWS system,

2 - the transmitted power has increased to 6 kw,

3 - a rectangular antenna, 8×8 meter, was used for all frequencies except 94 GHz where a 3×3 meter antenna was employed. The smaller antenna size is required due to the manufacturing tolerances associated with an antennas of dimensions > 1000λ (@94 GHz, 1000λ = 3.2 m; @35 GHz, 1000λ = 8.6 m). The same gain and beamwidth values can be obtained with the 8 m diameter parabolic antenna but a rectangular antenna was introduced to facilitate the possible use of an 2-D electronically scanned array.

The gain of the antenna was calculated using the well known equation

$$G = \frac{4\pi}{\lambda^2} A \eta_a \tag{2.49}$$

where A is the physical area of the antenna, and η_a is the aperture efficiency factor set equal to 0.85. The beamwidths were determined from the equation

$$\beta = \sigma \beta_o \frac{\lambda}{L} \tag{2.50}$$

where $\sigma = 1.0693$ and $\beta_o = 1.057$ for a Taylor weighted -30 dB sidelobe level, $\bar{n} = 4$ antenna [Johnson, 1984]. Table 2.14 summarizes the gains and beamwidths for each of the frequencies studied. Note that the vertical and horizontal beamwidths will be equal due to the square shape of the antenna.

Table 2.14 Summary of antenna gains and beamwidths.

Frequency (GHz)	Antenna Size (m x m)	Antenna Gain (dB)	Beamwidths (mrad)
94	3 x 3	69.8	1.20
35	8 x 8	69.7	1.21
24	8 x 8	66.4	1.76
17	8 x 8	63.4	2.49
14	8 x 8	61.7	3.03
10	8 x 8	58.8	4.23

All SNR calculations were based on a nadir angle of 35°. This angle assures the worst case scenario of the two nadir angles due to the increased slant range to, and within, the clouds. The attenuation due to atmospheric gases was obtained by reading the zenith, one-way, attenuation values from Figure 2.2 and using (2.33). For the 35° nadir,

$$\mathrm{CSC}(\alpha) = \mathrm{CSC}(90^\circ - 35^\circ) = 1.221.$$

Table 2.15 summarize the two-way attenuation values used.

Table 2.15 Summary of atmospheric gas attenuation values.

Frequency (GHz)	One-Way Attenuation (Figure 2.2)	Total Two-Way Attenuation from (2.33)
94	1.00 dB	2.44 dB
35	0.30 dB	0.73 dB
24	0.35 dB	0.85 dB
17	0.105 dB	0.26 dB
14	0.07 dB	0.17 dB
10	0.055 dB	0.13 dB

The Propp SNR program was modified into two programs: one assuming the Rayleigh approximation (SNRVER6.FOR) and the other using Mie scattering (SNRVER7.FOR). Although all SNR data presented in this thesis are based on Mie scattering, the Rayleigh approximation is satisfied when $|n\chi| < 0.5$.

The values of the complex index of refraction for the water and rain clouds were obtained by the use of the Debye equation [Ulaby, 1986]. This equation determines the complex dielectric constant, ε, versus temperature and frequency and is related to n by (2.14). The value of n for the ice clouds was taken to be $1.78 - j0.003$ per (2.23) where the value for the Im(n) is set to a worst case value. Equation (2.17) is then employed to determine $|K|^2$ and Im($-K$) used in (2.29) and (2.32a) to obtain values for the volume-extinction coefficient and backscatter coefficient. Table A1 and A2 in Appendix A tabulate all volume-extinction coefficient and backscatter coefficient values for both Mie and Rayleigh scattering used in the SNR calculations at each frequency. For the two-way extinction coefficient, Table A1 indicates that ice and water clouds (water clouds with $D_{\max}$<200 μm) satisfy the Rayleigh requirements for all frequencies studied. Table A1 also shows that only at the lower frequencies will the rain conditions meet the Rayleigh criterion. For the backscattering coefficient, Table A2 indicates that both ice and water clouds satisfy the Rayleigh condition for all six frequencies and for the rain, up to 17 and possibly 24 GHz.

Finally, the volume-extinction coefficient and backscatter coefficient, in conjunction with parameters from Table 1.3, 2.14 and 2.15 are used in (2.39) to generate the SNR.

2.2.4 RESULTS

Using the SNRVER7.FOR program, Figures A1 to A17 of Appendix A were generated. These figures present the SNR versus altitude for each of the 17 Deirmendjian cloud types. Three of these figures are repeated in Figures 2.6, 2.7 and 2.8.

As expected, Figure 2.6 shows that the ice clouds provide ample SNR. This is caused by the larger ice particle diameters and negligible attenuation based on the small value of Im(-*K*) for ice. Figure 2.7 shows a fair-weather cumulus cloud and illustrates the layers generated by the Deirmendjian model. The higher frequencies appear to produce sufficient SNR throughout the entire cloud. Figure 2.8 provides an example of a cloud type containing rain. Again for the higher frequencies, a large SNR is produced within the water portion of the cloud while all frequencies provide > 20 dB SNR from rain return.

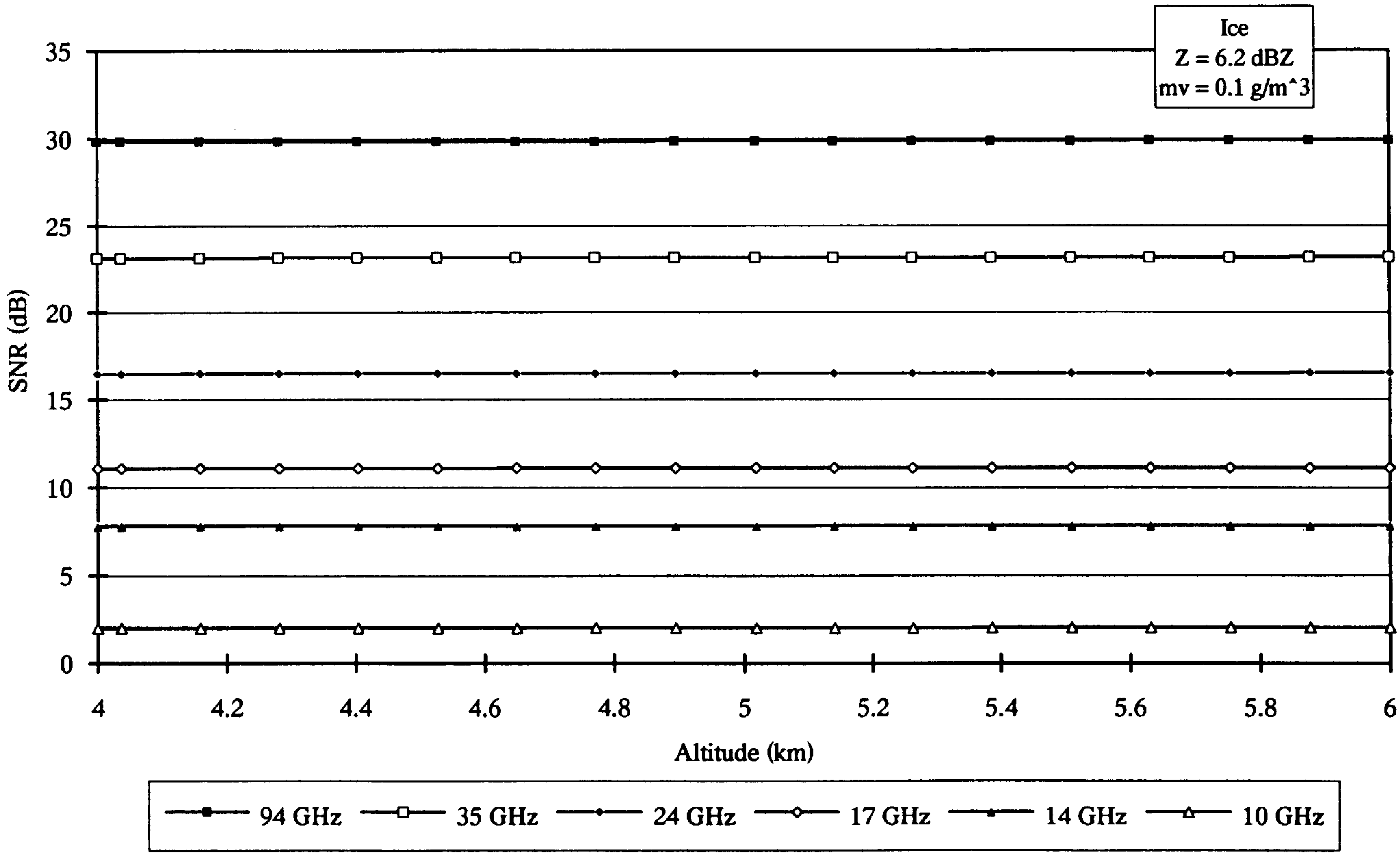

Figure 2.6 Mie SNR for Deirmendjian cloud model: 1-A-1, Cirrostratus.

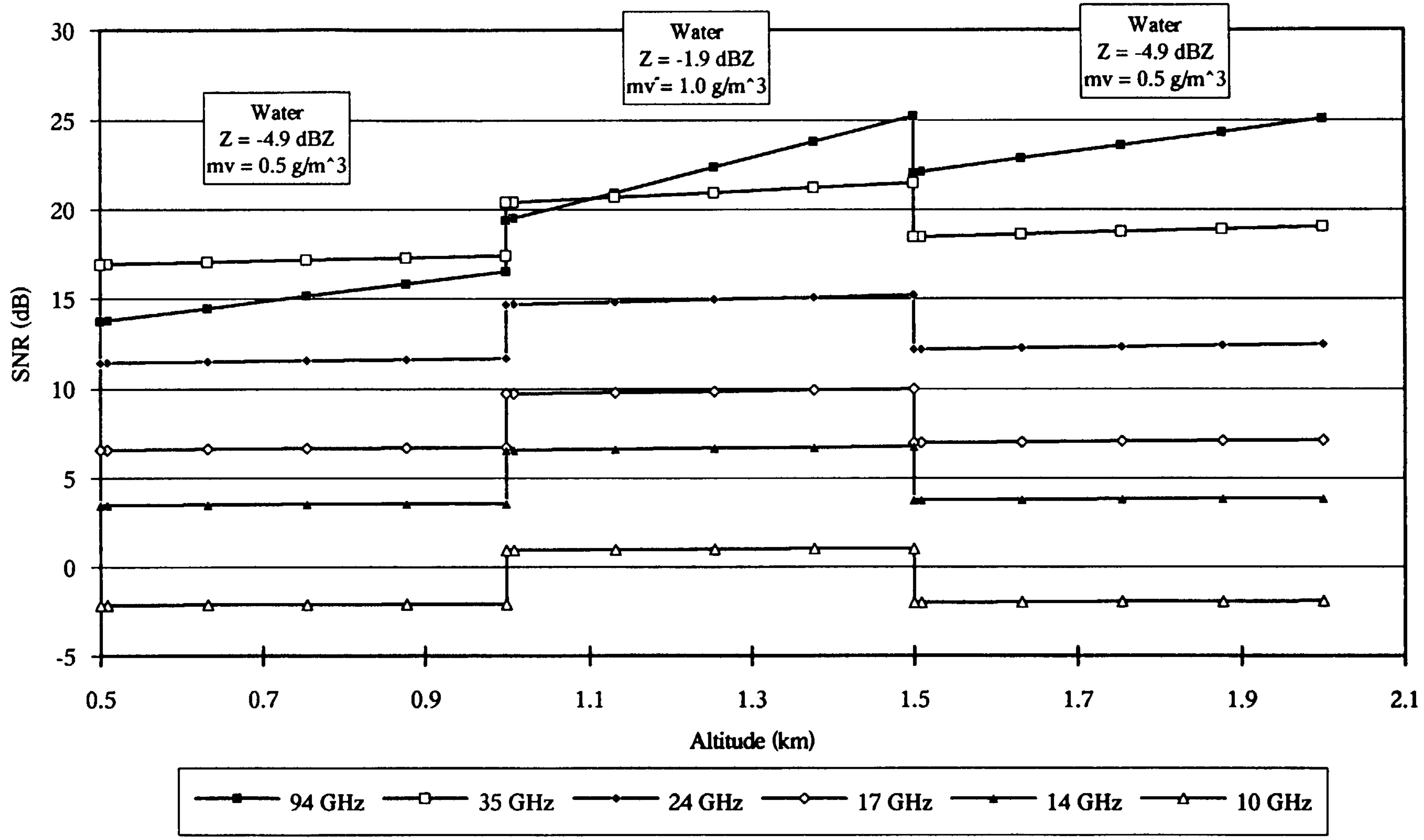

Figure 2.7 Mie SNR for Deirmendjian cloud model: 25-1, Fair Weather Cumulus.

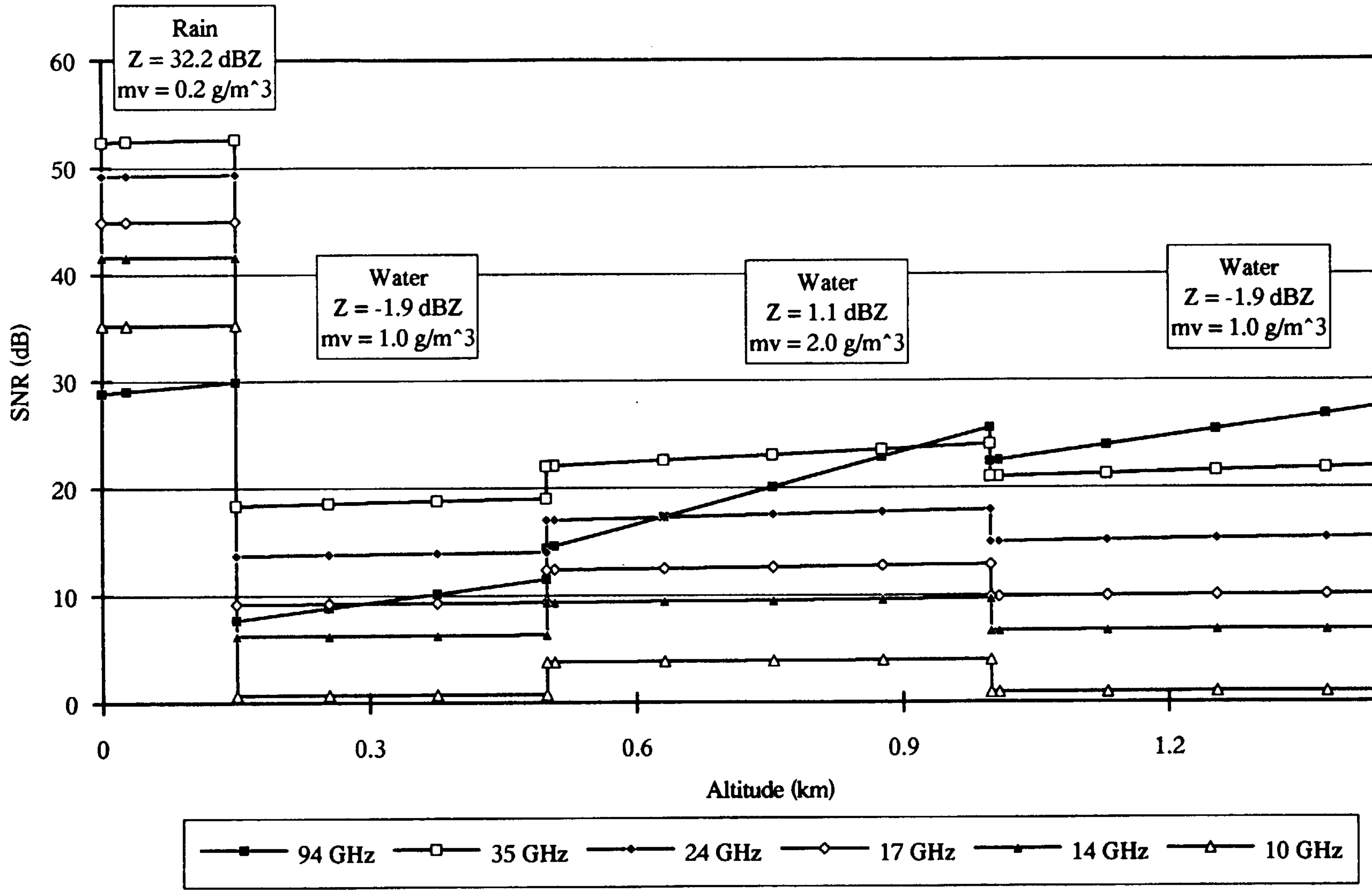

Figure 2.8 Mie SNR for Deirmendjian cloud model: 21-2, Steady Rain, 3 mm/hr.

To choose an optimal frequency, some form of presentation was required to compare all cloud types for each frequency, simultaneously. To this end, each cloud layer at each frequency was threshold detected and the results displayed in a table format. SNR thresholds of 5, 10, 15 and 20 dB were used to create Tables 2.16, 2.17, 2.18, and 2.19. These tables show for which frequency a cloud layer exceeds the threshold (indicated by a "X"), cross the threshold (indicated by a "P"), or is below the threshold (indicated by a "-").

As can be seen in these tables, the SNR from the rain layers is sufficient for the lower frequencies even with the 20 dB threshold, with the exception of the light rain (drizzle) of model 21-1. This was predicted in section 2.2.2.2. The discussion of ample SNR for ice clouds in section 2.2.2.3 is also realized in that these clouds produce sufficient SNR even at the 20 dB threshold with 94 or 35 GHz. The statement that the thinner clouds set the lower limit on the system SNR sensitivity can also be seen in these tables. The large-droplet clouds (25-2, 25-3, 25-4 and 26-1) even exceed the 20 dB SNR threshold, indicating they are not significant to the determination of the lower SNR limit. The clouds most instrumental in determining the minimum SNR are the Altocumulus (10-1 and 14-1) and the Low-Lying Stratus (20-1 and 20-2). Due to their minimal water content (0.15 and 0.25 gm^{-3}), these clouds exhibit the smallest values of reflectivity factor (as low as -18.5 dB*Z*) as compared to the other cloud types. Only the 94 GHz frequency achieves a > 10 dB SNR for these clouds. This implies the 94 GHz frequency is required to provide adequate SNR for the thinnest clouds. If only one frequency is utilized, 24 GHz gives the best overall performance. The combination of 94 and 24 GHz provides the best overall two-frequency performance.

Table 2.16 SNR threshold of 20 dB.

Cloud	Cloud Name	94 GHz	35 GHz	24 GHz	17 GHz	14 GHz	10 GHz
1-A-1(i)	Cirrostratus	X	X	-	-	-	-
1-M-1(i)	Cirrostratus	X	X	-	-	-	-
1-T-1(i)	Cirrostratus	X	X	-	-	-	-
10-1(w)	Altocumulus	-	-	-	-	-	-
14-1(w)	Altocumulus	-	-	-	-	-	-
20-1(w)	Low-Lying Stratus	-	-	-	-	-	-
20-2(w)	Low-Lying Stratus	-	-	-	-	-	-
21-1C(w)	Drizzle, 0.2 mm/hr	X	X	-	-	-	-
21-1B(w)		P	X	-	-	-	-
21-1A(r)		P	X	X	-	-	-
21-2D(w)	Steady Rain, 3 mm/hr	X	X	-	-	-	-
21-2C(w)		P	X	-	-	-	-
21-2B(w)		-	-	-	-	-	-
21-2A(r)		X	X	X	X	X	X
21-3D(w)	Steady Rain, 15 mm/hr	P	P	-	-	-	-
21-3C(w)		-	-	-	-	-	-
21-3B(w)		-	-	-	-	-	-
21-3A(r)		-	X	X	X	X	X
22-1(w)	Stratocumulus	X	-	-	-	-	-
22-2(w)	Stratocumulus	P	-	-	-	-	-
25-1C(w)	Fair Weather Cumulus	X	-	-	-	-	-
25-1B(w)		P	X	-	-	-	-
25-1A(w)		-	-	-	-	-	-
25-2C(w)	Cumulus, 2.4 mm/hr	P	X	X	X	X	X
25-2B(w)		-	X	X	X	X	X
25-2A(r)		-	X	X	X	X	X
25-3C(w)	Cumulus, 12 mm/hr	P	P	X	X	X	X
25-3B(w)		-	P	X	X	X	X
25-3A(r)		-	-	X	X	X	X
25-4E(w)	Cumulus Congestus	X	X	X	X	X	X
25-4D(w)		X	X	X	X	X	X
25-4C(w)		X	X	X	X	X	X
25-4B(w)		-	X	X	-	-	-
25-4A(w)		-	-	-	-	-	-
26-1F(i)	Cumulonimbus, 150 mm/hr	X	X	-	-	-	-
26-1E(w)		P	X	X	X	X	X
26-1D(w)		-	P	P	X	X	X
26-1C(w)		-	-	-	P	P	X
26-1B(w)		-	-	-	-	X	X
26-1A(r)		-	-	-	X	X	X

Table 2.17 SNR threshold of 15 dB.

Cloud	Cloud Name	94 GHz	35 GHz	24 GHz	17 GHz	14 GHz	10 GHz
1-A-1(i)	Cirrostratus	X	X	X	-	-	-
1-M-1(i)	Cirrostratus	X	X	X	-	-	-
1-T-1(i)	Cirrostratus	X	X	X	-	-	-
10-1(w)	Altocumulus	X	-	-	-	-	-
14-1(w)	Altocumulus	-	-	-	-	-	-
20-1(w)	Low-Lying Stratus	-	-	-	-	-	-
20-2(w)	Low-Lying Stratus	-	-	-	-	-	-
21-1C(w)	Drizzle, 0.2 mm/hr	X	X	-	-	-	-
21-1B(w)		P	X	X	-	-	-
21-1A(r)		P	X	X	X	X	-
21-2D(w)	Steady Rain, 3 mm/hr	X	X	-	-	-	-
21-2C(w)		P	X	X	-	-	-
21-2B(w)		-	X	-	-	-	-
21-2A(r)		X	X	X	X	X	X
21-3D(w)	Steady Rain, 15 mm/hr	P	P	P	-	-	-
21-3C(w)		-	-	-	-	-	-
21-3B(w)		-	-	-	-	-	-
21-3A(r)		-	X	X	X	X	X
22-1(w)	Stratocumulus	X	X	-	-	-	-
22-2(w)	Stratocumulus	X	X	-	-	-	-
25-1C(w)	Fair Weather Cumulus	X	X	-	-	-	-
25-1B(w)		X	X	-	-	-	-
25-1A(w)		-	X	-	-	-	-
25-2C(w)	Cumulus, 2.4 mm/hr	P	X	X	X	X	X
25-2B(w)		-	X	X	X	X	X
25-2A(r)		-	X	X	X	X	X
25-3C(w)	Cumulus, 12 mm/hr	P	X	X	X	X	X
25-3B(w)		-	X	X	X	X	X
25-3A(r)		-	X	X	X	X	X
25-4E(w)	Cumulus Congestus	X	X	X	X	X	X
25-4D(w)		X	X	X	X	X	X
25-4C(w)		X	X	X	X	X	X
25-4B(w)		P	X	X	X	X	-
25-4A(w)		-	-	-	-	-	-
26-1F(i)	Cumulonimbus, 150 mm/hr	X	X	X	-	-	-
26-1E(w)		P	X	X	X	X	X
26-1D(w)		-	P	P	X	X	X
26-1C(w)		-	-	P	P	X	X
26-1B(w)		-	-	-	P	X	X
26-1A(r)		-	-	-	X	X	X

Table 2.18 SNR threshold of 10 dB.

Cloud	Cloud Name	94 GHz	35 GHz	24 GHz	17 GHz	14 GHz	10 GHz
1-A-1(i)	Cirrostratus	X	X	X	X	-	-
1-M-1(i)	Cirrostratus	X	X	X	X	-	-
1-T-1(i)	Cirrostratus	X	X	X	X	-	-
10-1(w)	Altocumulus	X	X	-	-	-	-
14-1(w)	Altocumulus	X	-	-	-	-	-
20-1(w)	Low-Lying Stratus	X	-	-	-	-	-
20-2(w)	Low-Lying Stratus	X	-	-	-	-	-
21-1C(w)	Drizzle, 0.2 mm/hr	X	X	X	P	-	-
21-1B(w)		X	X	X	X	-	-
21-1A(r)		X	X	X	X	X	-
21-2D(w)	Steady Rain, 3 mm/hr	X	X	X	P	-	-
21-2C(w)		X	X	X	X	-	-
21-2B(w)		P	X	X	-	-	-
21-2A(r)		X	X	X	X	X	X
21-3D(w)	Steady Rain, 15 mm/hr	P	X	X	X	-	-
21-3C(w)		-	P	X	X	-	-
21-3B(w)		-	-	-	-	-	-
21-3A(r)		-	X	X	X	X	X
22-1(w)	Stratocumulus	X	X	-	-	-	-
22-2(w)	Stratocumulus	X	X	-	-	-	-
25-1C(w)	Fair Weather Cumulus	X	X	X	-	-	-
25-1B(w)		X	X	X	-	-	-
25-1A(w)		X	X	X	-	-	-
25-2C(w)	Cumulus, 2.4 mm/hr	P	X	X	X	X	X
25-2B(w)		-	X	X	X	X	X
25-2A(r)		-	X	X	X	X	X
25-3C(w)	Cumulus, 12 mm/hr	P	X	X	X	X	X
25-3B(w)		-	X	X	X	X	X
25-3A(r)		-	X	X	X	X	X
25-4E(w)	Cumulus Congestus	X	X	X	X	X	X
25-4D(w)		X	X	X	X	X	X
25-4C(w)		X	X	X	X	X	X
25-4B(w)		X	X	X	X	X	X
25-4A(w)		-	X	X	-	-	-
26-1F(i)	Cumulonimbus, 150 mm/hr	X	X	X	X	X	-
26-1E(w)		P	X	X	X	X	X
26-1D(w)		-	P	X	X	X	X
26-1C(w)		-	-	P	P	X	X
26-1B(w)		-	-	-	X	X	X
26-1A(r)		-	-	-	X	X	X

Table 2.19 SNR threshold of 5 dB.

Cloud	Cloud Name	94 GHz	35 GHz	24 GHz	17 GHz	14 GHz	10 GHz
1-A-1(i)	Cirrostratus	X	X	X	X	X	-
1-M-1(i)	Cirrostratus	X	X	X	X	X	-
1-T-1(i)	Cirrostratus	X	X	X	X	X	-
10-1(w)	Altocumulus	X	X	X	-	-	-
14-1(w)	Altocumulus	X	P	-	-	-	-
20-1(w)	Low-Lying Stratus	X	X	-	-	-	-
20-2(w)	Low-Lying Stratus	X	X	-	-	-	-
21-1C(w)	Drizzle, 0.2 mm/hr	X	X	X	X	X	-
21-1B(w)		X	X	X	X	X	-
21-1A(r)		X	X	X	X	X	X
21-2D(w)	Steady Rain, 3 mm/hr	X	X	X	X	X	-
21-2C(w)		X	X	X	X	X	-
21-2B(w)		X	X	X	X	X	-
21-2A(r)		X	X	X	X	X	X
21-3D(w)	Steady Rain, 15 mm/hr	P	X	X	X	X	-
21-3C(w)		-	X	X	X	X	-
21-3B(w)		-	P	X	X	X	-
21-3A(r)		-	X	X	X	X	X
22-1(w)	Stratocumulus	X	X	X	-	-	-
22-2(w)	Stratocumulus	X	X	X	-	-	-
25-1C(w)	Fair Weather Cumulus	X	X	X	X	-	-
25-1B(w)		X	X	X	X	X	-
25-1A(w)		X	X	X	X	-	-
25-2C(w)	Cumulus, 2.4 mm/hr	P	X	X	X	X	X
25-2B(w)		-	X	X	X	X	X
25-2A(r)		-	X	X	X	X	X
25-3C(w)	Cumulus, 12 mm/hr	P	X	X	X	X	X
25-3B(w)		-	X	X	X	X	X
25-3A(r)		-	X	X	X	X	X
25-4E(w)	Cumulus Congestus	X	X	X	X	X	X
25-4D(w)		X	X	X	X	X	X
25-4C(w)		X	X	X	X	X	X
25-4B(w)		X	X	X	X	X	X
25-4A(w)		-	X	X	-	-	-
26-1F(i)	Cumulonimbus, 150 mm/hr	X	X	X	X	X	X
26-1E(w)		P	X	X	X	X	X
26-1D(w)		-	P	X	X	X	X
26-1C(w)		-	-	P	X	X	X
26-1B(w)		-	-	-	X	X	X
26-1A(r)		-	-	-	X	X	X

CHAPTER 3

MEAN-FREQUENCY ESTIMATION, RADAR AMBIGUITIES AND TRANSMITTED WAVEFORM

3.1 WEATHER ECHO AND POWER SPECTRAL DENSITY

A vector summation of the scattered electric fields from a large number of particles defines the weather radar echo. The voltage received from such an echo is given by

$$V = \sum_{i=0}^{N} V_i e^{j2kR_i} \qquad (3.1)$$

where V_i and R_i are the voltage and range corresponding to the i^{th} scatterer, k is the wavenumber ($k=2\pi/\lambda$), and N the total number of scatterers. Due to the random position of the scatterers, the phase, $j2kR_i$, will be random in nature and assumed uniformly distributed over the range $[0,2\pi]$. The central limit theorem states the sum of n independent identical distributed random variables tends to have a limiting (as $n \rightarrow \infty$) distribution that is Gaussian with a mean equal to the sum of the individual means and a variance equal to the sum of the individual variances. Hence, the resultant voltage, V, will tend to have a Gaussian distribution [Shanmugan, 1988]. For weather echoes, the individual means equal zero, i.e.,

$$\mathrm{E}\{V_i\}\frac{1}{2\pi}\int_0^{2\pi} e^{j2\pi kR_i}\,dR_i = 0, \qquad i = 0, 1, 2, \ldots, N \qquad (3.2)$$

which implies $E\{V\} = 0$. Thus, weather echoes will have a Gaussian probability density function with zero-mean and a variance determined by the sum of the variances of the individual scatterers.

An important function used to characterize radar returns is the power spectral density (PSD). The PSD is a function of a number of factors including the reflectivity, illumination factor (defined by the antenna pattern and range weighting functions), turbulence, and wind shear. For uniform reflectivity and uniform shear, the PSD shape is largely determined by the illuminating factor, assumed Gaussian. The spectrum's variance, σ_S^2, is considered the sum of the variances contributed by wind shear, antenna motion, turbulence and other factors [Doviak, 1984]. Figure 3.1 illustrates the received echo power spectral density $S(v)$.

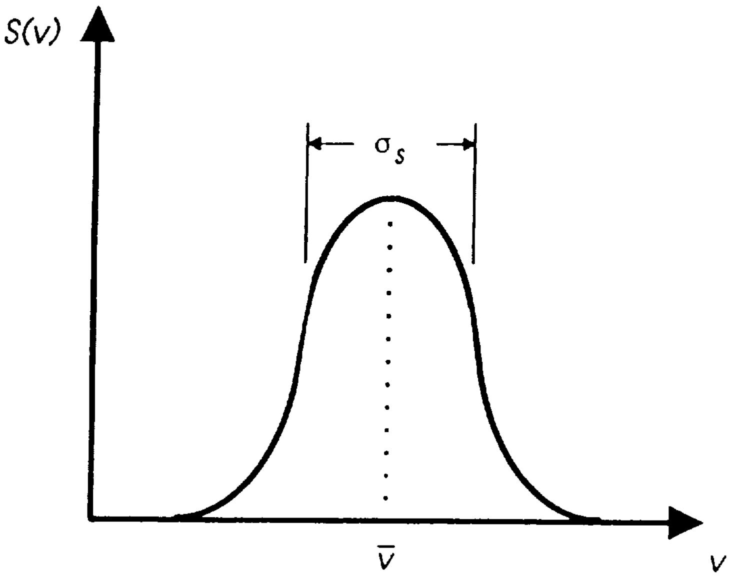

Figure 3.1 Radar return Doppler spectrum.

Knowledge of the PSD allows determination of other parameters such as the received power, mean velocity and velocity spectrum variance. The zero moment of $S(v)$ yields the received power:

$$P_r = \int S(v)dv. \tag{3.3}$$

The mean velocity is given by the first moment of the spectrum,

$$\bar{v} = \frac{\int vS(v)dv}{\int S(v)dv}, \tag{3.4}$$

and the spectrum variance is obtained from the second central moment,

$$\sigma_S^2 = \frac{\int (v - \bar{v})^2 S(v) dv}{\int S(v) dv}, \tag{3.5}$$

where σ_S is the velocity width. The first and second moments are analogous to the expected value and variance, respectively, with a non-normalized probability density function $S(v)$ [Skolnik, 1990]. Substitution of the equation

$$f = \frac{2v}{\lambda}, \tag{3.6}$$

produces solutions of (3.3), (3.4) and (3.5) in terms of the Doppler frequency. When used in weather observations, the zero moment, or echo power, can be an indicator of liquid water content or precipitation rate in the resolution volume. The first and second moments allow for the measurement of the mean velocity and spectral width of the returned signal.

Several moment estimators have been developed to estimate accurately the values given by (3.3), (3.4) and (3.5). In most cases, the return signal is digitized into complex components, I (in-phase, real) and Q (quadrature-phase, imaginary). The use of the fast Fourier transform (FFT) can then provide an estimate of the Doppler spectrum. Xin studied the FFT, auto-regression and covariance estimators to determine the most accurate mean-frequency estimator. He concluded that a covariance estimator (or pulse-pair estimator) produces the least error for a symmetric PSD [Xin, 1990]. The mean estimate given by the covariance estimator is an unbiased estimate of the signal mean even with low values of SNR for symmetric spectra. The mean-estimate bias due to non-symmetric spectra has been studied and shown not to be a serious problem for the covariance estimator [Sirmans, 1975]. The next section concerns the development of the covariance estimator.

3.2 COVARIANCE ESTIMATOR

The autocovariance of a random variable $X(t)$, is defined as

$$C_{XX}(t_1,t_2) \equiv R_{XX}(t_1,t_2) - \mu_X^*(t_1)\mu_X(t_2) \qquad (3.7)$$

where R_{XX} is the autocorrelation of $X(t)$ given by

$$R_{XX}(t_1,t_2) = E\{X^*(t_1)X(t_2)\} = \int X^*(t_1)X(t_2)f(t_1,t_2)dt_1dt_2, \qquad (3.8)$$

$f(t_1,t_2)$ being the joint probability density function, and μ_X the expected value of $X(t)$. If the autocorrelation depends only on a time difference (i.e., t_1-t_2) and the mean is independent of time, the process is considered wide-sense-stationary (WSS) and (3.8) becomes

$$R_{XX}(\tau) = E\{X^*(t)X(t+\tau)\} = \int X^*(t)X(t+\tau)f(\tau)dt, \qquad (3.9)$$

with μ_X equal to a constant [Shanmugan, 1988]. As mentioned in section 3.1, the weather return signal is statistically Gaussian with zero-mean, μ_X=0; thus from (3.7), the autocovariance equals the autocorrelation. With this, another important property of WSS processes, based on the Wiener-Khinchine relationship, can be utilized. This relation states the autocorrelation function can be obtained from the inverse Fourier transform of the power spectral density:

$$R_{XX}(\tau) = F^{-1}\{S_{XX}(f)\} = \int_{-\infty}^{\infty} S_{XX}(f)\exp(j2\pi f\tau)df. \qquad (3.10)$$

In a radar application, the autocorrelation is obtained from the sampled returns. Each range gate will produce a sequence of complex video samples $V(kT_S)$, where T_S is the pulse repetition time. Each sample can be written as

$$V(kT_s) = V_k + n_k, \qquad k = 0,\ 1,\ \ldots,\ L, \qquad (3.11a)$$

or, $$V(kT_s) = s_k e^{j\omega_d kT_s} + n_k, \qquad k = 0, 1, ..., L, \qquad (3.11b)$$

where V_k is the weather echo sample given by (3.1) for range gate k, s_k is the weather echo sample with spectra centered at zero, n_k is the white noise sample, and L is the total number of range gates. Both s_k and n_k are zero-mean Gaussian processes. Letting S be the average signal power and ρ the normalized correlation function, the autocorrelation function of the process $V(kT_s)$ is

$$R(mT_s) = E\{V^*(kT_s)\, V[(k+m)T_s]\} = S\rho(mT_s)e^{j\omega_d mT_s} + N_p\delta_m, \qquad (3.12)$$

where N_p is defined as the mean white noise power. The difficulty in determining the autocorrelation using (3.12) is in obtaining the normalized correlation function. An alternative approach is to utilize (3.10) and the PSD. The Doppler spectrum will have a Gaussian shape, as discussed in section 3.1, of the form

$$S(v) = \frac{S}{\sqrt{(2\pi)}\sigma_s}\exp\left(-\frac{(v-\bar{v})^2}{2\sigma_s^2}\right) + \frac{2N_pT_s}{\lambda}. \qquad (3.13)$$

Substitution (3.13) into (3.10), yields

$$R(mT_s) = S\exp\left\{-8\left(\frac{\pi\sigma_s mT_s}{\lambda}\right)^2\right\}e^{j4\pi\bar{v}mT_s/\lambda} + N_p\delta_m. \qquad (3.14)$$

A comparison of (3.12) and (3.14) identifies the correlation function as

$$\rho(mT_s) = \exp\left\{-8\left(\frac{\pi\sigma_s mT_s}{\lambda}\right)^2\right\}. \qquad (3.15)$$

It is easy to see that the mean velocity can be obtained from the argument of (3.14):

$$arg[R(mT_s)] = \frac{4\pi\bar{v}mT_s}{\lambda}, \qquad (3.16)$$

or, solving for $\bar{v}$ and letting $m = 1$,

$$\bar{v} = (\lambda / 4\pi T_s)\arg[R(T_s)], \tag{3.17a}$$

and

$$\bar{f} = (1 / 2\pi T_s)\arg[R(T_s)]. \tag{3.17b}$$

Equation (3.17) constitutes the covariance mean-frequency estimator and can be interpreted by reviewing the operation of an FFT. Figure 3.2(a) illustrates the continuous Doppler return from a target and the associated complex radar I&Q samples. Each of these samples contains amplitude and phase information of the return signal and they are spaced T_S seconds apart. The diagrams in Figure 3.2(b) depict a rotating phasor produced by the sequence of N I&Q samples.

The phasor produced by the I&Q data will rotate at an angular frequency of $\Delta\phi$ radians per T_S seconds:

$$\omega_d = \frac{\Delta\phi}{T_s}, \tag{3.18a}$$

or,

$$f_d = \frac{\Delta\phi}{2\pi T_s}. \tag{3.18b}$$

The FFT, simply stated, creates a digital bank of N phasors each rotating at different rates corresponding to a particular frequency. A comparison is then made between each FFT phasor and the phasor defined by the N I&Q samples. If the I&Q phasor correlates well with a particular FFT phasor, the output of that bank (or frequency bin) is large, conversely if there is poor correlation, the output is small. Thus, the output of the FFT bins will produce the spectrum of the I&Q input data. The covariance estimator determines the mean-frequency by calculating the change in phase, $\Delta\phi$, between successive samples, and then uses (3.18b) to obtain the frequency. A comparison of (3.18b) and (3.17b) reveals the argument of the autocorrelation function at time lag T_S, is equal to the change in phase over the time interval T_S. This is not surprising since the autocorrelation function by definition yields the differences between a function and itself translated in time (see equation (3.9)). For the

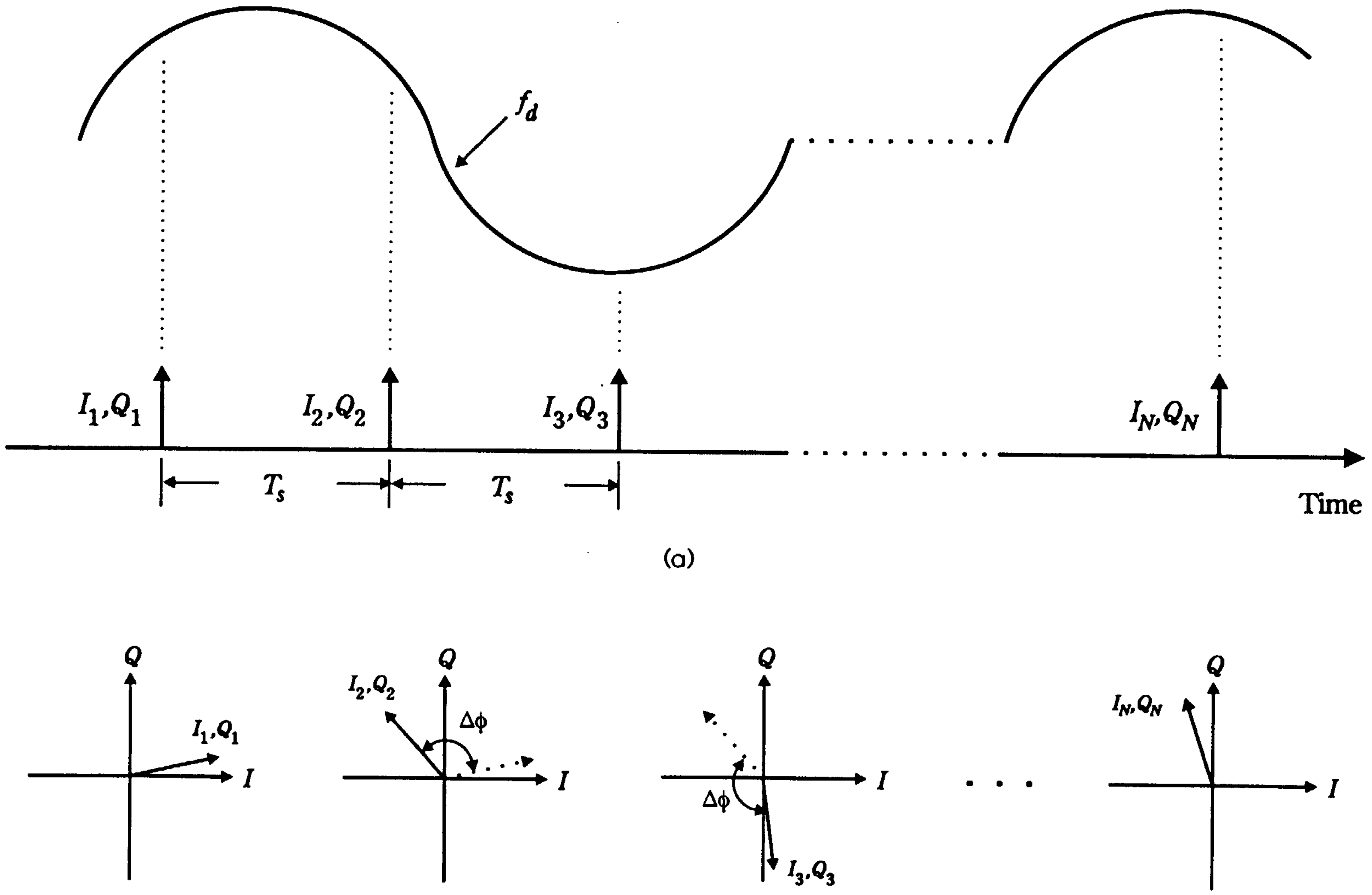

(a)

(b)

Figure 3.2 (a) Continuous Doppler return, (b) phasor representation of radar return with evenly spaced samples.

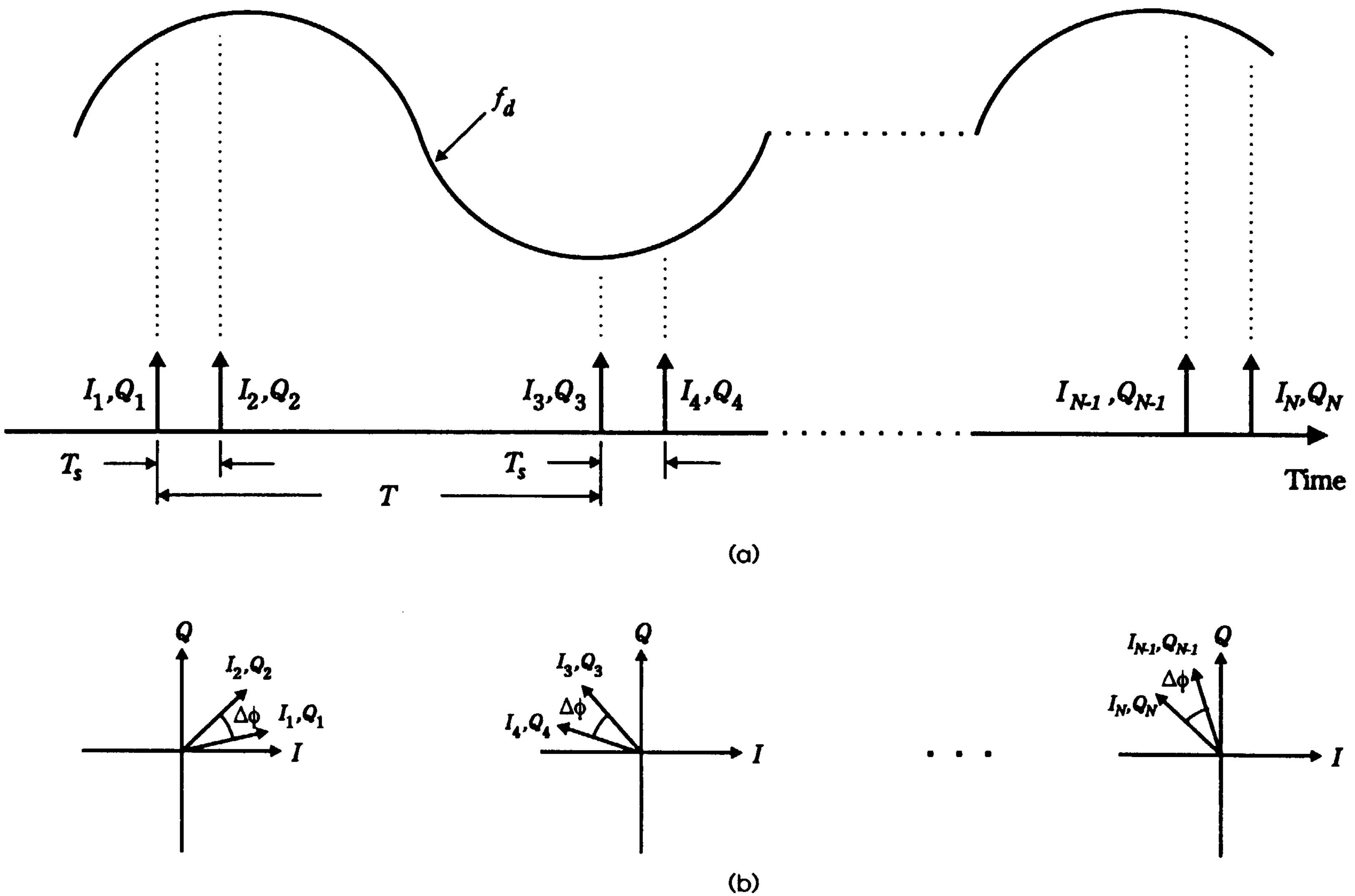

(a)

(b)

Figure 3.3 (a) Continuous Doppler return, (b) phasor representation of radar return with unevenly spaced samples.

covariance estimator, the time between samples need not be uniform. Figure 3.3 depicts the same process shown in Figure 3.2 for a non-uniform sampling interval.

One advantage of the covariance estimator is the returns only need to be correlated for a shorter time (i.e., T_S) as compared to the FFT process that requires correlation during the entire look (i.e., NT_S).

Although (3.17) implies the frequency can be determined from only two samples (one pulse-pair) of the returned signal, the variance of such a measurement would be unacceptable. A large number of independent samples (a sample here being one $\Delta\phi$ measurement) is necessary to provide an acceptable mean frequency variance. If the samples are independent, the estimated variance, $\hat{\sigma}^2$, decreases as

$$\hat{\sigma}^2 = \frac{\sigma^2}{M}, \qquad (3.19)$$

where σ^2 is a single sample estimate variance, and M is the number of independent samples. However, because correlation can exist between samples, (3.19) does not always hold. The effective estimate-variance reduction factor for M samples is given by [Doviak, 1984]

$$\frac{\hat{\sigma}^2}{\sigma^2} = \frac{1}{M_e} = \sum_{m=-(M-1)}^{M-1} \frac{M-|m|}{M^2}\rho(mT). \qquad (3.20)$$

A perturbation analysis has been derived for the variance of the mean velocity for the pulse-pair estimator. The condition required for this analysis to be valid are:

$$\frac{4\pi M\sigma_S T_S}{\lambda} >> 1, \qquad (3.21)$$

$$\rho^2(T_s)M >> (N/S+1)^2, \qquad (3.22)$$

and the power spectral density is Gaussian. Condition (3.21) expresses the requirement for a large number of independent samples, while (3.22) ensures that the argument of $R(T_S)$ has a distribution width small compared to 2π. If these condition are valid, and $T_S<T$, the variance of the mean velocity can be expressed as

$$var(\hat{v}) \approx \lambda^2 [32\pi^2 M\rho^2(T_s)T_s^2]^{-1} \left\{ \left([1-\rho^2(T_s)]\lambda \right) \Big/ \left(4\sigma_s T\sqrt{\pi} \right) \right.$$
$$\left. + N^2/S^2 + 2(N/S) \right\} \qquad (3.23)$$

where T_S and T are defined in Figure 3.3 [Doviak, 1984]. As will be shown in the next chapter, the determination of the variance plays an important role characterizing the antenna scan pattern.

3.3 RADAR AMBIGUITIES

To determine the limits for T_S and T, the range and velocity ambiguities must be analyzed. Continuous wave (CW) radars measure all Doppler frequency returns unambiguously but not range. Pulse-Doppler radars provide simultaneous range and velocity measurements but have a Doppler aliasing ambiguity based on the Nyquist sampling rate. The unambiguous range for a coherent pulsed radar is given by

$$R_u = \frac{cT_s}{2} \qquad (3.24)$$

where c is the speed of light. Returns from ranges greater than R_u are received as multiple trip returns and are overlaid with echoes from targets within $R_u = cT_S/2$.

Doppler frequencies are ambiguous because one cannot distinguish between the real Doppler shifts and those aliases spaced in frequency by the pulse repetition frequency (PRF). To be unambiguous in frequency, the Doppler frequencies must adhere to the Nyquist criterion:

$$f_u = \pm\frac{1}{2T_s}, \qquad (3.25a)$$

or in terms of velocity, $$V_u = \pm \frac{\lambda}{4T_s}. \quad (3.25b)$$

Thus the range-velocity product,

$$R_u V_u = \frac{c\lambda}{8}, \quad (3.26)$$

specifies the ambiguity resolution capabilities for a conventional (i.e., uniform pulse spacing) Doppler radar. It is desirable to choose a large value of T_S to eliminate second and higher order trips. However, the sampling rate is limited in that the samples must remain correlated for precise Doppler shift measurements. Correlation exists when [Atlas, 1964]

$$\frac{\lambda}{2T_s} >> \sigma_S \quad (3.27)$$

where σ_S is the velocity-spectrum width defined as the square root of the spectrum's second moment (3.5). Condition (3.27) indicates that the Doppler width must be much smaller than the Nyquist interval, $\lambda/2T_S$, to prevent aliasing, where the Nyquist interval limits the maximum radial velocity, V_{mr}. What is more significant is the effect of the sampling rate on the variance of the estimate. The variance given in (3.23) reduces to

$$\mathrm{var}(\hat{v}) \approx \frac{\sigma_S \lambda e^{\left[(4\pi\sigma_S T_S/\lambda)^2\right]}}{8\sqrt{\pi}MT}, \quad (3.28)$$

for large values of SNR [Zrnic, 1977]. Evaluation of (3.28) reveals that

$$\frac{4\pi\sigma_S T_S}{\lambda} \leq 1 \quad (3.29)$$

is necessary to prevent the variance from increasing exponentially. This results in a sampling limit of

$$\frac{\lambda}{2T_s} \geq 2\pi\sigma_v \qquad (3.30)$$

as a condition to maintain signal sample correlation [Zrnic, 1977]. Comparing (3.30) with (3.27) indicates sampling at $(1/2\pi)$ of the Nyquist rate $(\lambda/2T_S)$ may allow for a tolerable variance. It is important to realize violating (3.30) does not necessarily produce unacceptable results; it merely implies a rapid decrease in correlation and an exponentially increasing variance.

3.4 TRANSMIT WAVEFORM

The modulation pulse-pair waveform developed by Xin consists of the first pulse in the pulse-pair being up-chirped while the second is down-chirped. The chirp modulation allows for a lower peak power requirement and extends the unambiguous range of the pulse-pairs. Figure 3.4 presents this waveform and Figure 3.5 illustrates a receiver block diagram capable of decoding such a waveform.

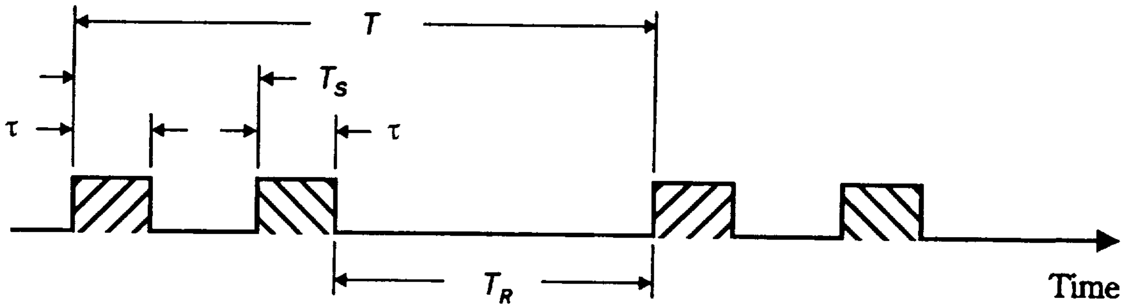

Figure 3.4 RAWS modulated pulse-pair waveform.

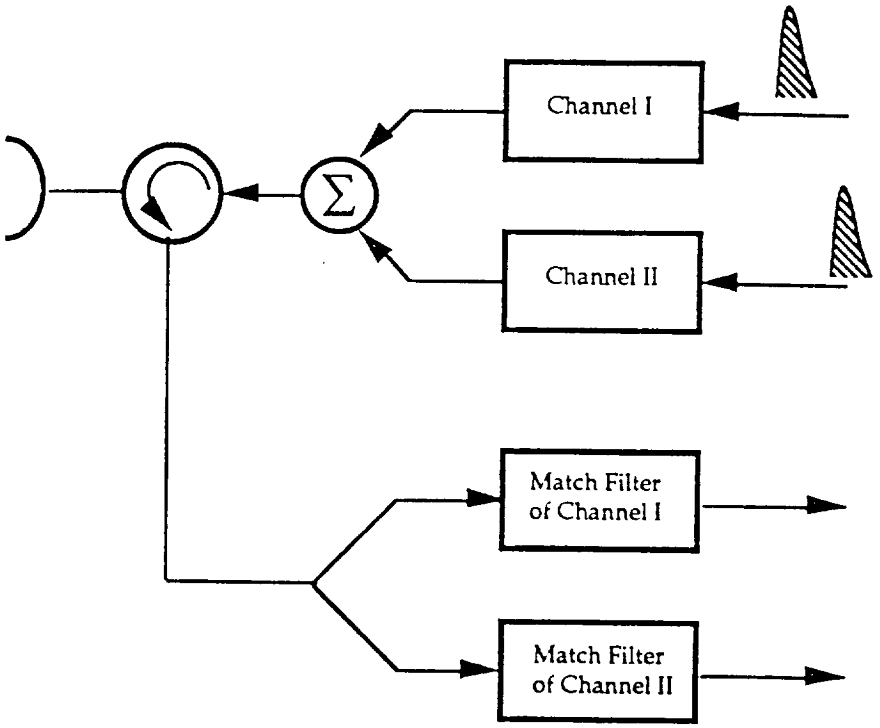

Figure 3.5 RAWS receiver block diagram [Xin, 1990].

Since the receiver can distinguish between the first and second pulse of the pulse-pair, the unambiguous range increases from that given in (3.24) to:

$$R_u = \frac{cT}{2}. \tag{3.31}$$

However, if the receiver is unable to receive radar echoes during the transmission of the second pulse, the unambiguous range will decrease to:

$$R_u = \frac{cT_R}{2}. \tag{3.32}$$

Transmitting each pulse of the pulse-pair on either different frequencies or with a unique polarization may be used to allow the receiver to receive echoes during the transmission of the second pulse, thus extending the unambiguous range to (3.31). However, by changing frequencies, the phase difference, $\Delta\phi$, may be erroneous (depending on the amount of frequency change) since the phase reference will have changed from the first to second pulse based on (3.1). That is, if the values of R_i are only a function of the relative motion between the satellite and the cloud, (3.1) indicates, although the resultant phase will be random, successive resultant phases will only shift by the amount corresponding to the Doppler frequency (i.e., $\Delta\phi$ in Figure 3.2). However, if the frequency is allowed to change, the resulting voltage becomes

$$V = \sum_{i=0}^{N} V_i e^{j2k_f R_i} \qquad f = 1 \text{ and } 2, \qquad (3.33)$$

where $k_1 = 2\pi/\lambda_1$ is the wavenumber corresponding to the first transmitted frequency and $k_2 = 2\pi/\lambda_2$ for the second frequency. In this case the first pulse will correspond to the resultant phase based on k_1 while the second pulse will be dependent on k_2. The change in wavenumber will define a new random resultant phase for the second pulse that is not simply a function of the Doppler frequency and k_1, but also of the second frequency ($k_2 = 2\pi/\lambda_2$). Unless this phase relationship is measured, the Doppler frequency can not be extracted.

The unambiguous range is determined from the maximum cloud penetration requirement derived from the target volume coverage and antenna pointing angle given in Table 1.3. Since the unambiguous range is known, the value of T_R can be computed by solving equation (3.32) for T_R. This yields

$$T_R = \frac{2R_u}{c}, \qquad (3.34a)$$

or,

$$T_R = \frac{2h_c}{c\cos\theta}, \qquad (3.34b)$$

where h_c is the maximum cloud height, c is the speed of light, and θ is the nadir angle. From Table 1.3, we find $h_c = 20$ km, and for worst case, $\theta = 35°$. Thus,

$$T_R = 162.8\mu\,\text{sec}. \qquad (3.35)$$

The minimum value of T_S is determined by the amount of time required to switch between the pulses within the pulse-pair and the time associated with the pulsewidth (see Figure 3.4). A choice of 5 μsec is used in this analysis for the switch time. The pulsewidth is given in Table 1.3 as 20 μsec, resulting in

$$T_S = 20 + 5 = 25 \ \mu\text{sec}. \qquad (3.36)$$

The time between sample pairs, T, can be obtained from

$$\begin{aligned} T &= T_S + \tau + T_R \\ &= 25 + 20 + 162.8 = 207.8 \ \mu\text{sec}. \end{aligned} \qquad (3.37a)$$

Solving for the pulse repetition frequency (PRF),

$$\text{or,} \qquad \text{PRF} = 1/T \approx 4800 \text{ Hz} \qquad (3.37b)$$

One of the major advantages of the covariance estimator is that the unambiguous range is a function of T_R while the unambiguous velocity is a function of T_S. This allows for independent control of the range and velocity ambiguity limits.

With the value of T_S determined, the spectral width can be calculated using (3.30). At 94 GHz,

$$\sigma_S \leq 10.2 \ \text{msec}^{-1}. \qquad (3.38)$$

Data from severe storms show a median spectral width of 4 msec^{-1} and only 0.5% of measured widths are larger than 10 msec^{-1}. Figure 3.6 illustrates the cumulative probability of the total spectrum width [Doviak, 1984].

The maximum radial velocity can be computed using the Nyquist criterion (3.25) and (3.36). At 94 GHz,

$$V_{mr} \leq \pm 32.1 \ \text{msec}^{-1}. \qquad (3.39)$$

The maximum horizontal and vertical velocities are obtained by dividing V_{mr} by $\cos\theta$ and $\sin\theta$, respectively, and are shown in Table 3.1 for $\theta = 35°$.

Table 3.1 Summary of maximum velocity components.

Velocity Component	Maximum Velocity at 94 GHz
V_{mh}	± 39.2 msec^{-1}
V_{mv}	± 56.0 msec^{-1}

Figure 3.7 shows the cumulative probability of the wind velocity for three tornadic storms. As can be seen, only 5% of tornadic clouds have wind velocities that exceed those shown in Table 3.1.

Different values of T_S can be used when operating at a frequency other than 94 GHz. The above analysis used 94 GHz as worst case, and appears to provide adequate coverage of the Doppler spectral width, σ_S, and the maximum Doppler extent, V_m even in tornadic storms.

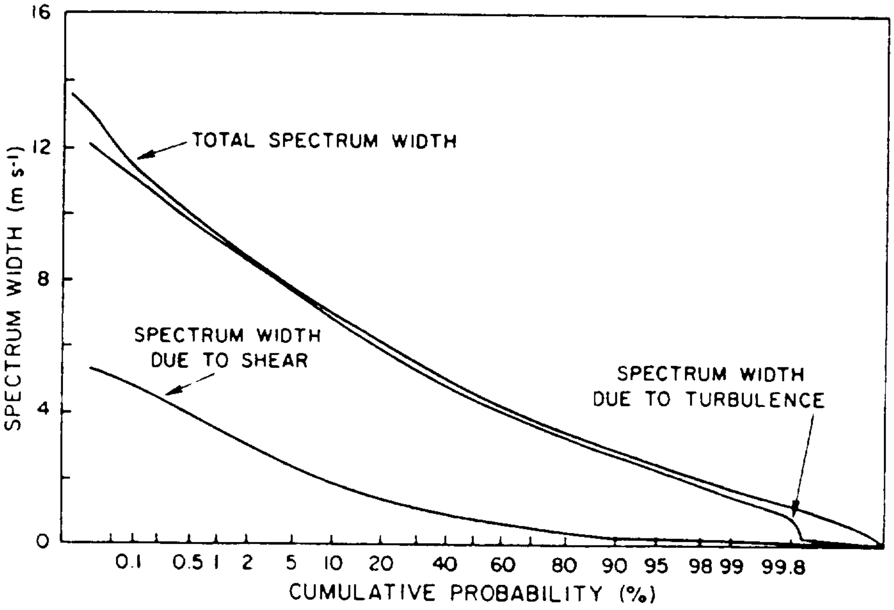

Figure 3.6 Cumulative probability of the total spectrum width and the width due to linear radial velocity shear and turbulence [Doviak, 1984].

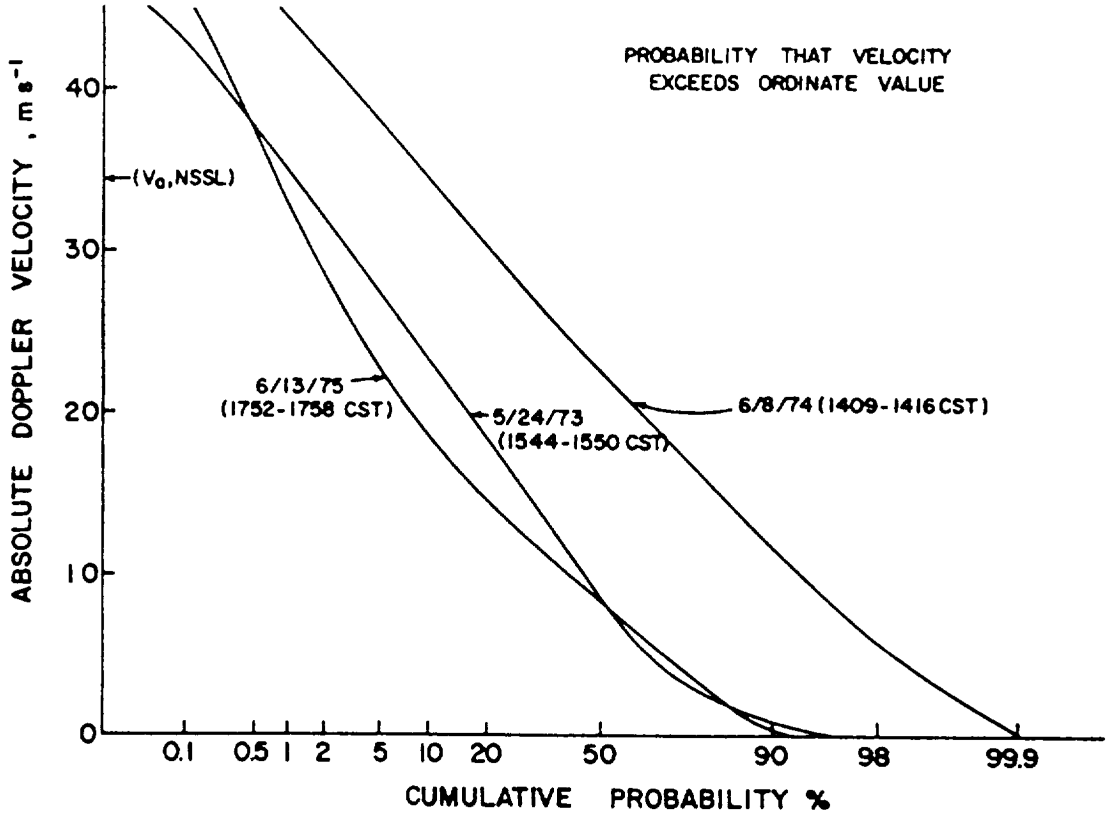

Figure 3.7 Cumulative probability of absolute Doppler velocities in three tornadic storms [Doviak, 1978].

CHAPTER 4

MEASUREMENT ERRORS AND ANTENNA SCAN PATTERN

4.1 BASIC EQUATIONS

The observed Doppler frequencies at three separate antenna positions produced by the wind vector

$$\bar{u}_w = u_{wx}\hat{x} + u_{wy}\hat{y} + u_{wz}\hat{z}, \qquad (4.1)$$

are given by the dot product

$$f_{di} = \frac{2\bar{u}_w}{\lambda} \cdot \bar{r}_i, \qquad i = 1, 2, 3 \qquad (4.2)$$

where λ is the wavelength, and $\bar{r}_i$ the antenna pointing vectors. The pointing vectors have the form

$$\bar{r}_i = \sin\theta_i \cos\phi_i \hat{x} + \sin\theta_i \sin\phi_i \hat{y} - \cos\theta_i \hat{z}, \qquad i = 1, 2, 3 \qquad (4.3)$$

with nadir angles θ_i, and azimuth angles ϕ_i as defined in Figure 4.1.

Note $\hat{x}, \hat{y}$, and $\hat{z}$ are unit vectors. In terms of Doppler velocities, (4.2) becomes

$$u_{di} = \bar{u}_w \cdot \bar{r}_i, \qquad i = 1, 2, 3 \qquad (4.4)$$

or in matrix form

$$\mathbf{u}_d = \mathbf{A}\mathbf{u}_w, \qquad (4.5)$$

where $\mathbf{u}_d$ is the measured velocity vector, $\mathbf{u}_w$ the wind vector, and **A** the matrix defining the antenna pointing geometry. Specifically;

$$\mathbf{u}_d = \begin{bmatrix} u_{d1} \\ u_{d2} \\ u_{d3} \end{bmatrix}, \qquad \mathbf{u}_w = \begin{bmatrix} u_{wx} \\ u_{wy} \\ u_{wz} \end{bmatrix},$$

$$\text{and} \quad \mathbf{A} = \begin{bmatrix} \sin\theta_1 \cos\phi_1 & \sin\theta_1 \sin\phi_1 & -\cos\theta_1 \\ \sin\theta_2 \cos\phi_2 & \sin\theta_2 \sin\phi_2 & -\cos\theta_2 \\ \sin\theta_3 \cos\phi_3 & \sin\theta_3 \sin\phi_3 & -\cos\theta_3 \end{bmatrix}. \tag{4.6}$$

Solving (4.5) for $\mathbf{u}_w$ allows the wind vector components to be determined from the measurements $\mathbf{u}_d$.

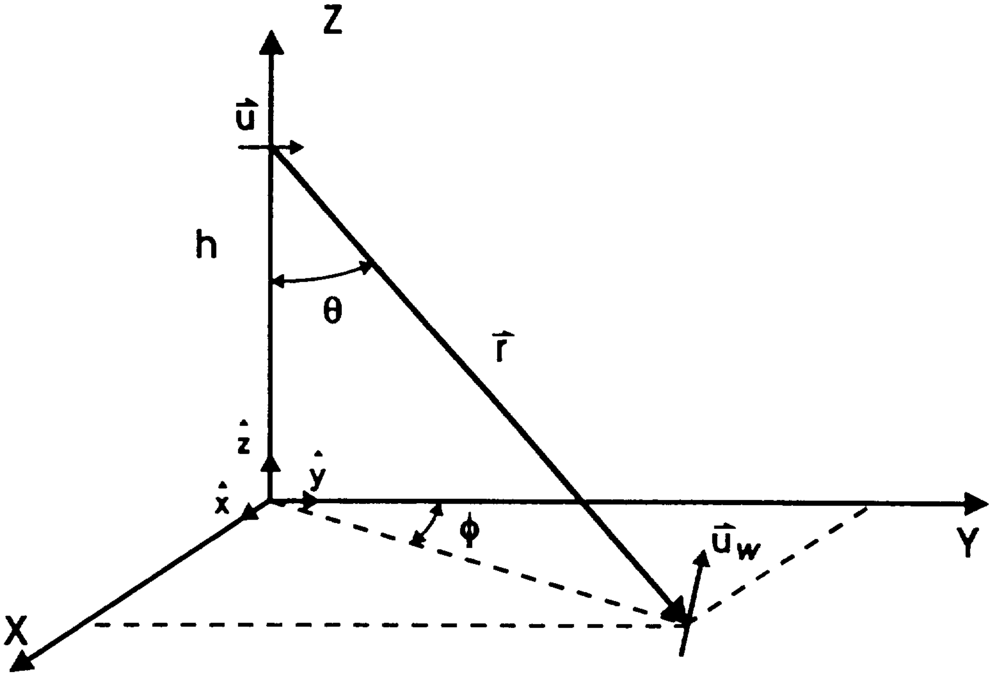

Figure 4.1 Antenna pointing vector coordinates.

4.2 MEASUREMENT ERRORS

There are three major sources of error in determining the wind speed: estimator errors in computing the mean-velocity, antenna pointing errors, and errors associated with tracking the mean-Doppler frequency caused by satellite motion. Only the estimator and antenna pointing errors will be analyzed in this thesis. These errors will be used in section 4.3 to examine the performance of several scan patterns.

4.2.1 VELOCITY UNCERTAINTY

The velocity uncertainty error is based on the ability of the covariance estimator to estimate accurately the mean velocity of the return weather echoes. Introducing a velocity uncertainty error, $\Delta\mathbf{u}_{de}$, into (4.5) yields:

$$\mathbf{u}_d + \Delta\mathbf{u}_{de} = \mathbf{A}\left(\mathbf{u}_w + \Delta\mathbf{u}_{we}\right),$$

which implies,

$$\Delta\mathbf{u}_{we} = \mathbf{A}^{-1}\Delta\mathbf{u}_{de}, \tag{4.7}$$

where $\Delta\mathbf{u}_{we}$ is the resulting wind error. Equation (4.7) is valid only if the matrix $\mathbf{A}$ is non-singular (i.e., $|\mathbf{A}| \neq 0$ and $\mathbf{A}^{-1} \neq \infty$).

For the antenna scan pattern analysis, the velocity uncertainty $\Delta\mathbf{u}_{de}$ is defined as the measurement accuracy for the covariance estimator given by (3.23). Using (3.23) with the waveform parameters defined in chapter 3, several standard deviation ($\sigma_{\mathrm{cov}} = \sqrt{\mathrm{var}(\hat{v})}$) versus spectral width plots were generated as a function of the SNR. Figures 4.2 (a), (b), and (c) illustrate these plots for various values of M at 94 GHz with T_S=25 μsec and T = 210 μsec, and Figure 4.3 for M = 1024 at 24 GHz with T_S=50 μsec and T = 250 μsec. Studying Figures 4.2 (a), (b) and (c) one is able to verify that the standard deviation decreased as $\frac{1}{\sqrt{M}}$ given by (3.19). The maximum spectral width used is 10 ms^{-1} as defined by (3.38).

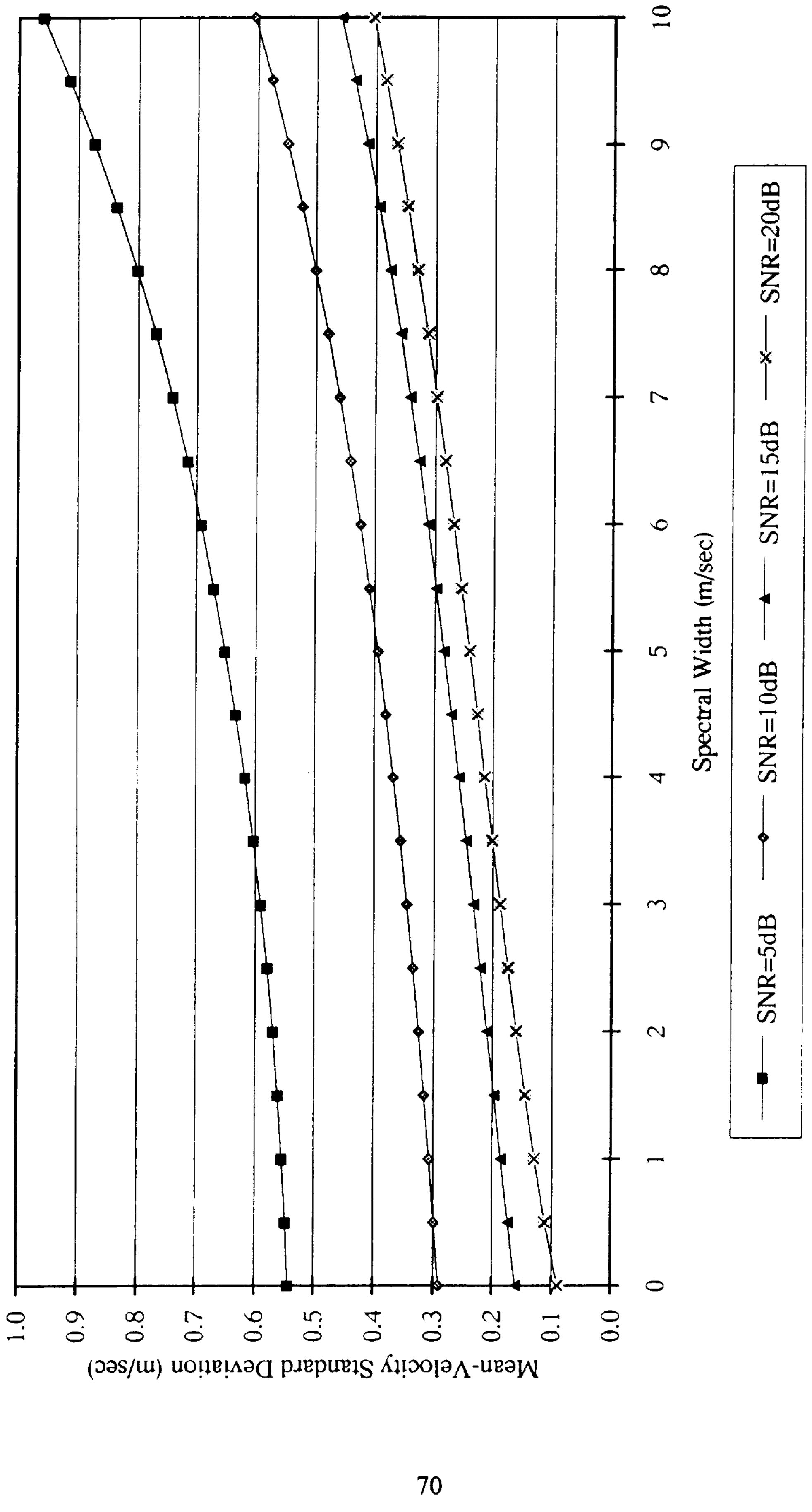

Figure 4.2(a) Standard deviation of a covariance estimator at 94 GHz with *Ts*=25 μsec, *T* = 210 μsec, and *M*=128.

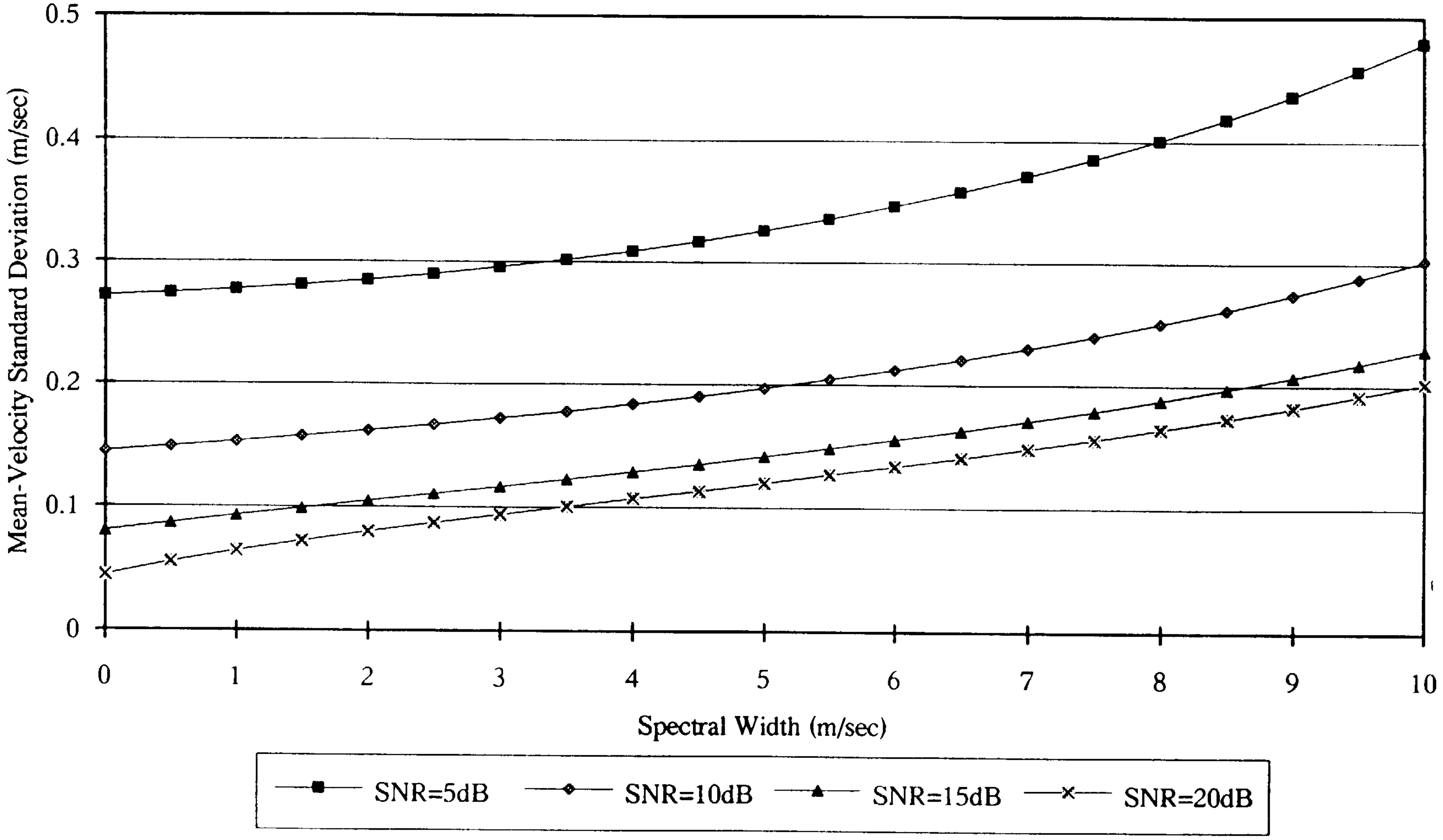

Figure 4.2(b) Standard deviation of a covariance estimator at 94 GHz with *Ts*=25 μsec, *T* = 210 μsec, and *M*=512.

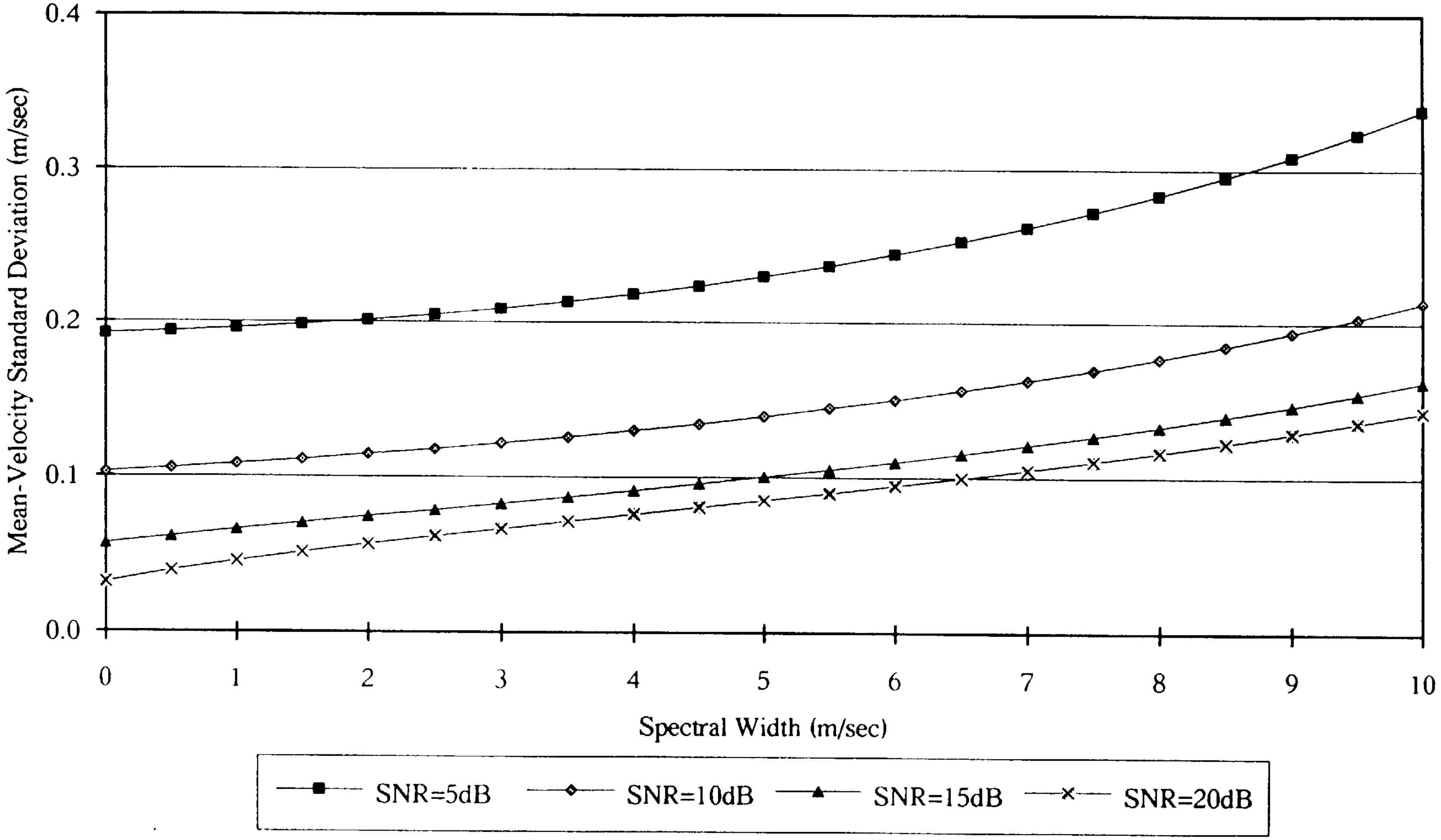

Figure 4.2(c) Standard deviation of a covariance estimator at 94 GHz with Ts=25 μsec, T = 210 μsec, and M=1024.

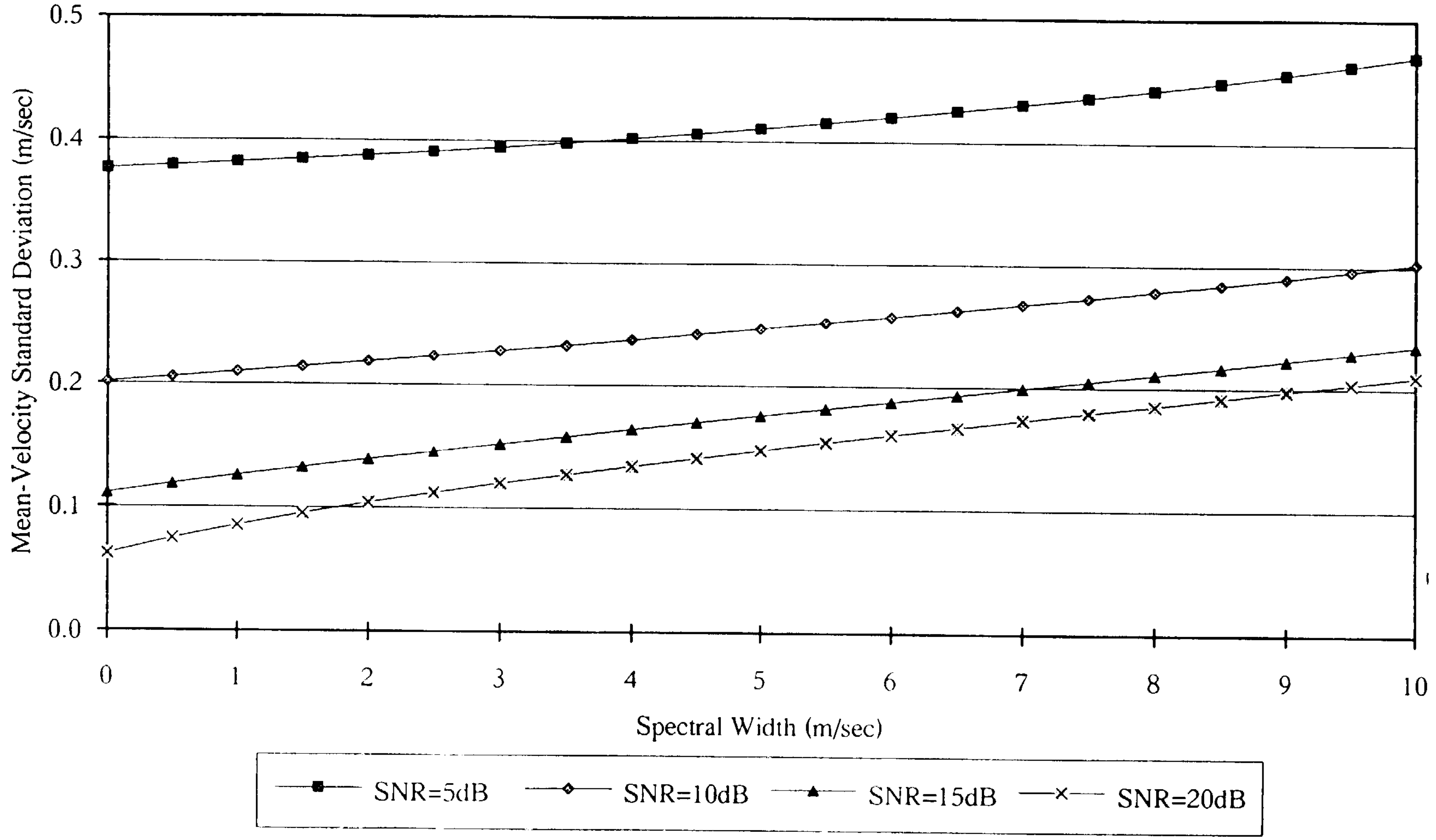

Figure 4.3 Standard deviation of a covariance estimator at 24 GHz with *Ts*=50 μsec, *T* = 250 μsec, and *M*=1024.

A value of $\Delta\mathbf{u}_{de} = 0.2\ \mathrm{ms}^{-1}$ is chosen for use in the scan pattern analysis. Both Figures 4.2 and 4.3 indicate that a 1024 pulse-pairs are required to achieve such a standard deviation. For water-clouds providing 10 dB SNR, Figure 4.2 justifies the use of 94 GHz to reach the $0.2\ \mathrm{ms}^{-1}$ limit, while for rain-clouds, 20 dB SNR is required at 24 GHz.

A Monte Carlo simulation program was written to model (4.7). A Gaussian probability density function with a standard deviation of σ_{cov} was used for values of $\Delta\mathbf{u}_{de}$. The elements of the **A** matrix are specific to the geometry of the particular scan pattern being analyzed. Results from this program appear in section 4.3.

4.2.2 ANTENNA POINTING ANGLE UNCERTAINTY

Some radar applications require the antenna to be adjusted during the time-on-target (TOT) to eliminate the effects of decorrelation. Decorrelation is caused by the illumination of different portions of the target, in this case a cloud, which produces a change in the phase reference during the signal processing period. To minimize the effects of decorrelation, the antenna beam is adjusted to maintain the same beam position on the cloud during the TOT. This antenna adjustment, however, produces velocity errors in that M **A** matrices will exist but only one will be used to determine $\mathbf{u}_w$ per (4.5).

For a covariance estimation based system, decorrelation is not a concern since, as discussed in section 3.2, each of the sample pairs is phase independent. However, if the scan rate and/or the radar's velocity is too great, the sample pairs used to compute the mean-velocity will originate from separate points on the cloud, thus measuring separate wind vectors and producing a velocity error. This implies the antenna must be adjusted to maintain the beam at a single point on the cloud. Since the maximum movement of the beam due to the satellites velocity is only 1.5 km at 0° azimuth (worst case), corrections to the nadir angle will be ignored. Unless a very slow scan rate is used, an azimuth squint angle will be required. An electronically scanned squint angle will be assumed in the azimuth direction only.

Referring to Figure 4.4 one sees that at time t = 1 the azimuth angle is ϕ_1 while at t = 2 this angle must change to ϕ_2, assuring a common beam position at position *P*.

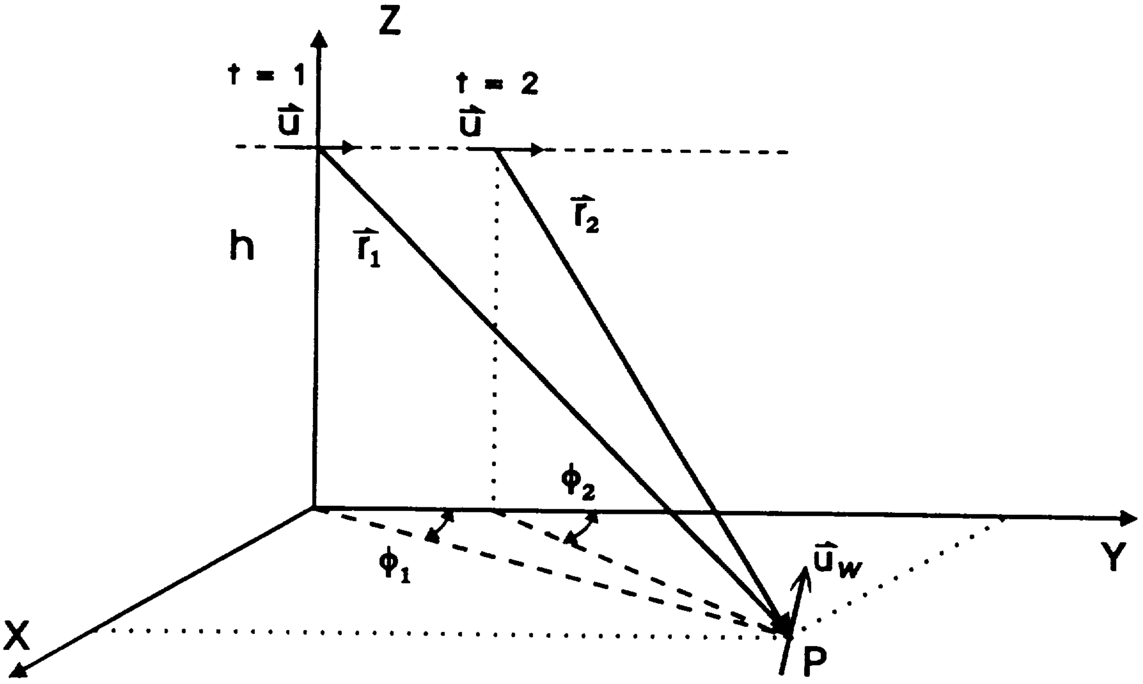

Figure 4.4 Antenna pointing error diagram.

To determine the error associated with these two measurements, the following equations are given

$$\begin{aligned}\mathbf{u}_{d1} &= \mathbf{A}_1\mathbf{u}_w \\ \mathbf{u}_{d2} &= \mathbf{A}_2\mathbf{u}_w\end{aligned} \tag{4.8}$$

The pointing error will occur since the wind vector will be determined from both sets of Doppler velocities (i.e., $\mathbf{u}_{d1}$ and $\mathbf{u}_{d2}$) but only one geometry matrix, $\mathbf{A}_1$, is used to determine $\mathbf{u}_w$ per (4.5). Thus the wind error will be

$$\begin{aligned}\mathbf{u}_{we} &= \mathbf{A}_1^{-1}\mathbf{u}_{d2} \\ \Delta\mathbf{u}_w &= \mathbf{u}_w - \mathbf{u}_{we} \\ \Delta\mathbf{u}_w &= \mathbf{u}_w - \mathbf{A}_1^{-1}\mathbf{A}_2\mathbf{u}_w\end{aligned} \tag{4.9}$$

where $\mathbf{u}_{we}$ is the wind vector generated by using the second velocity estimate, $\mathbf{u}_{d2}$, and the first geometry matrix $\mathbf{A}_1$. Subtraction of $\mathbf{u}_{we}$ from the wind vector results in the wind error $\Delta\mathbf{u}_w$. Note that (4.9) indicates that the wind error is a function of the wind vector $\mathbf{u}_w$.

A simulation program was written to determine $\Delta\mathbf{u}_w$ given the geometry of both antenna pointing vectors and a wind vector. Given the original geometry matrix $\mathbf{A}_1$, $\mathbf{A}_2$ can be obtained by determining ϕ_2 based on the satellite's velocity from the equation

$$\phi_2 = \sin^{-1}\left(\frac{R_1 \sin\phi_1}{R_1 - vt\cos\phi_1}\right) \tag{4.10}$$

where R_1 is the slant range of the first vector, v the satellite velocity, and t is the TOT. The program solves (4.9) by computing the maximum value of $\Delta\mathbf{u}_w$ for a complete set of wind vectors and given values of ϕ_1 and $|\mathbf{u}_w|$. The program then repeats this process for additional azimuth angles until all angles have been analyzed.

4.3 ANTENNA SCAN PATTERN

The antenna scan must allow for enough time-on-target to provide for an accurate mean-velocity measurement while allowing for multiple independent looks at the same cloud position. This section analyzes three antenna scan patterns to determine the pattern which produces the least measurement error.

4.3.1 CONICAL ANTENNA SCAN PATTERN

The conical scan originally proposed by Xin [Xin, 1990] is shown in Figure 4.5. This scan allows for four looks at given locations along a path parallel to the velocity vector and produces a "corkscrew" pattern on the ground (see Figure 4.9). Figure 4.6 illustrates these same four vectors relative to the satellite at four specific times and their ability to intersect at a point. To determine the wind velocity, measurements must be taken with at least three vectors intersecting the same point.

A set of equations given by (4.5) and (4.6) can be written based on the nadir and azimuth angles shown in Figure 4.5. Solving (4.5) for $\mathbf{u}_w$, however, one finds a singularity of the matrix **A** (i.e., the determinate of **A**, $|\mathbf{A}|$, = 0) for a flat earth. At the singularity, $\mathbf{A}^{-1} = \infty$ implying $\mathbf{u}_w$ cannot be determined. The cause of the singularity is obvious since in 3-dimensional space three or more co-planar vectors are linearly dependent. Likewise in 2-dimensional space, two or more co-linear vectors are linearly dependent. Figure 4.7 shows all four antenna position vectors as being co-planar.

Since the satellite must fly parallel to a given point on the cloud, the vectors to that point will always be co-planar! If we look at the more realistic case of a curved earth, one finds the singularity is eliminated, but the vectors are still close to being co-planar, resulting in a large velocity uncertainty error. That is, as the vectors approach becoming co-planar, $|\mathbf{A}| \rightarrow 0$ and $\mathbf{A}^{-1} \rightarrow \infty$.

To eliminate the singularity and decrease the velocity uncertainty error, another approach is necessary. Figure 4.8 shows the same scan pattern given in Figure 4.5 with the exception that the three vectors are not co-planar. Prudent selection of the offset values $\Delta X1$ and $\Delta X2$ will guarantee a non-singular **A** matrix.

The disadvantage of using the offsets is that the vectors no longer intersect the same point on the cloud. This is only critical if the wind vector is not homogeneous over the offset distance. Due to the two nadir angles used in the conical scan pattern,

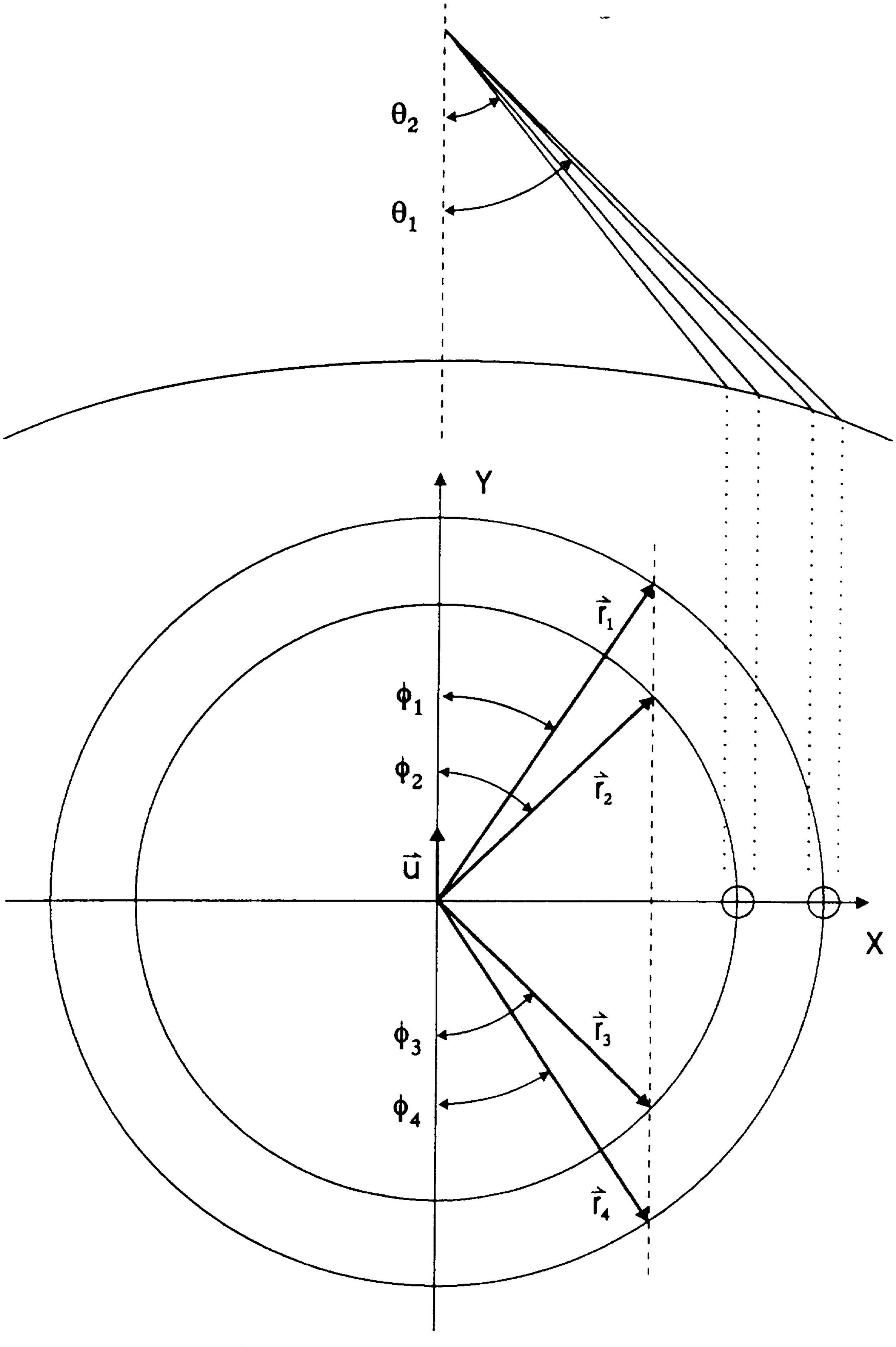

Figure 4.5 Originally proposed antenna scan.

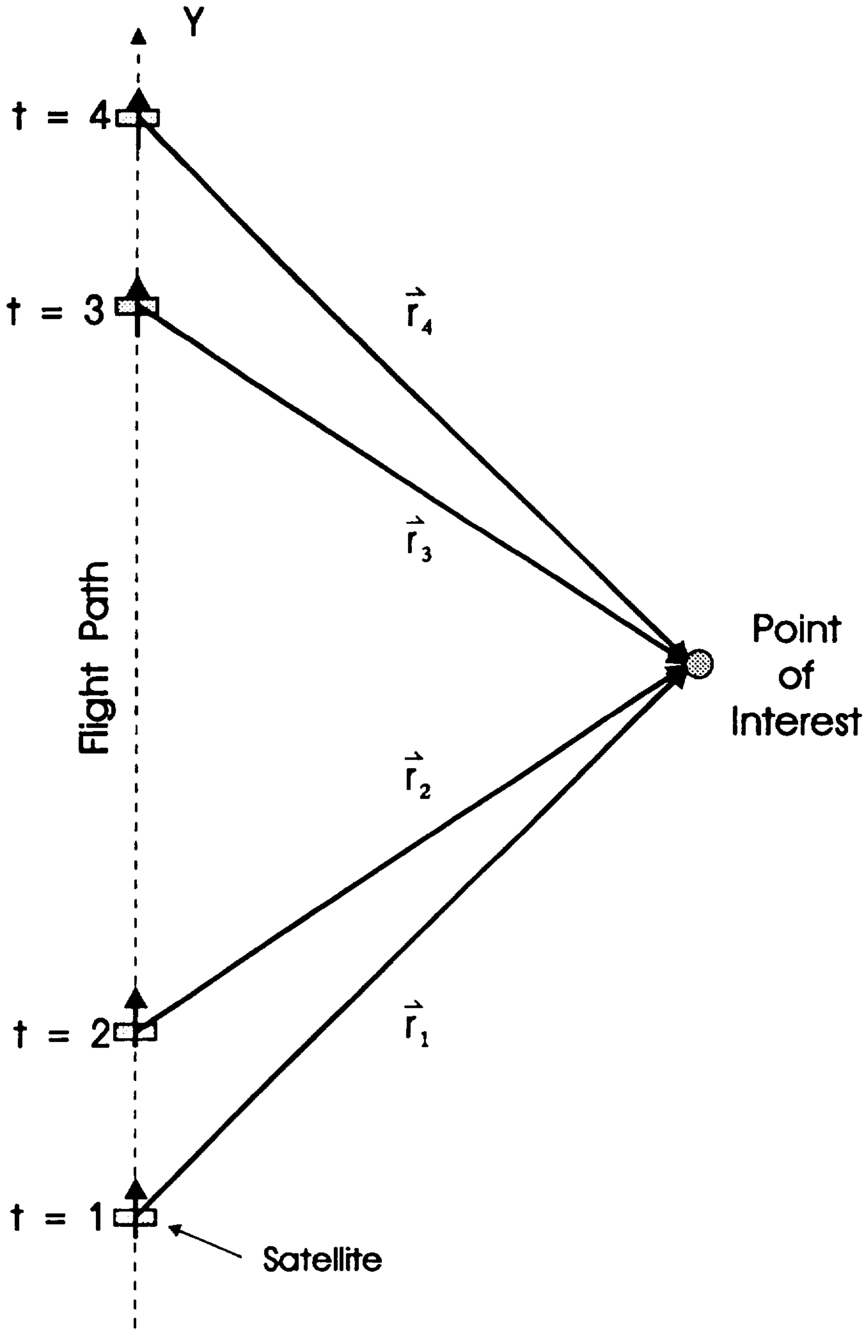

Figure 4.6 Antenna scan as seen by satellite.

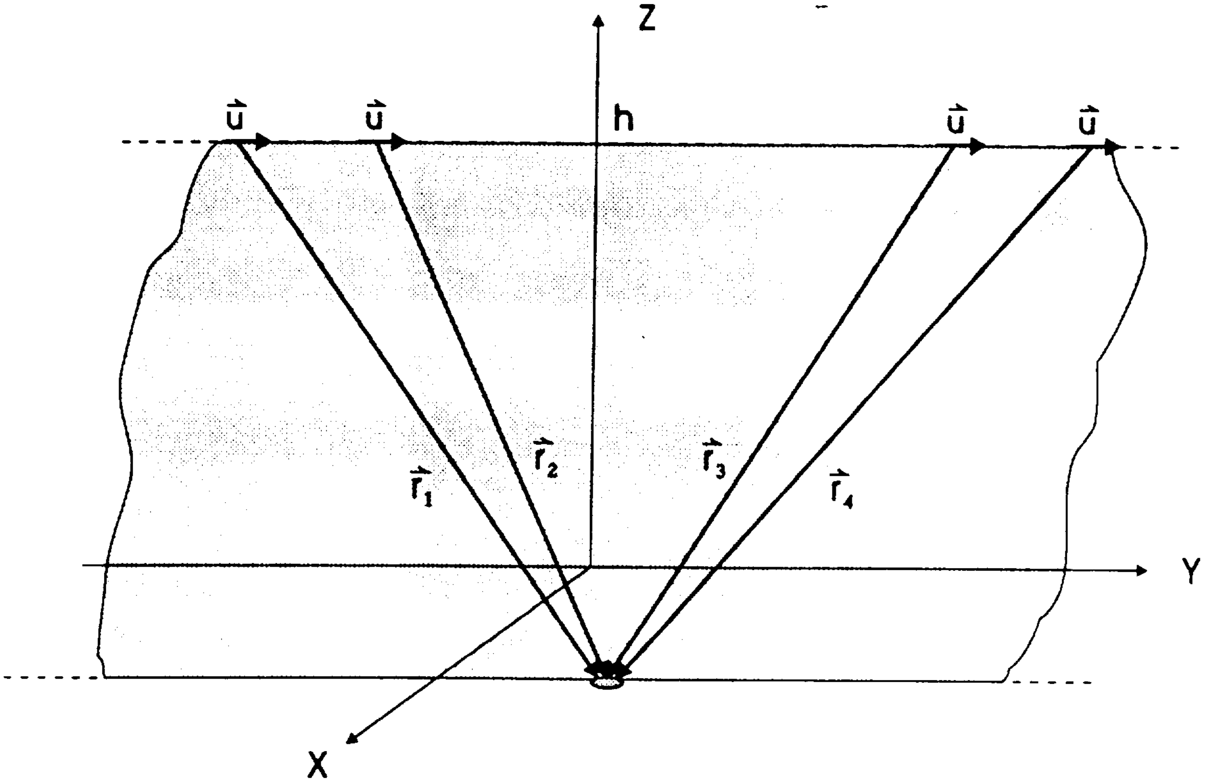

Figure 4.7 Illustration of co-planar vectors.

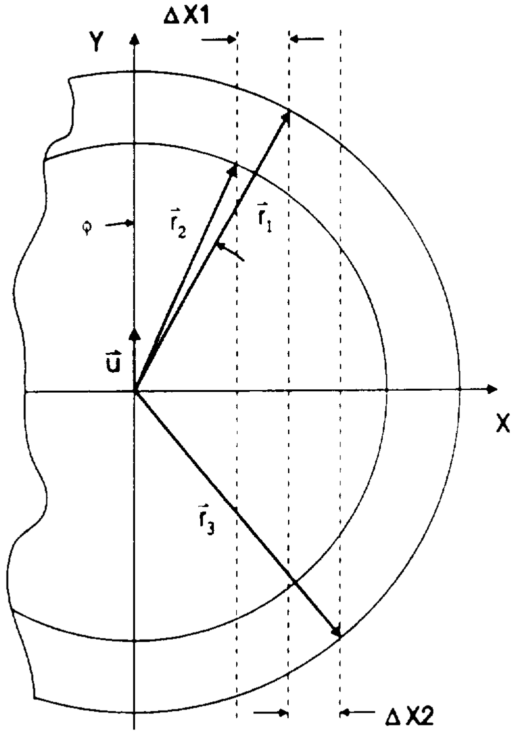

Figure 4.8 Modified conical scan pattern.

offsets will implicitly occur. The coordinates of the antenna beam's intersection with the ground (or cloud) are given by

$$\begin{aligned} x &= h \tan\theta_i \sin\omega t \\ y &= h \tan\theta_i \cos\omega t + vt \qquad i = 1, 2 \end{aligned} \qquad (4.11)$$

where h is the altitude of the satellite, θ_i is the antenna nadir angle, v is the spacecraft velocity, and ω is the angular antenna scan rate. Figure 4.9 illustrates the intersection pattern for an altitude of 525 km, a velocity of 7500 msec^{-1}, and a scan rate of 10 seconds. In some cases the offsets are as large as 10 km while in others they are less than 0.5 km. The amount of offset can be controlled, to some extent, by carefully selecting the scan rate.

The velocity uncertainty error (4.7) was computed using the Monte Carlo simulation program with $\Delta \mathbf{u}_{de} = 0.2\ \mathrm{ms}^{-1}$, and making 500 runs. The first computations varied both $\Delta X1$ and $\Delta X2$ from 0 to 100 km and obtained the maximum value of $|\Delta \mathbf{u}_{we}|$ between the azimuth angles 0° and 70°. The results are shown in Figure 4.10.

Note that the wind error is almost independent of $\Delta X2$. Due to this independence, another plot is made with $\Delta X2 = 0$ while varying $\Delta X1$ and the azimuth angle ϕ. This plot is given in Figure 4.11.

As can be seen in both Figures 4.10 and 4.11, the error is well above the design limit of 1 ms^{-1} for offset values < 10 km and only approaches the limit with offsets on the order of 100 km. This amount of offset is unacceptable since no rain cell will remain constant over such a large horizontal distance.

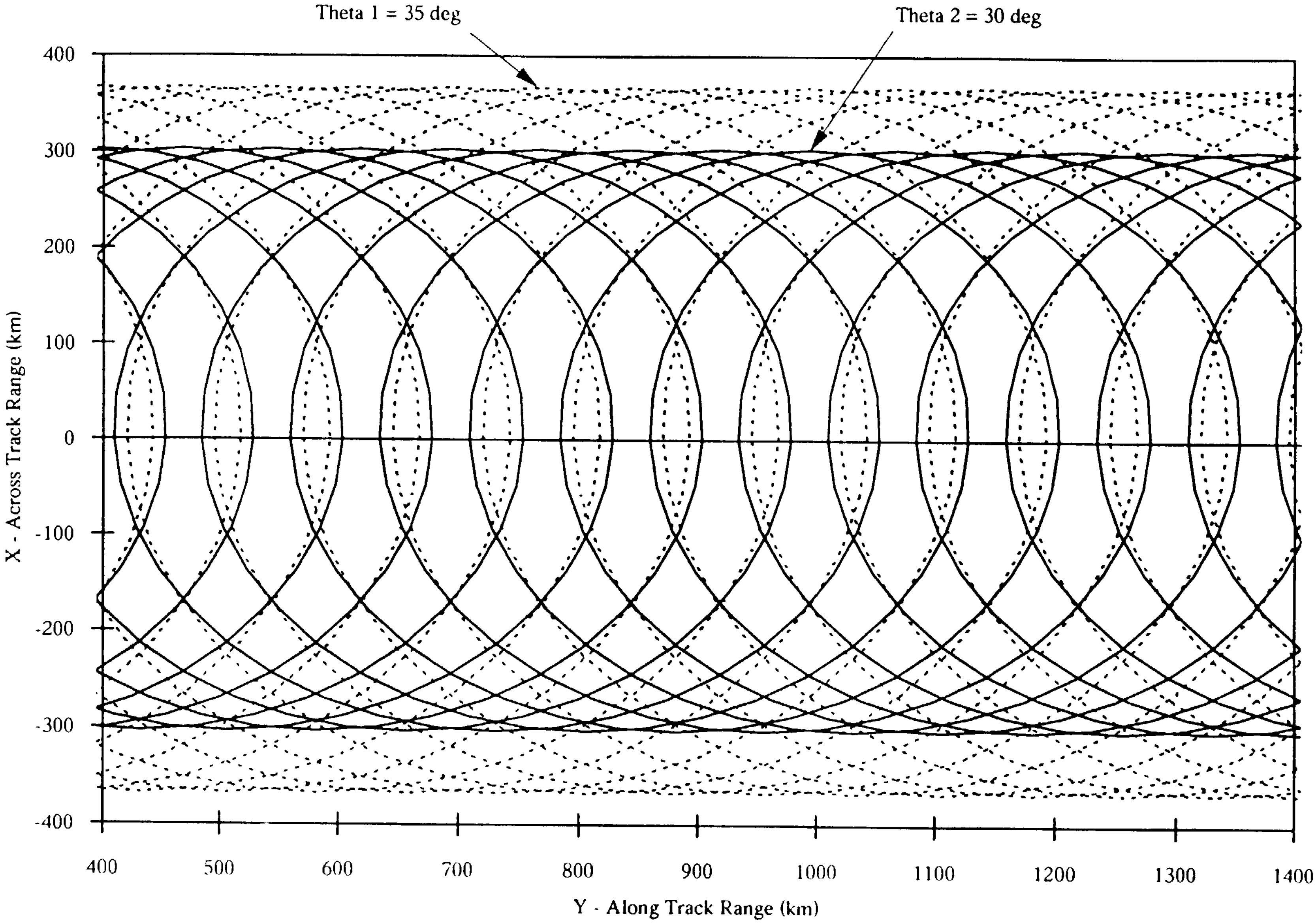

Figure 4.9 Intersection pattern with *h*=525 km, *v*=7500 msec^{-1}, and *w*=10 sec.

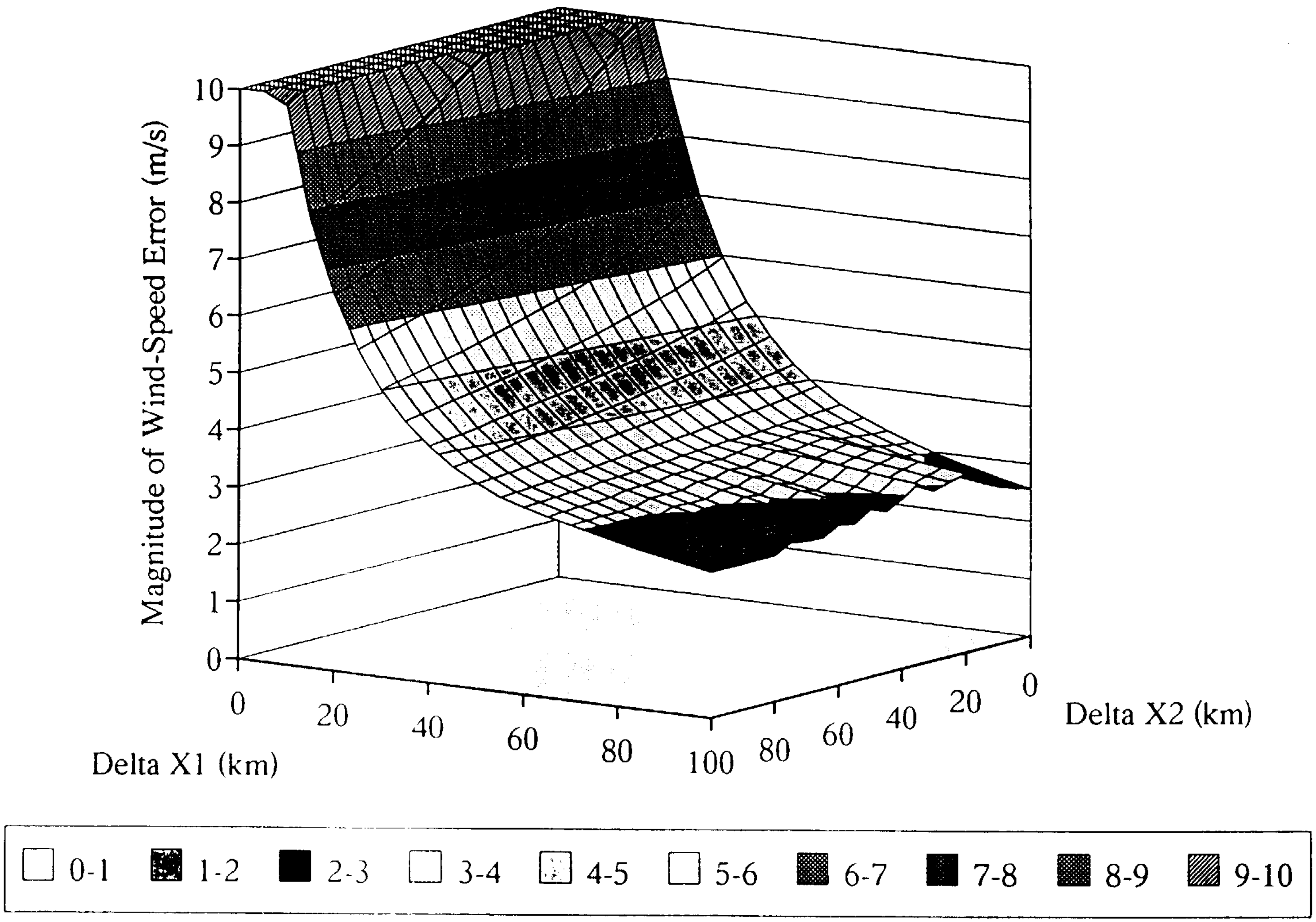

Figure 4.10 Magnitude wind-error versus ΔX1 and ΔX2 for the original scan pattern due to velocity uncertainty error.

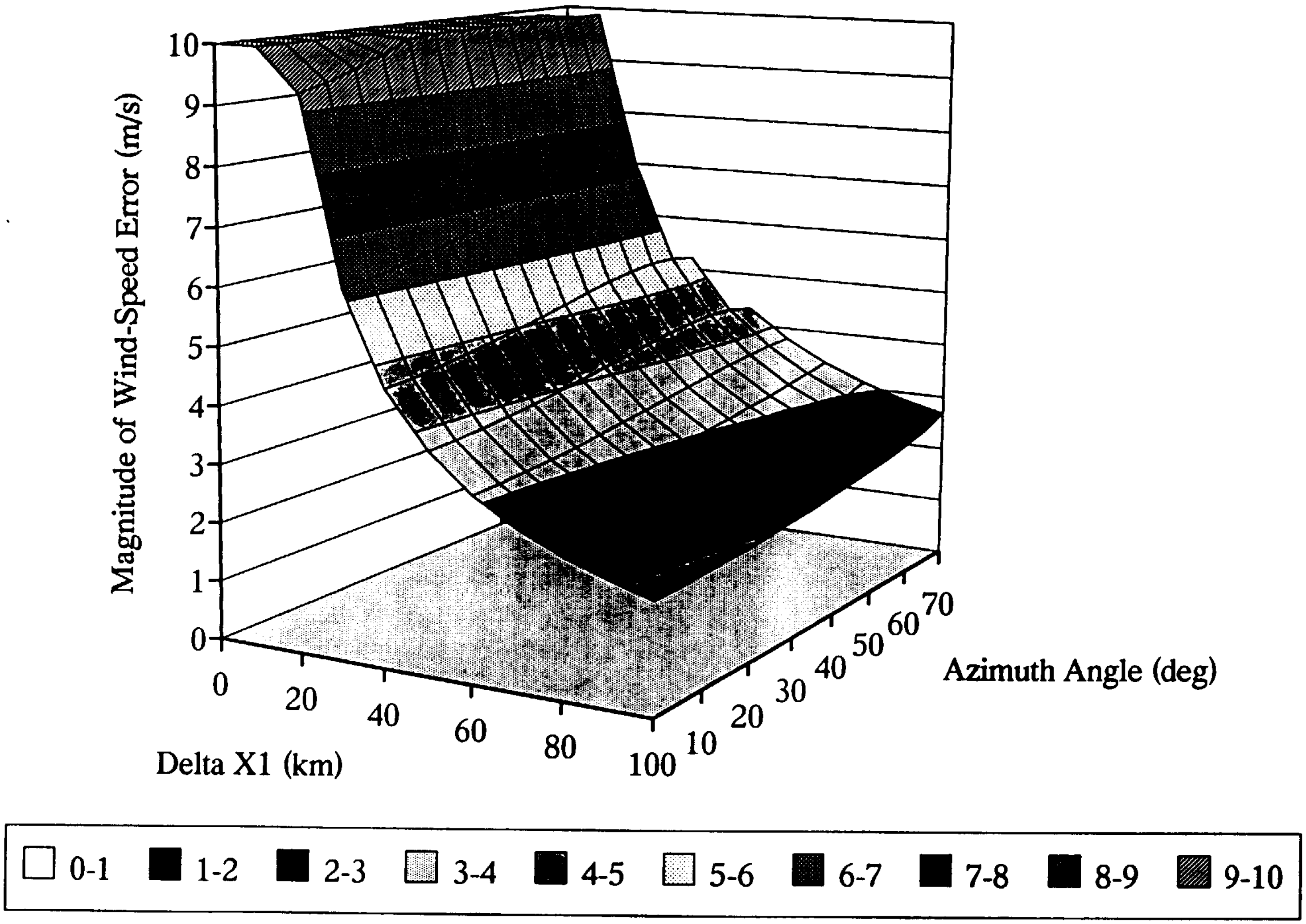

Figure 4.11 Magnitude wind-error versus $\Delta X1$ and azimuth angle for the original scan pattern due to velocity uncertainty error.

4.3.2 ALTERNATIVE THREE-VECTOR SCAN PATTERN

An alternate three-vector scan is shown in Figure 4.12. This pattern has the advantage of spacing the three vectors a maximum distance apart to provide better linear independence. However, it is more difficult to implement since a 2D electronically scanned antenna is required. The original scan pattern can be produced by a mechanically scanned antenna requiring less power and weight. The offsets ΔX1 and ΔX2 are still necessary to assure the three vectors are not co-planar.

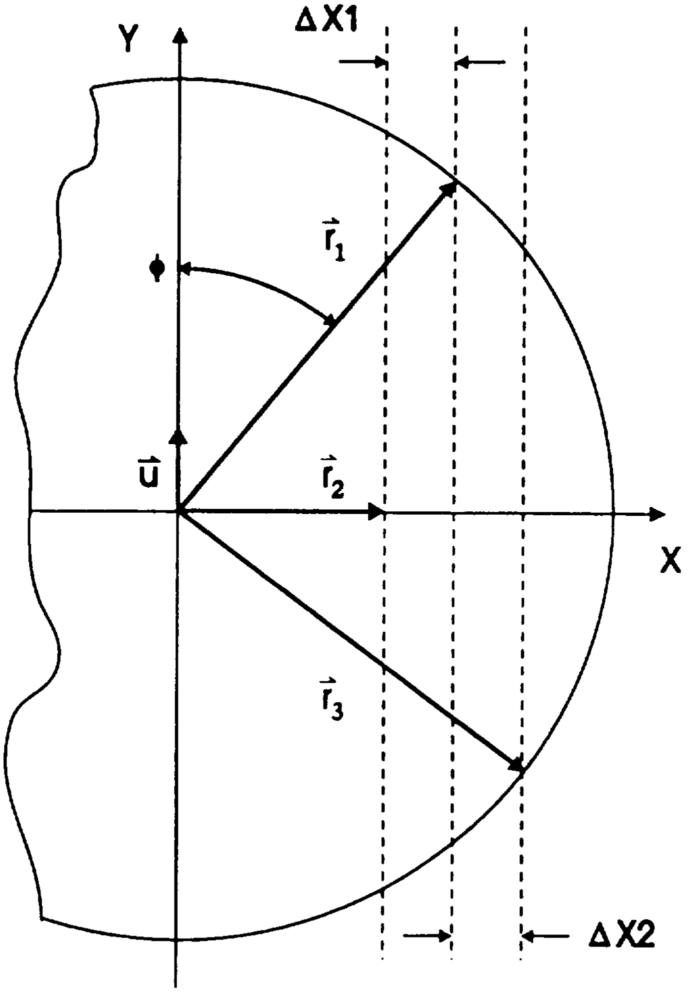

Figure 4.12 Alternate three-vector scan pattern.

a-2

The same velocity uncertainty error analysis done in the previous section is repeated here for the alternate three-vector scan. Figure 4.13 indicates the wind error for varying values of ΔX1 and ΔX2. The plot appears vary similar to Figure 4.10 although with less error, but still well above the 1 $m s^{-1}$ limit for small offsets.

Figure 4.14 illustrates the velocity uncertainty error generated with ΔX2 = 0 while varying ΔX1 and the azimuth angle. Again the wind-error is unacceptable.

For these two scan patterns, sufficient independence is not possible to obtain a reasonable wind error and still maintain a small measurement footprint.

4.3.3 TWO-VECTOR SCAN PATTERN

To compute only the horizontal components of the wind vector, Figure 4.15 illustrates a simple scan pattern that may be used. Since only one nadir angle is required, the antenna design would be simplified, however, the second nadir angle is still required to support de-aliasing techniques for ocean-wind scatterometery.

Although in this case the two vectors are co-planar, a singularity will only exist when the vectors are co-linear, occurring at azimuth angles 0° and 90°. Computing the velocity uncertainty for this scan pattern results in Figure 4.16

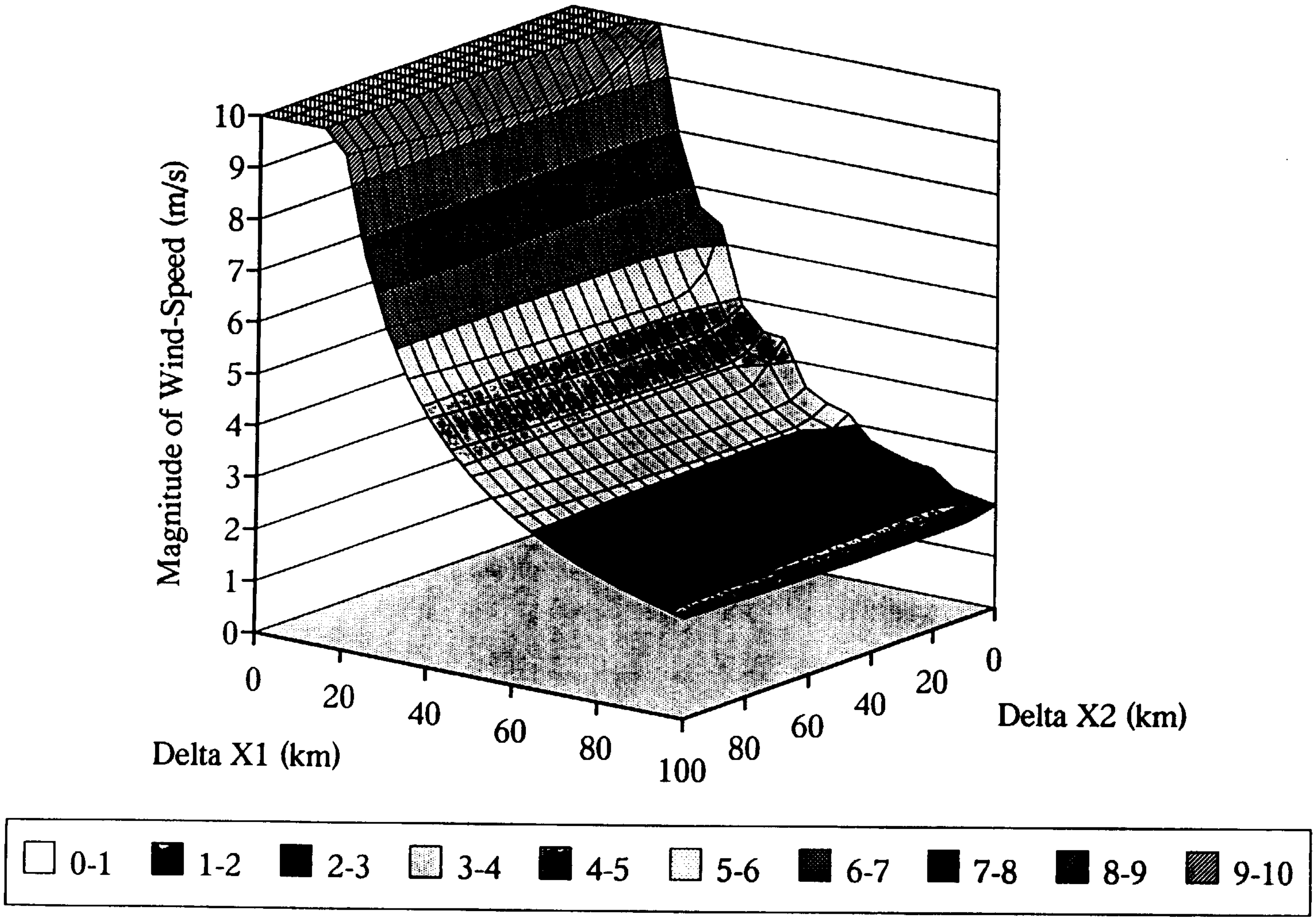

Figure 4.13 Magnitude wind-error versus ΔX1 and ΔX2 for alternate three-vector scan pattern due to velocity uncertainty error.

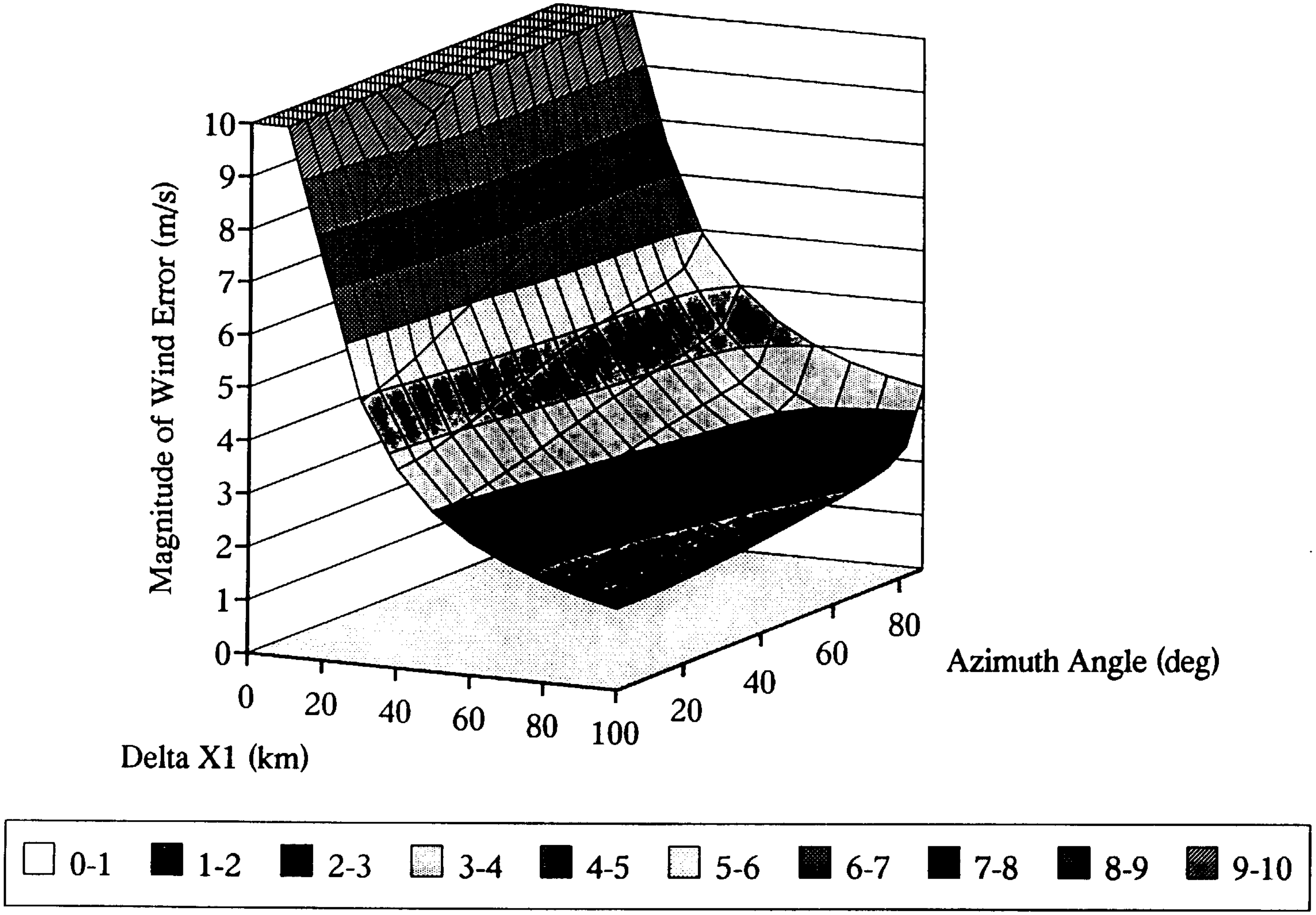

Figure 4.14 Magnitude wind error versus ΔX1 and azimuth angle for alternate three-vector scan pattern due to velocity uncertainty error.

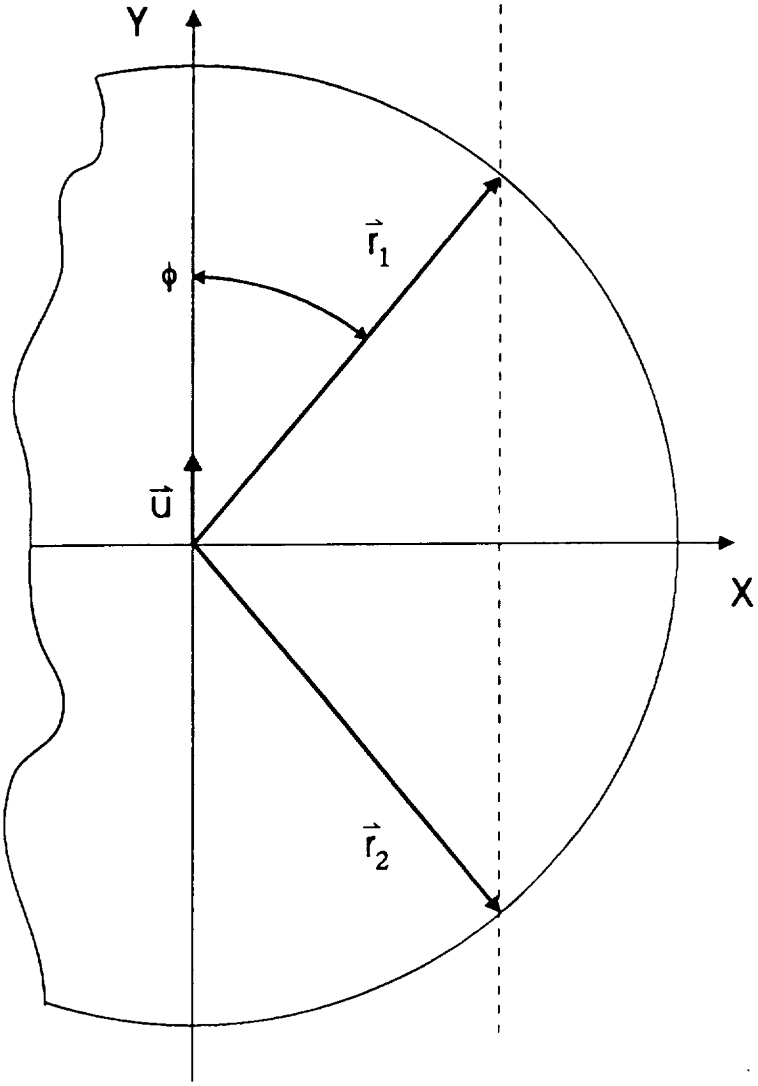

Figure 4.15 Two-vector antenna scan pattern.

Figure 4.16 indicates that the two-vector scan pattern will allow errors of less than 1 ms^{-1}. Next the simulation program used to calculate the antenna pointing error (4.9) is run. First the change in azimuth antenna angle must be determined using (4.10). For a PRF of 4800 Hz and 1024 pulse-pairs, the TOT will be 0.21 seconds. With the TOT and ϕ_2 calculated, the antenna pointing error is computed using (4.9) with the results shown in Figure 4.17. Figure 4.18 shows the total error defined as the summation of both the velocity uncertainty and antenna pointing errors.

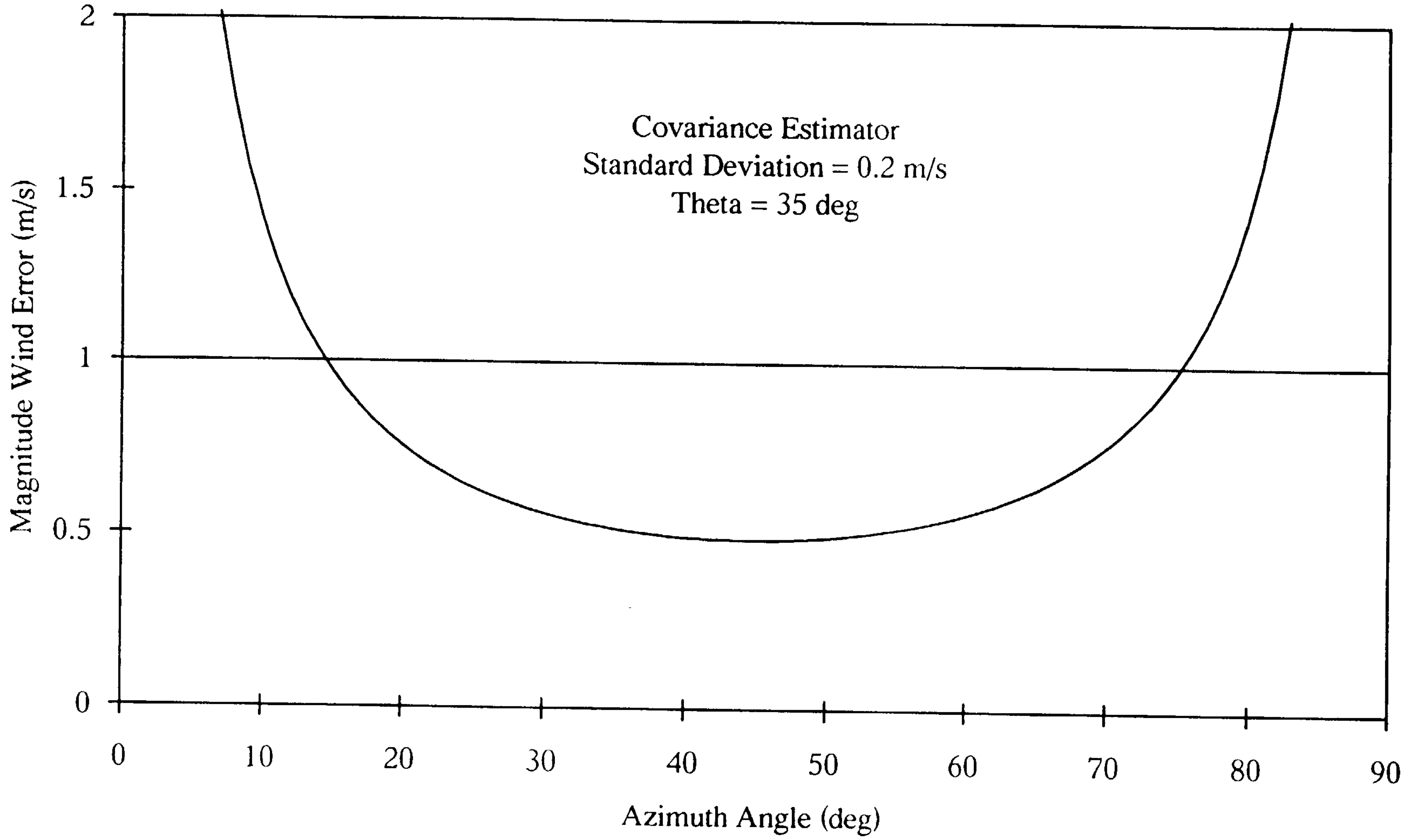

Figure 4.16 Magnitude wind-error versus azimuth angle for alternate two-vector scan pattern due to velocity uncertainty error.

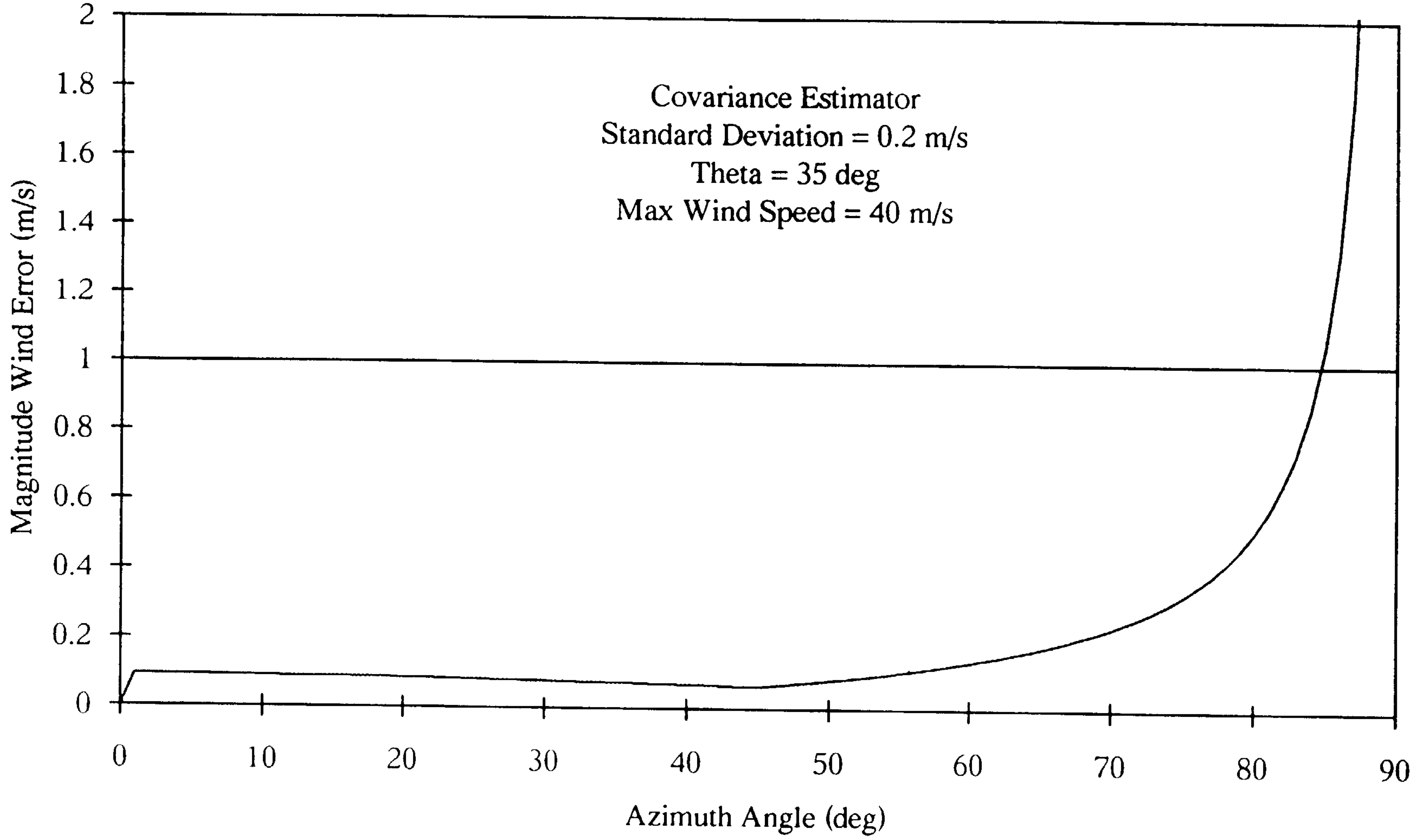

Figure 4.17 Magnitude wind-error versus azimuth angle for alternate two-vector scan pattern due to the antenna pointing uncertainty error.

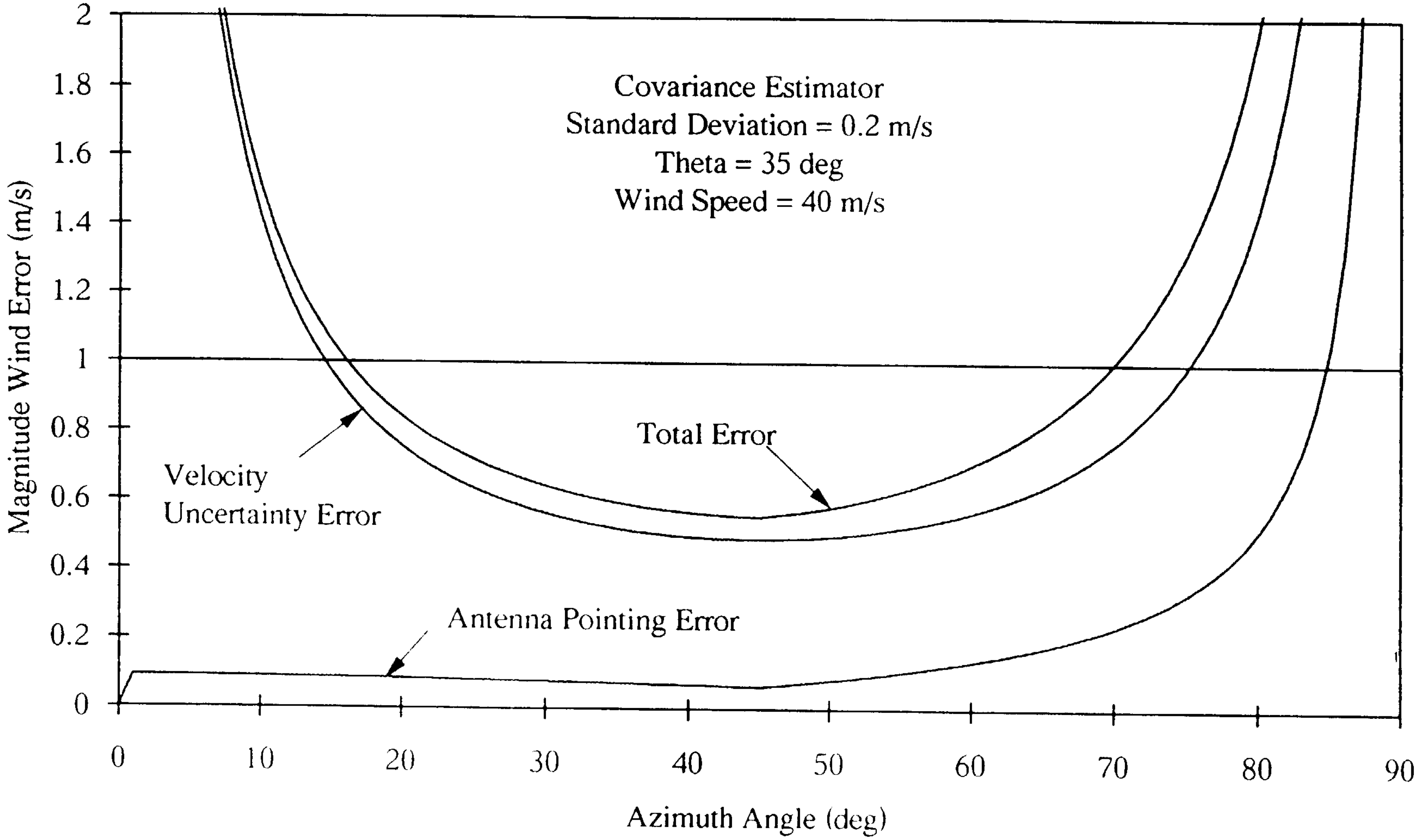

Figure 4.18 Total error for two-vector scan pattern.

Figure 4.18 indicates that the two-vector scan pattern results in acceptable wind error between the azimuth angles of 16° to 70°. This results in a swathwidth on each side of the satellites path equal to 249.26 km as shown in Figure 4.19. Thus the total swath width is 2*249.26 = 498.52 km.

The disadvantage of this pattern is that any vertical component of wind (e.g., rain) will present an error in the calculations of the horizontal wind components. This can be seen by reviewing the measurement process. The measurement of the wind components in the absence of a vertical component is

$$\begin{bmatrix} u_{d1} \\ u_{d2} \end{bmatrix} = \mathbf{A} \begin{bmatrix} u_{wx} \\ u_{wy} \end{bmatrix}$$

or

$$\begin{aligned} u_{d1} &= \sin\theta_1 \sin\phi_1 u_{wx} + \sin\theta_1 \cos\phi_1 u_{wy} \\ u_{d2} &= \sin\theta_2 \sin\phi_2 u_{wx} + \sin\theta_2 \cos\phi_2 u_{wy} \end{aligned} . \qquad (4.12)$$

If a vertical wind component does exist, the two measured velocities will equal

$$\begin{aligned} u_{d1} &= \sin\theta_1 \sin\phi_1 u_{wx} + \sin\theta_1 \cos\phi_1 u_{wy} - \cos\theta_1 u_{wz} \\ u_{d2} &= \sin\theta_2 \sin\phi_2 u_{wx} + \sin\theta_2 \cos\phi_2 u_{wy} - \cos\theta_2 u_{wz} \end{aligned} . \qquad (4.13)$$

Thus an error of $-\cos\theta_i u_{wz}$ is introduced in each of the velocity measurements. The amount of error caused by the vertical component u_{wz} is given in Figure 4.20. This figure indicates that the two-vector scan pattern is very sensitive to any vertical wind/rain component. The detection of a vertical component due to rain can be accomplished by use of a SNR threshold. As seen in chapter 2, rain will produce ample SNR (> 20 dB) which can be discriminated using a SNR threshold on a range-gate basis. The threshold detection of rain within a range gate only identifies those range gates which are susceptible to erroneous results. Thus another process is required to estimate the vertical component of the rain.

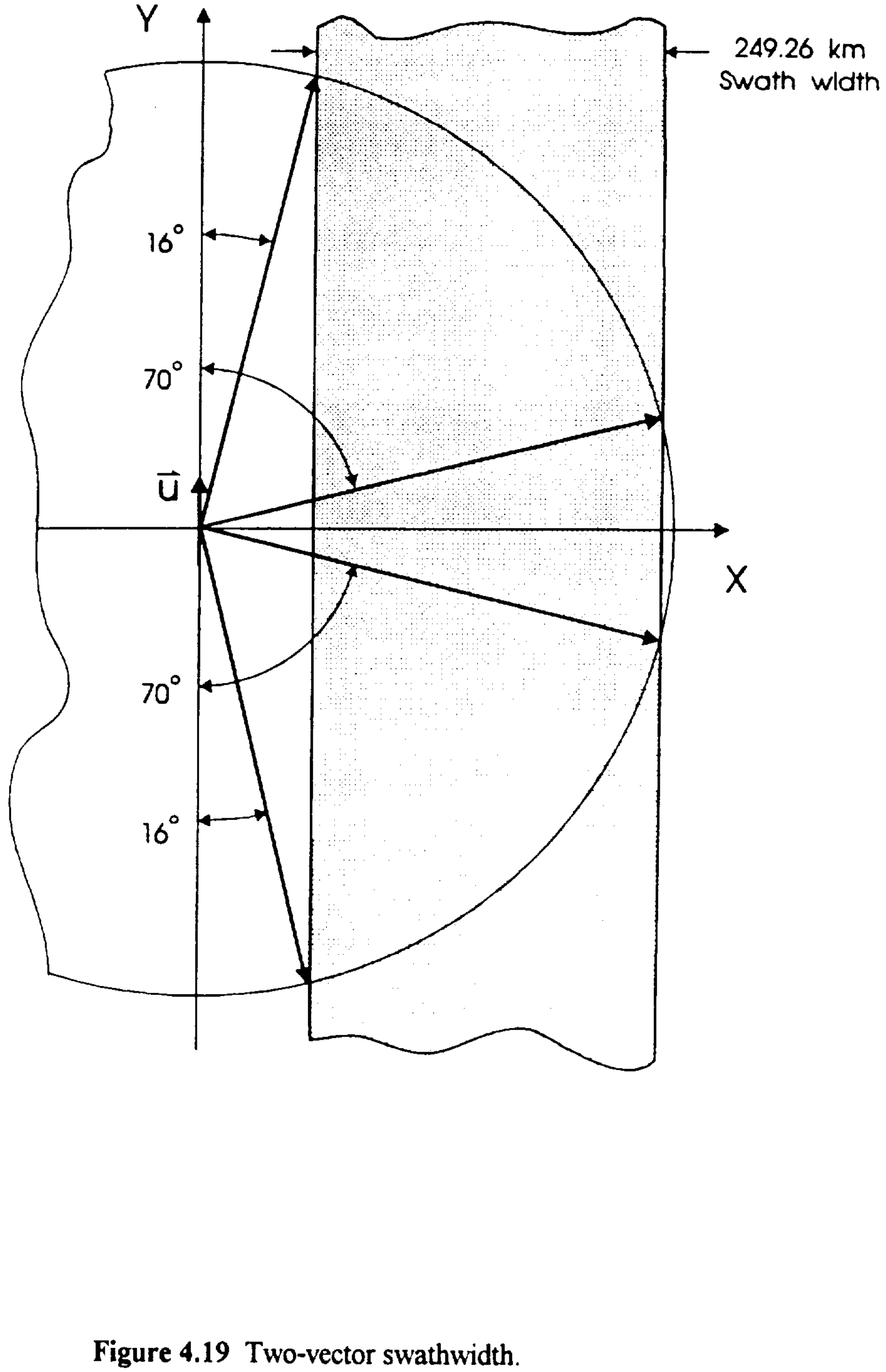

Figure 4.19 Two-vector swathwidth.

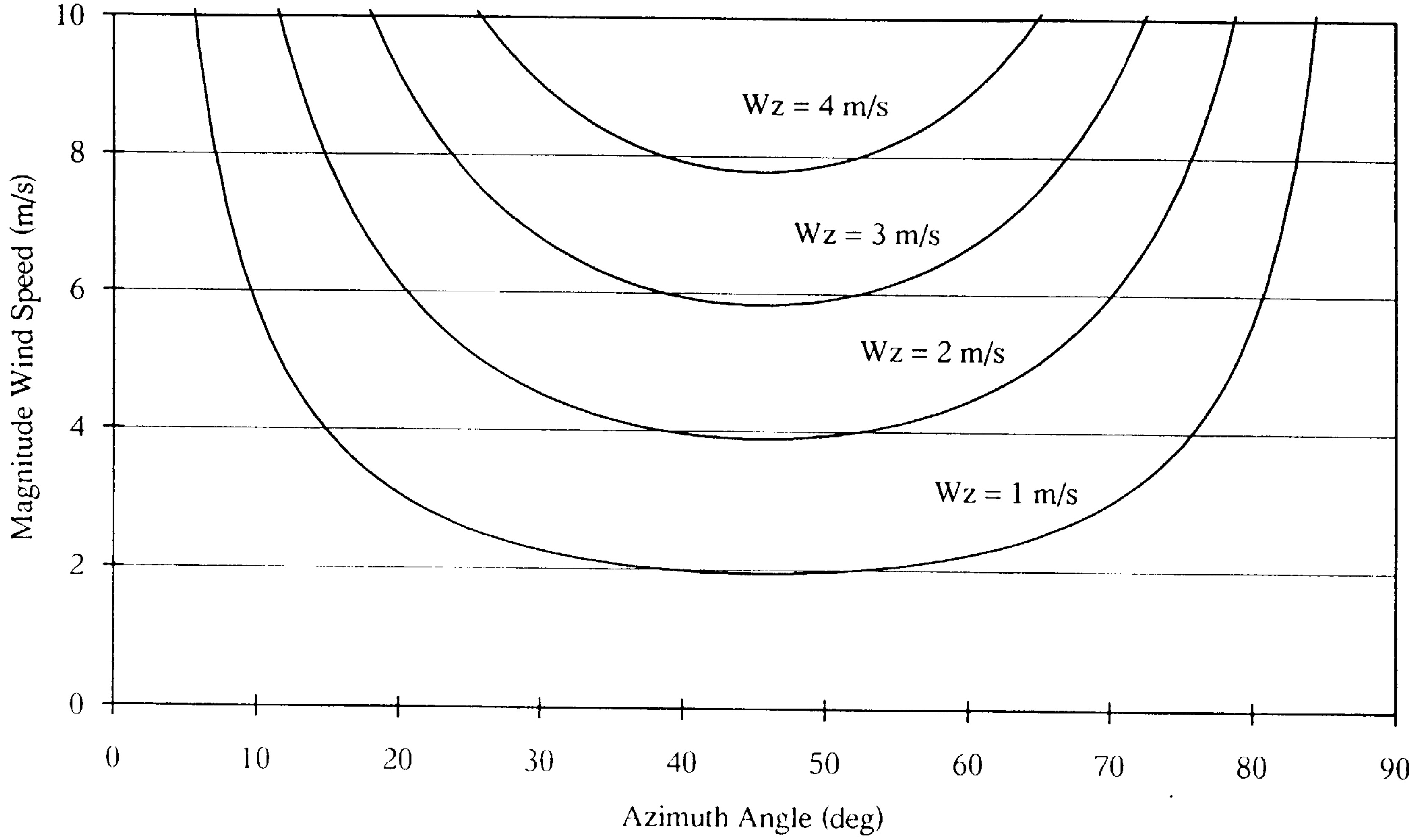

Figure 4.20 Error caused by vertical wind/rain component.

Several empirical relationships have been developed which relate the reflectivity factor Z, with the rain rate R. Work has been conducted by Gossard and others to obtain similar equations relating the ZR-relationships with the vertical rain velocity V_z. With the selection of a rain drop-size distribution, a ZRV_z model has been developed [Gossard, 1992]. Figure 4.21 illustrates the results of such a model.

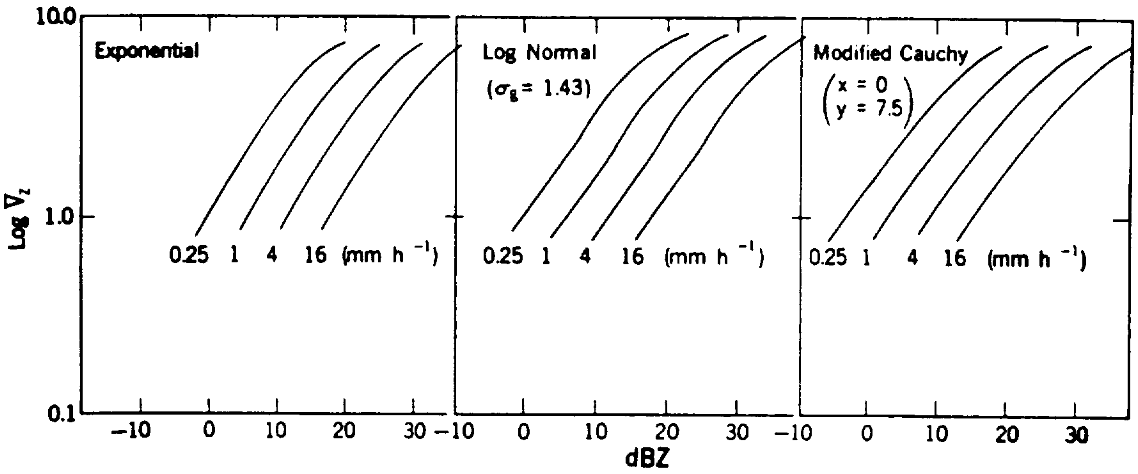

Figure 4.21 Theoretical ZRV_z. plots for log-normal distribution, modified Cauchy distribution, and exponential distribution [Gossard, 1992].

To determine the vertical component V_z, the radar must measure the reflectivity factor Z and use a ZR-relationship to determine the corresponding value of rain rate, R. The ZRV_z-relationship given in Figure 4.21 can then be used to determine the vertical wind/rain velocity, V_z. In practice, a look-up table can be employed to relate the correct value of vertical velocity V_z for a measured value of Z. Adding the values of $\cos\theta_i V_z$ to (4.13) results in an accurate computation of the horizontal wind components.

A full analysis of the accuracies of such models and their effect on the wind measurement error, will require for further study.

CHAPTER 5

NEW CANDIDATE SYSTEM

5.1 NEW CANDIDATE SYSTEM PARAMETERS

Many of the RAWS candidate system parameters given in Table 1.3 were modified here. Such changes include an altitude of 525 km introduced to remain compatible with the LAWS system, an increase of 3 dB in peak power to allow for a larger SNR, and new values for the transmit frequency and PRF derived from the analysis conducted in chapters 2 and 3. This chapter defines and calculates a new set of candidate system parameters as a result of these changes.

One important parameter required for most of the following calculations is the slant range to curved-earth. Values for this range can be obtained using the law of cosines which reduces to

$$R_i = (h + r_e)\cos\theta_i - \sqrt{(h+r_e)^2 \cos^2\theta_i - (h+r_e)^2 + r_e^2}\,, \qquad (5.1)$$

where h is the satellite's altitude, r_e the earth's radius, and θ_i the nadir angle. Using values of h = 525 km, r_e = 6370 km, θ_1 = 35° and θ_2 = 30°, (5.1) yields $R_1 = 654.42$ km and $R_2 = 614.79$ km.

5.1.1 RESOLUTION

The slant range resolution is given by

$$\Delta r = \frac{c\tau_c}{2}, \qquad (5.2)$$

where τ_c is the compressed pulsewidth and c is the speed of light. Since the compressed pulsewidth has not been modified, the value of τ_c taken from Table 1.3 may be substituted into (5.1), giving a slant range resolution of 150 m.

The horizontal resolution is simply given by

$$\Delta y_h = \beta_\phi R, \tag{5.3}$$

where β_ϕ is the azimuth beamwidth, and R the slant range to the radar footprint. Figure 5.1 illustrates the geometry involved in determining the vertical resolution.

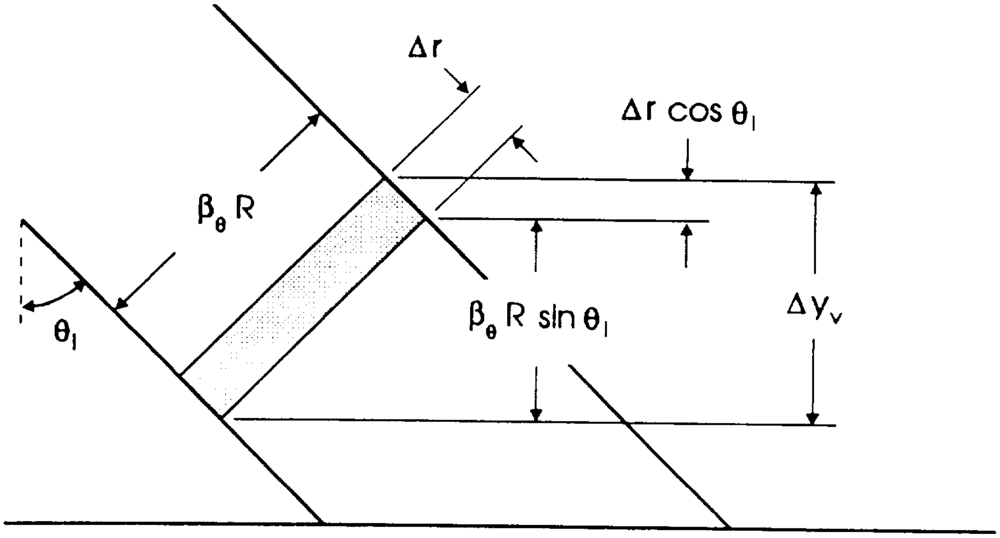

Figure 5.1 Vertical resolution geometry.

The vertical resolution is a function of the slant range resolution, the elevation beamwidth β_θ, and the slant range, and can be expressed as

$$\Delta y_v = \frac{c\tau_c}{2}\cos\theta_i + \beta_\theta R_i \sin\theta_i. \tag{5.4}$$

Table 5.1 lists the values computed for the vertical and horizontal resolutions with $h = 525$ km, θ_i and R_i obtained from (5.1), and the appropriate elevation and azimuth beamwidths at 94 and 24 GHz.

Table 5.1 Vertical and horizontal resolution.

Frequency	$\theta_1 = 35°$		$\theta_2 = 30°$	
	Δy_h	Δy_v	Δy_h	Δy_v
94 GHz ($\beta_\theta = \beta_\phi = 1.2$ mrad)	785.3 m	573.3 m	737.7 m	498.8 m
24 GHz ($\beta_\theta = \beta_\phi = 1.76$ mrad)	1151.8 m	783.5 m	1082.0 m	670.9 m

5.1.2 FOOTPRINT

The footprint is defined where the 3 dB beamwidth intersects the ground. Using the law of cosines and Figure 5.2, the along-track footprint, R_a, may be obtained from the following equations

$$\theta_u = \theta_i + \frac{\beta_\theta}{2},$$

$$\theta_l = \theta_i - \frac{\beta_\theta}{2},$$

$$R_u = (h+r_e)\cos\theta_u - \sqrt{(h+r_e)^2\cos^2\theta_u - (h+r_e)^2 + r_e{}^2},$$

$$R_l = (h+r_e)\cos\theta_l - \sqrt{(h+r_e)^2\cos^2\theta_l - (h+r_e)^2 + r_e{}^2},$$

$$R_a = \sqrt{R_u^2 + R_l^2 - 2R_uR_l\cos\beta_\theta}. \qquad (5.5)$$

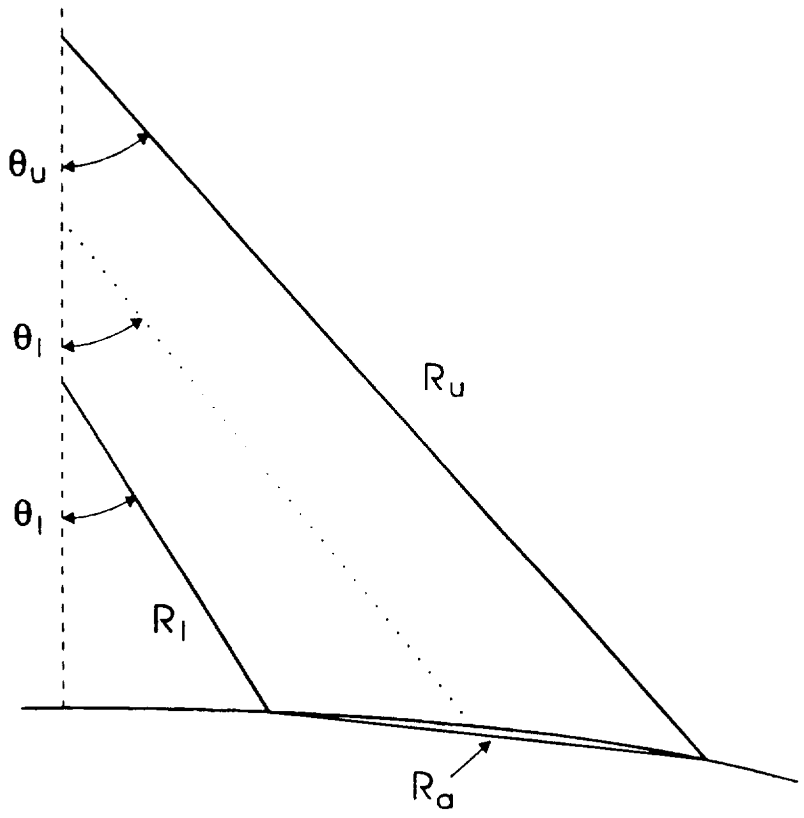

Figure 5.2 Radar footprint geometry.

The across-track footprint will equal the horizontal resolution, Δy_h, given in (5.3). Table 5.2 lists the values computed for the radar along-track footprint with $h = 525$ km and the appropriate elevation and azimuth beamwidths at 94 and 24 GHz

Table 5.2 Radar along-track footprint.

Frequency	$\theta_1 = 35°$	$\theta_2 = 30°$
94 GHz ($\beta_\theta = \beta_\phi = 1.2$ mrad)	1.0 km	0.877 km
24 GHz ($\beta_\theta = \beta_\phi = 1.76$ mrad)	1.47 km	1.29 km

5.1.3 SWATHWIDTH

The swathwidth is defined as twice the acceptable (i.e., satisfies the wind-error limit) cross-track extent on either side of the satellite. For the 2-vector antenna scan pattern shown in Figure 4.18, the swathwidth may be determined by

$$R_{sw} = 2R_1 \sin\theta_1 (\sin\phi_2 - \sin\phi_1) \qquad (5.6)$$

where R_1 and θ_1 are given in (5.1), and $\phi_1 = 16°$ and $\phi_2 = 70°$ are taken from section 4.3.3. This results in $R_{sw} = 498.52$ km.

5.1.4 AVERAGE POWER

The definition of the average power is

$$P_{\text{avg}} = \frac{1}{T}\int_0^{\tau_u} P_{\text{peak}}(t)dt \qquad (5.7)$$

where P_{peak} is the peak transmitted power, τ_u is the uncompressed pulsewidth, and T is the period of P_{peak}. For a pulse-train uniformly spaced at T_S intervals, the average power is simply

$$P_{\text{avg}} = \text{DC}\, P_{\text{peak}} = \tau_u\, \text{PRF}\, P_{\text{peak}}\,, \qquad (5.8)$$

where PRF = $1/T_S$, and DC is the duty cycle. When using a pulse-pair waveform, P_{avg} becomes twice that of (5.8) due to the additional pulse. Thus (5.8) becomes

$$P_{\text{avg}} = 2\, \text{DC}\, P_{\text{peak}} = 2\, \tau_u\, \text{PRF}\, P_{\text{peak}}, \qquad (5.9)$$

Table 5.3 lists the values computed for P_{avg} using (5.9) with τ_u = 20 μsec, and P_{peak} = 6000 W.

Table 5.3 Radar average power.

PRF	P_{avg}
4800 Hz @ 94 GHz	1152 W
4000 Hz @ 24 GHz	960 W

The use of solar panel technology may be deficient for such a large average power, and the use of a nuclear power source required.

5.2 NEW CANDIDATE PARAMETERS

The new candidate parameters are given in Table 5.4.

Table 5.4 New RAWS candidate system parameters.

Altitude	525 km
Target Volume Coverage	100 km x 100 km x 20 km
Look Angles (from vertical)	35° and 30°
Transmit Frequencies	94 GHz and 24 GHz
PRF	4800 Hz @ 94 GHz 4000 Hz @ 24 GHz
Pulse Width (Compressed)	1 μsec
Time-Bandwidth Product	20
Antenna Size	8 X 8 m
Scan Period	10 sec
Vertical Resolution	For $\theta = 35°$: 0.57 km @ 94 GHz 0.78 km @ 24 GHz For $\theta = 30°$: 0.50 km @ 94 GHz 0.67 km @ 24 GHz
Horizontal Resolution	For $\theta = 35°$: 0.79 km @ 94 GHz 1.15 km @ 24 GHz For $\theta = 30°$: 0.74 km @ 94 GHz 1.08 km @ 24 GHz

Table 5.4 New RAWS candidate system parameters (continued).

Slant Range Resolution	150 m
Footprint	For θ = 35°: 1.0 km × 0.79 km @ 94 GHz 1.47 km × 1.15 km @ 24 GHz For θ = 30°: 0.88 km × 0.74 km @ 94 GHz 1.29 km × 1.08 km @ 24 GHz
Swathwidth	498.52 km
Peak Power	6000 W
Average Power	1152 W @ PRF = 4800 Hz 960 W @ PRF = 4000 Hz
Receiver Noise Figure	4 dB
Transmitter Losses	1.5 dB
Receiver Losses	1.5 dB
Spacecraft Speed	7.5 km/s

CHAPTER 6

CONCLUSION

The major topics that were discussed are: the selection of an optimal frequency to obtain the maximum SNR, the design of a transmit waveform to provide sufficient unambiguous range and velocity, and the study of an antenna scan pattern capable of providing wind-error accuracies of < 1 msec^{-1}.

The comparison of the reflectivity factor comparison of the Deirmendjian model with the Diem and Squires data proved acceptable for the thinner clouds characterized by $D_O < 92$ μm and $m_V < 0.87$ gm^{-1}. The SNR for these thinner clouds limits the system sensitivity. Ample SNR (>10 dB) occurs at 94 GHz. The large-droplet cloud models, although not realistic in nature due to their excessive drop diameters, provide the maximum cloud attenuation. For such highly attenuating clouds, a lower frequency is required for penetrating to the lower rain layers. The ice clouds provide ample SNR for the higher frequencies due to their larger drop radii. Based on the SNR results, the use of 94 GHz for the thinner clouds and 24 GHz for the large-droplet clouds is recommended for the RAWS system. If only one frequency is to be used, 24 GHz provides the best overall results. A complete set of SNR versus altitude is given in Appendix A. No further work is required on the radar sensitivity analysis unless a more accurate model is discovered or additional data is obtained.

The ability of the chirp-modulated waveform, in conjunction with the covariance estimator, to eliminate range and Doppler ambiguities independently is a very desirable feature. This allows for an effective high sampling rate of the weather echo while still remaining unambiguous is range. The value of T_S was shown to correspond to the maximum unambiguous velocity and spectral width measurable, while T_R provides the limitation to the unambiguous range. Letting T_S equal 25 μsec allows spectral width as wide as 10.2 ms^{-1} to remain reasonably correlated and allows for a maximum unambiguous velocity of ±32.1 ms^{-1} at 94 GHz (the worst case). These values are adequate for even tornadic storms.

Computer programs were developed to compute the velocity uncertainty and antenna pointing uncertainty errors for various antenna scan patterns. Three scan patterns were analyzed to determine if they produce acceptable wind errors (i.e., $< 1\ \mathrm{ms}^{-1}$). Due to the geometry of the satellite with respect to a single location on a cloud, the matrix **A** becomes singular for three-vector scan patterns using flat-earth geometry and produces unacceptable measurement errors using curved-earth geometry. A two-vector scan pattern was shown to provide acceptable error, but lacks the ability to determine all three wind components. Furthermore, any vertical component (i.e., rain) will cause erroneous results in the computation of the horizontal wind components. To minimize the effects caused by the rain, an estimate of the vertical velocity of rain was discovered by using a ZRV relationship. Thus the horizontal components of the wind can be determined from the covariance estimator and the vertical component of the rain obtained from the measured reflectivity factor and the ZRV relationship. Further analysis is required to determine the accuracy of such ZRV models and their effects on the two-vector antenna scan pattern.

Finally, a new set of candidate parameters was developed. Definitions and the associated values are presented and a summary table provided.

APPENDIX A

Table A1 presents a tabulated comparison of the Rayleigh and Mie two-way extinction coefficients for all six frequencies and for each cloud layers.

Table A2 presents a tabulated comparison of the Rayleigh and Mie backscatter coefficients for all six frequencies and for each cloud layers.

Figures A1 - A17 illustrate the SNR versus altitude plots generated for the 17 Deirmendjian cloud models.

Figure A-1 Comparison of Rayleigh and Mie two-way extinction coefficients.

Cloud Type	Dmax (um)	94 GHz (dB/km) Ray	Mie	Δ	35 GHz (dB/km) Ray	Mie	Δ	24 GHz (dB/km) Ray	Mie	Δ	17 GHz (dB/km) Ray	Mie	Δ	14 GHz (dB/km) Ray	Mie	Δ	10 GHz (dB/km) Ray	Mie	Δ
1-A-1(i)	1000	-0.01	-0.02	0.01	0.00	0.00	0.00	0.00	0.00	0.00	0.00	0.00	0.00	0.00	0.00	0.00	0.00	0.00	0.00
1-M-1(i)	1000	-0.01	-0.02	0.01	0.00	0.00	0.00	0.00	0.00	0.00	0.00	0.00	0.00	0.00	0.00	0.00	0.00	0.00	0.00
1-T-1(i)	1000	-0.01	-0.02	0.01	0.00	0.00	0.00	0.00	0.00	0.00	0.00	0.00	0.00	0.00	0.00	0.00	0.00	0.00	0.00
10-1(w)	200	-1.53	-1.54	0.01	-0.33	-0.33	0.00	-0.17	-0.17	0.00	-0.08	-0.08	0.00	-0.06	-0.06	0.00	-0.03	-0.03	0.00
14-1(w)	200	-1.53	-1.53	0.00	-0.33	-0.33	0.00	-0.17	-0.17	0.00	-0.08	-0.08	0.00	-0.06	-0.06	0.00	-0.03	-0.03	0.00
20-1(w)	200	-2.19	-2.19	0.01	-0.38	-0.38	0.00	-0.18	-0.18	0.00	-0.09	-0.09	0.00	-0.06	-0.06	0.00	-0.03	-0.03	0.00
20-2(w)	200	-2.26	-2.26	0.01	-0.40	-0.40	0.00	-0.20	-0.20	0.00	-0.10	-0.10	0.00	-0.07	-0.07	0.00	-0.03	-0.03	0.00
21-1C(w)	200	-9.42	-9.52	0.10	-1.76	-1.77	0.01	-0.85	-0.86	0.00	-0.43	-0.43	0.00	-0.30	-0.30	0.00	-0.15	-0.15	0.00
21-1B(w)	200	-18.07	-18.28	0.20	-3.24	-3.25	0.02	-1.56	-1.57	0.01	-0.79	-0.79	0.00	-0.54	-0.54	0.00	-0.28	-0.28	0.00
21-1A(r)	400	-0.66	-9.17	8.51	-0.08	-1.53	1.45	-0.04	-0.73	0.69	-0.02	-0.37	0.35	-0.01	-0.25	0.24	0.00	-0.13	0.12
21-2D(w)	200	-9.42	-9.52	0.10	-1.76	-1.77	0.01	-0.85	-0.86	0.00	-0.43	-0.43	0.00	-0.30	-0.30	0.00	-0.15	-0.15	0.00
21-2C(w)	200	-18.07	-18.28	0.20	-3.24	-3.25	0.02	-1.56	-1.57	0.01	-0.79	-0.79	0.00	-0.54	-0.54	0.00	-0.28	-0.28	0.00
21-2B(w)	200	-8.69	-8.79	0.11	-1.51	-1.51	0.01	-0.72	-0.73	0.00	-0.37	-0.37	0.00	-0.25	-0.25	0.00	-0.13	-0.13	0.00
21-2A(r)	4000	-4.90	-5.91	1.01	-1.43	-1.63	0.21	-0.71	-0.76	0.05	-0.36	-0.36	0.00	-0.22	-0.22	0.01	-0.08	-0.09	0.01
21-3D(w)	200	-20.58	-20.73	0.15	-4.71	-4.72	0.01	-2.34	-2.35	0.00	-1.21	-1.21	0.00	-0.83	-0.83	0.00	-0.43	-0.43	0.00
21-3C(w)	200	-28.81	-29.09	0.28	-5.51	-5.53	0.02	-2.68	-2.69	0.01	-1.36	-1.37	0.00	-0.93	-0.93	0.00	-0.48	-0.48	0.00
21-3B(w)	200	-17.91	-18.12	0.20	-3.18	-3.20	0.02	-1.53	-1.54	0.01	-0.78	-0.78	0.00	-0.53	-0.53	0.00	-0.27	-0.27	0.00
21-3A(r)	4000	-16.17	-29.55	13.38	-7.73	-8.16	0.43	-3.88	-3.77	-0.11	-2.34	-1.79	-0.55	-1.61	-1.12	-0.49	-0.53	-0.44	-0.09
22-1(w)	200	-2.21	-2.23	0.03	-0.39	-0.39	0.00	-0.19	-0.19	0.00	-0.09	-0.09	0.00	-0.06	-0.06	0.00	-0.03	-0.03	0.00
22-2(w)	200	-2.31	-2.33	0.02	-0.42	-0.42	0.00	-0.20	-0.20	0.00	-0.10	-0.10	0.00	-0.07	-0.07	0.00	-0.04	-0.04	0.00
25-1C(w)	200	-4.88	-4.93	0.04	-0.96	-0.96	0.00	-0.47	-0.47	0.00	-0.24	-0.24	0.00	-0.16	-0.16	0.00	-0.08	-0.08	0.00
25-1B(w)	200	-9.42	-9.52	0.10	-1.76	-1.77	0.01	-0.85	-0.86	0.00	-0.43	-0.43	0.00	-0.30	-0.30	0.00	-0.15	-0.15	0.00
25-1A(w)	200	-4.52	-4.57	0.05	-0.81	-0.81	0.00	-0.39	-0.39	0.00	-0.20	-0.20	0.00	-0.13	-0.14	0.00	-0.07	-0.07	0.00
25-2C(w)	4000	-61.99	-45.17	-16.82	-5.01	-7.44	2.43	-2.19	-3.33	1.15	-1.06	-1.59	0.53	-0.71	-1.04	0.33	-0.36	-0.49	0.13
25-2B(w)	4000	-31.91	-22.86	-9.05	-2.13	-3.51	1.38	-0.90	-1.56	0.66	-0.43	-0.72	0.30	-0.28	-0.46	0.18	-0.14	-0.21	0.07
25-2A(r)	6000	-4.15	-1.71	-2.44	-1.13	-1.13	0.00	-0.56	-0.70	0.15	-0.27	-0.40	0.13	-0.17	-0.29	0.12	-0.06	-0.15	0.09
25-3C(w)	2000	-50.91	-60.28	9.37	-8.95	-10.31	1.36	-4.34	-4.89	0.55	-2.21	-2.45	0.24	-1.51	-1.65	0.14	-0.77	-0.83	0.06
25-3B(w)	3000	-63.87	-45.73	-18.14	-4.24	-7.01	2.78	-1.78	-3.11	1.33	-0.84	-1.44	0.60	-0.56	-0.92	0.36	-0.28	-0.41	0.13
25-3A(r)	6000	-13.70	-8.56	-5.15	-6.11	-5.66	-0.46	-3.06	-3.52	0.45	-1.80	-2.02	0.22	-1.22	-1.44	0.22	-0.41	-0.76	0.35

25-4E(w)	2000	-6.07	-7.57	1.50	-1.16	-1.31	0.15	-0.57	-0.63	0.06	-0.29	-0.32	0.03	-0.20	-0.21	0.02	-0.10	-0.11	0.01
25-4D(w)	2000	-12.02	-15.21	3.19	-2.13	-2.46	0.33	-1.03	-1.17	0.13	-0.53	-0.58	0.05	-0.36	-0.39	0.03	-0.18	-0.20	0.01
25-4C(w)	2000	-9.48	-12.16	2.68	-1.59	-1.86	0.28	-0.76	-0.87	0.11	-0.39	-0.43	0.05	-0.26	-0.29	0.03	-0.14	-0.15	0.01
25-4B(w)	1000	-4.83	-5.19	0.35	-0.90	-0.93	0.03	-0.44	-0.45	0.01	-0.22	-0.23	0.00	-0.15	-0.15	0.00	-0.08	-0.08	0.00
25-4A(w)	200	-2.79	-2.82	0.03	-0.51	-0.52	0.00	-0.25	-0.25	0.00	-0.13	-0.13	0.00	-0.09	-0.09	0.00	-0.04	-0.04	0.00
26-1F(i)	1000	-0.03	-0.04	0.01	0.00	-0.01	0.00	0.00	0.00	0.00	0.00	0.00	0.00	0.00	0.00	0.00	0.00	0.00	0.00
26-1E(w)	2000	-30.48	-34.55	4.07	-11.21	-11.85	0.63	-6.40	-6.64	0.25	-3.55	-3.65	0.10	-2.49	-2.56	0.06	-1.32	-1.35	0.03
26-1D(w)	2000	-47.81	-54.71	6.91	-12.65	-13.68	1.03	-6.59	-7.00	0.40	-3.48	-3.65	0.17	-2.40	-2.51	0.11	-1.25	-1.29	0.05
26-1C(w)	2000	######	######	18.75	-17.89	-20.61	2.72	-8.69	-9.78	1.10	-4.43	-4.90	0.47	-3.02	-3.30	0.28	-1.55	-1.66	0.11
26-1B(w)	3000	######	######	-63.62	-14.74	-24.50	9.76	-6.17	-10.85	4.67	-2.93	-5.04	2.11	-1.95	-3.22	1.27	-0.97	-1.43	0.46
26-1A(r)	50000	-89.27	-9.68	-79.59	-86.72	-12.36	-74.36	-44.57	-11.44	-33.13	-34.60	-9.87	-24.72	-28.00	-8.71	-19.29	-8.21	-6.13	-2.08

Figure A-2 Comparison of Rayleigh and Mie backscatter coefficients.

Cloud	Dmax	94 GHz (dB)			35 GHz (dB)			24 GHz (dB)			17 GHz (dB)			14 GHz (dB)			10 GHz (dB)		
Type	(um)	Ray	Mie	Δ	Ray	Mie	Δ	Ray	Mie	Δ	Ray	Mie	Δ	Ray	Mie	Δ	Ray	Mie	Δ
1-A-1(i)	1000	-56.6	-56.9	0.2	-73.8	-73.8	0.0	-80.3	-80.4	0.0	-86.3	-86.4	0.0	-89.7	-89.7	0.0	-95.5	-95.6	0.0
1-M-1(i)	1000	-56.6	-56.9	0.2	-73.8	-73.8	0.0	-80.3	-80.4	0.0	-86.3	-86.4	0.0	-89.7	-89.7	0.0	-95.5	-95.6	0.0
1-T-1(i)	1000	-56.6	-56.9	0.2	-73.8	-73.8	0.0	-80.3	-80.4	0.0	-86.3	-86.4	0.0	-89.7	-89.7	0.0	-95.5	-95.6	0.0
10-1(w)	200	-67.2	-67.2	0.0	-83.2	-83.2	0.0	-89.6	-89.6	0.0	-95.5	-95.5	0.0	-98.9	-98.9	0.0	-104.7	-104.7	0.0
14-1(w)	200	-75.5	-75.6	0.0	-91.5	-91.6	0.0	-98.0	-98.0	0.0	-103.9	-103.9	0.0	-107.2	-107.3	0.0	-113.1	-113.1	0.0
20-1(w)	200	-72.7	-72.7	0.0	-89.2	-89.2	0.0	-95.7	-95.7	0.0	-101.7	-101.7	0.0	-105.0	-105.0	0.0	-110.9	-110.9	0.0
20-2(w)	200	-72.7	-72.7	0.0	-89.2	-89.2	0.0	-95.7	-95.7	0.0	-101.7	-101.7	0.0	-105.0	-105.0	0.0	-110.8	-110.9	0.0
21-1C(w)	200	-58.5	-58.5	0.0	-74.8	-74.9	0.0	-81.3	-81.3	0.0	-87.3	-87.3	0.0	-90.6	-90.6	0.0	-96.5	-96.5	0.0
21-1B(w)	200	-55.3	-55.3	0.0	-71.8	-71.8	0.0	-78.3	-78.3	0.0	-84.3	-84.3	0.0	-87.6	-87.6	0.0	-93.4	-93.5	0.0
21-1A(r)	400	-49.1	-49.1	0.0	-65.7	-65.7	0.0	-72.2	-72.2	0.0	-78.2	-78.2	0.0	-81.5	-81.5	0.0	-87.4	-87.4	0.0
21-2D(w)	200	-58.5	-58.5	0.0	-74.8	-74.9	0.0	-81.3	-81.3	0.0	-87.3	-87.3	0.0	-90.6	-90.6	0.0	-96.5	-96.5	0.0
21-2C(w)	200	-55.3	-55.3	0.0	-71.8	-71.8	0.0	-78.3	-78.3	0.0	-84.3	-84.3	0.0	-87.6	-87.6	0.0	-93.4	-93.5	0.0
21-2B(w)	200	-58.3	-58.3	0.0	-74.8	-74.8	0.0	-81.3	-81.3	0.0	-87.3	-87.3	0.0	-90.6	-90.6	0.0	-96.5	-96.5	0.0
21-2A(r)	4000	-23.9	-36.1	12.2	-40.5	-40.5	0.1	-47.0	-45.7	-1.3	-52.9	-51.6	-1.3	-56.3	-55.3	-1.0	-62.1	-62.0	-0.2
21-3D(w)	200	-56.1	-56.1	0.0	-72.0	-72.0	0.0	-78.4	-78.4	0.0	-84.3	-84.3	0.0	-87.6	-87.6	0.0	-93.4	-93.5	0.0
21-3C(w)	200	-53.8	-53.8	0.0	-70.1	-70.1	0.0	-76.5	-76.6	0.0	-82.5	-82.5	0.0	-85.9	-85.9	0.0	-91.7	-91.7	0.0
21-3B(w)	200	-55.3	-55.3	0.0	-71.8	-71.8	0.0	-78.3	-78.3	0.0	-84.3	-84.3	0.0	-87.6	-87.6	0.0	-93.4	-93.5	0.0
21-3A(r)	4000	-16.9	-29.1	12.2	-33.5	-33.6	0.1	-40.0	-38.7	-1.3	-45.9	-44.6	-1.3	-49.3	-48.3	-1.0	-55.1	-55.0	-0.2
22-1(w)	200	-64.3	-64.3	0.0	-80.8	-80.9	0.0	-87.3	-87.3	0.0	-93.3	-93.3	0.0	-96.6	-96.7	0.0	-102.5	-102.5	0.0
22-2(w)	200	-64.4	-64.4	0.0	-80.9	-80.9	0.0	-87.3	-87.3	0.0	-93.3	-93.3	0.0	-96.6	-96.7	0.0	-102.5	-102.5	0.0
25-1C(w)	200	-61.6	-61.6	0.0	-77.9	-77.9	0.0	-84.3	-84.4	0.0	-90.3	-90.3	0.0	-93.6	-93.7	0.0	-99.5	-99.5	0.0
25-1B(w)	200	-58.5	-58.5	0.0	-74.8	-74.9	0.0	-81.3	-81.3	0.0	-87.3	-87.3	0.0	-90.6	-90.6	0.0	-96.5	-96.5	0.0
25-1A(w)	200	-61.4	-61.4	0.0	-77.8	-77.8	0.0	-84.3	-84.3	0.0	-90.3	-90.3	0.0	-93.6	-93.7	0.0	-99.5	-99.5	0.0
25-2C(w)	4000	-21.4	-28.5	7.1	-37.6	-37.9	0.3	-44.0	-43.4	-0.6	-49.9	-49.2	-0.7	-53.3	-52.7	-0.6	-59.1	-58.9	-0.3
25-2B(w)	4000	-24.0	-30.9	6.9	-40.5	-40.6	0.1	-47.0	-46.3	-0.7	-52.9	-52.1	-0.8	-56.3	-55.6	-0.7	-62.1	-61.9	-0.3
25-2A(r)	6000	-17.9	-43.5	25.6	-34.4	-41.2	6.8	-40.9	-43.1	2.1	-46.9	-46.4	-0.5	-50.3	-48.9	-1.3	-56.1	-54.2	-1.9
25-3C(w)	2000	-27.5	-30.0	2.5	-43.5	-43.2	-0.3	-49.9	-49.7	-0.3	-55.9	-55.7	-0.1	-59.2	-59.2	0.0	-65.1	-65.1	0.1
25-3B(w)	3000	-21.0	-27.9	6.8	-37.5	-37.6	0.1	-44.0	-43.3	-0.7	-49.9	-49.1	-0.8	-53.3	-52.6	-0.7	-59.1	-58.9	-0.3
25-3A(r)	6000	-10.9	-36.5	25.6	-27.4	-34.2	6.7	-33.9	-36.1	2.1	-39.9	-39.4	-0.5	-43.3	-41.9	-1.4	-49.1	-47.2	-1.9

25-4E(w)	2000	-37.8	-39.1	1.2	-53.8	-53.6	-0.2	-60.2	-60.2	-0.1	-66.1	-66.2	0.0	-69.5	-69.5	0.1	-75.3	-75.4	0.1
25-4D(w)	2000	-34.6	-35.8	1.1	-50.8	-50.5	-0.2	-57.2	-57.1	-0.1	-63.1	-63.2	0.0	-66.5	-66.5	0.1	-72.3	-72.4	0.1
25-4C(w)	2000	-35.4	-36.6	0.0	-51.7	-51.4	-0.3	-58.1	-58.1	-0.1	-64.1	-64.1	0.1	-67.4	-67.5	0.1	-73.3	-73.4	0.1
25-4B(w)	1000	-49.0	-49.0	0.0	-65.4	-65.4	0.0	-71.8	-71.9	0.0	-77.8	-77.8	0.0	-81.2	-81.2	0.0	-87.0	-87.0	0.0
25-4A(w)	200	-63.7	-63.7	0.2	-80.1	-80.1	0.0	-86.5	-86.6	0.0	-92.5	-92.5	0.0	-95.9	-95.9	0.0	-101.7	-101.7	0.0
26-1F(i)	1000	-53.6	-53.9	3.0	-70.8	-70.8	0.0	-77.3	-77.4	0.0	-83.3	-83.4	0.0	-86.7	-86.7	0.0	-92.5	-92.6	0.0
26-1E(w)	2000	-30.5	-33.6	2.9	-45.6	-45.7	0.1	-51.6	-51.5	-0.1	-57.4	-57.3	-0.1	-60.6	-60.6	-0.1	-66.4	-66.4	0.0
26-1D(w)	2000	-28.5	-31.4	2.5	-43.9	-43.8	-0.1	-50.1	-49.9	-0.2	-56.0	-55.8	-0.1	-59.3	-59.2	-0.1	-65.1	-65.1	0.0
26-1C(w)	2000	-24.5	-27.0	6.8	-40.5	-40.2	-0.3	-46.9	-46.6	-0.3	-52.9	-52.7	-0.1	-56.2	-56.2	0.0	-62.0	-62.1	0.1
26-1B(w)	3000	-15.6	-22.4	39.9	-32.1	-32.2	0.1	-38.5	-37.8	-0.7	-44.5	-43.6	-0.8	-47.9	-47.2	-0.7	-53.7	-53.4	-0.3
26-1A(r)	50000	5.0	-34.9	39.9	-11.5	-33.2	21.7	-18.0	-32.2	14.2	-24.0	-31.8	7.8	-27.4	-31.5	4.1	-33.2	-32.7	-0.5

Figure A-1 Mie SNR for Deirmendjian cloud model: 1-A-1, Cirrostratus

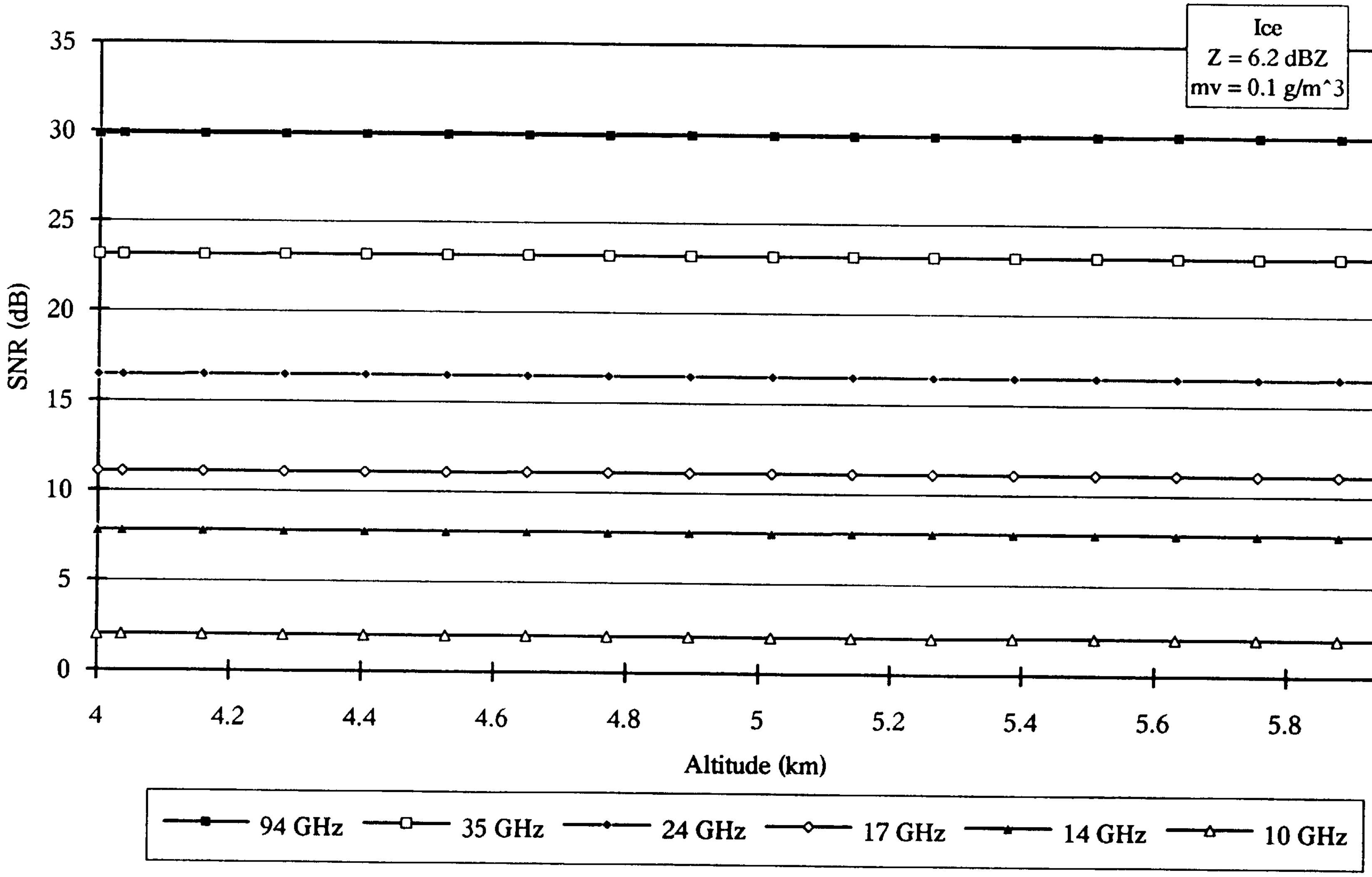

Figure A-2 Mie SNR for Deirmendjian cloud model: 1-M-1, Cirrostratus

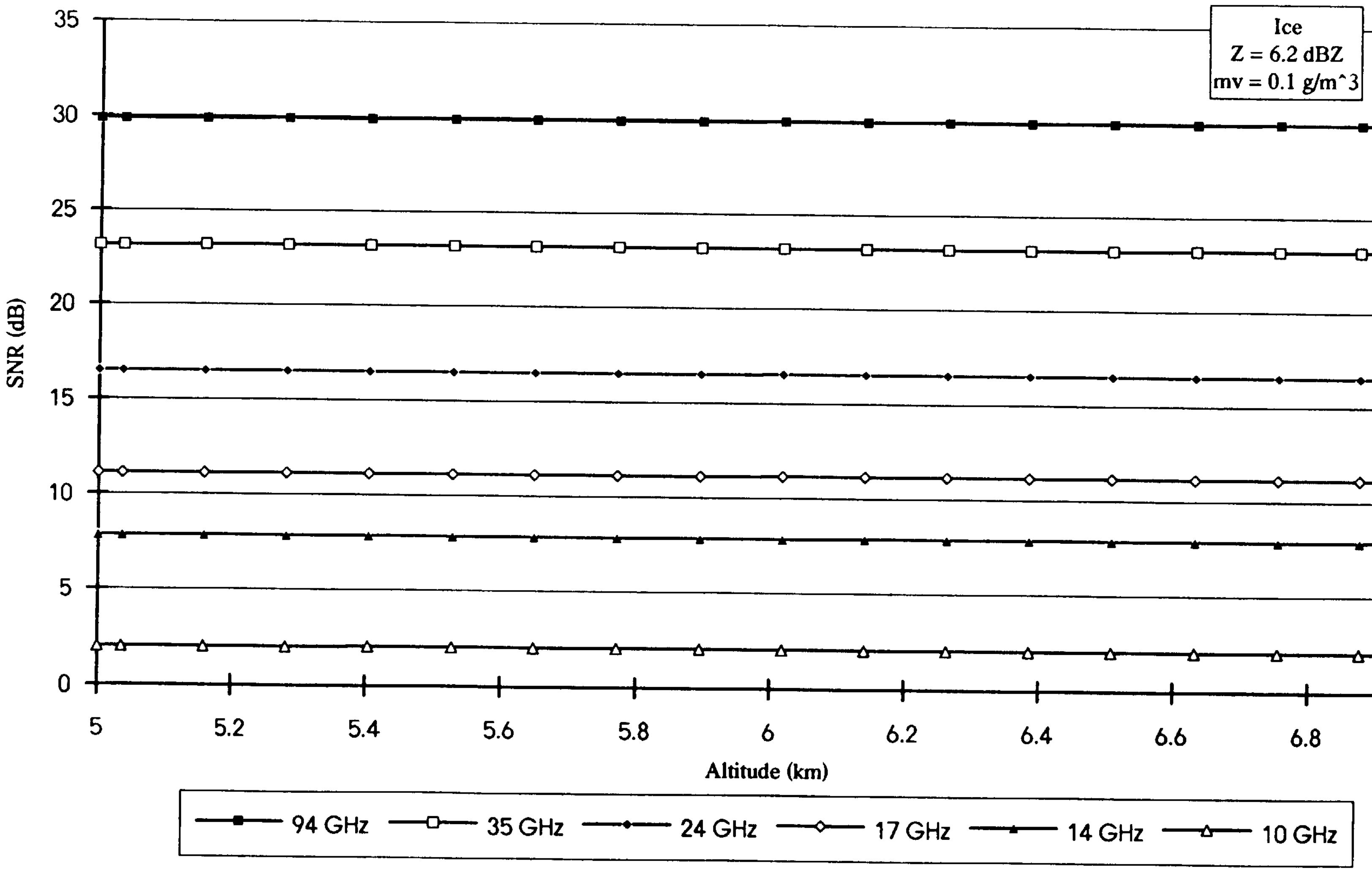

Figure A-3 Mie SNR for Deirmendjian cloud model: 1-T-1, Cirrostratus

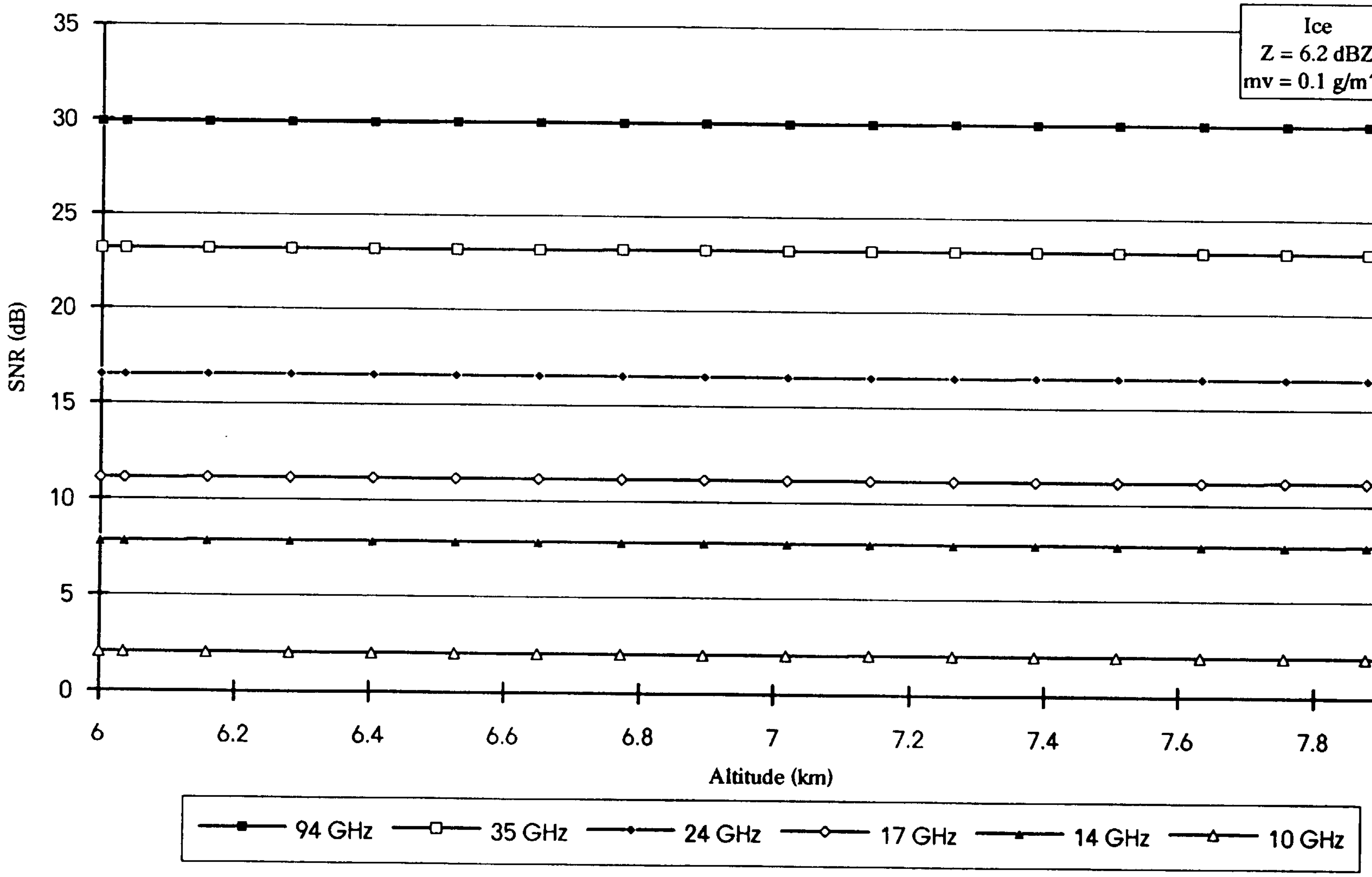

Figure A-4 Mie SNR for Deirmendjian cloud model: 10-1, Altocumulus

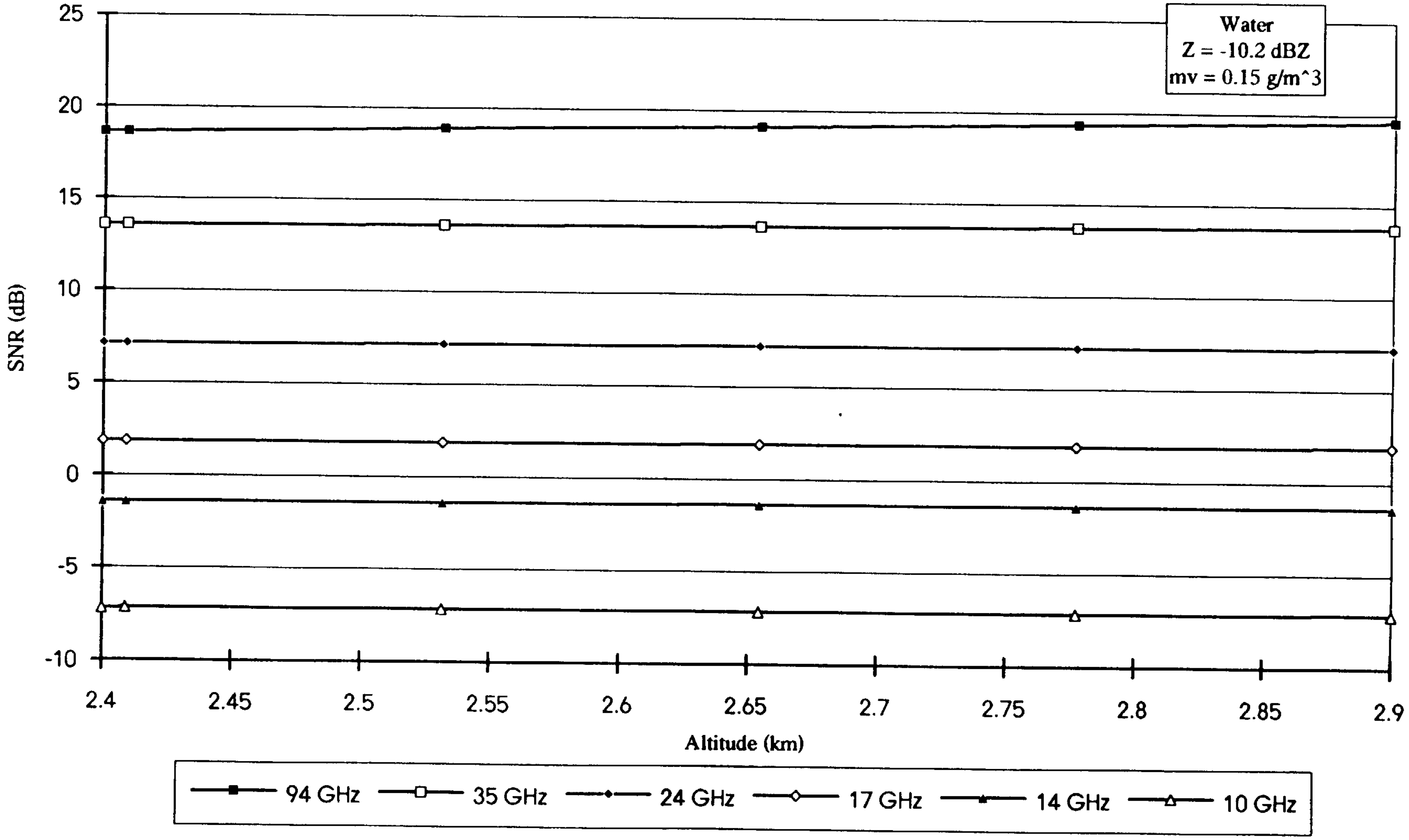

Figure A-5 Mie SNR for Deirmendjian cloud model: 14-1, Altocumulus

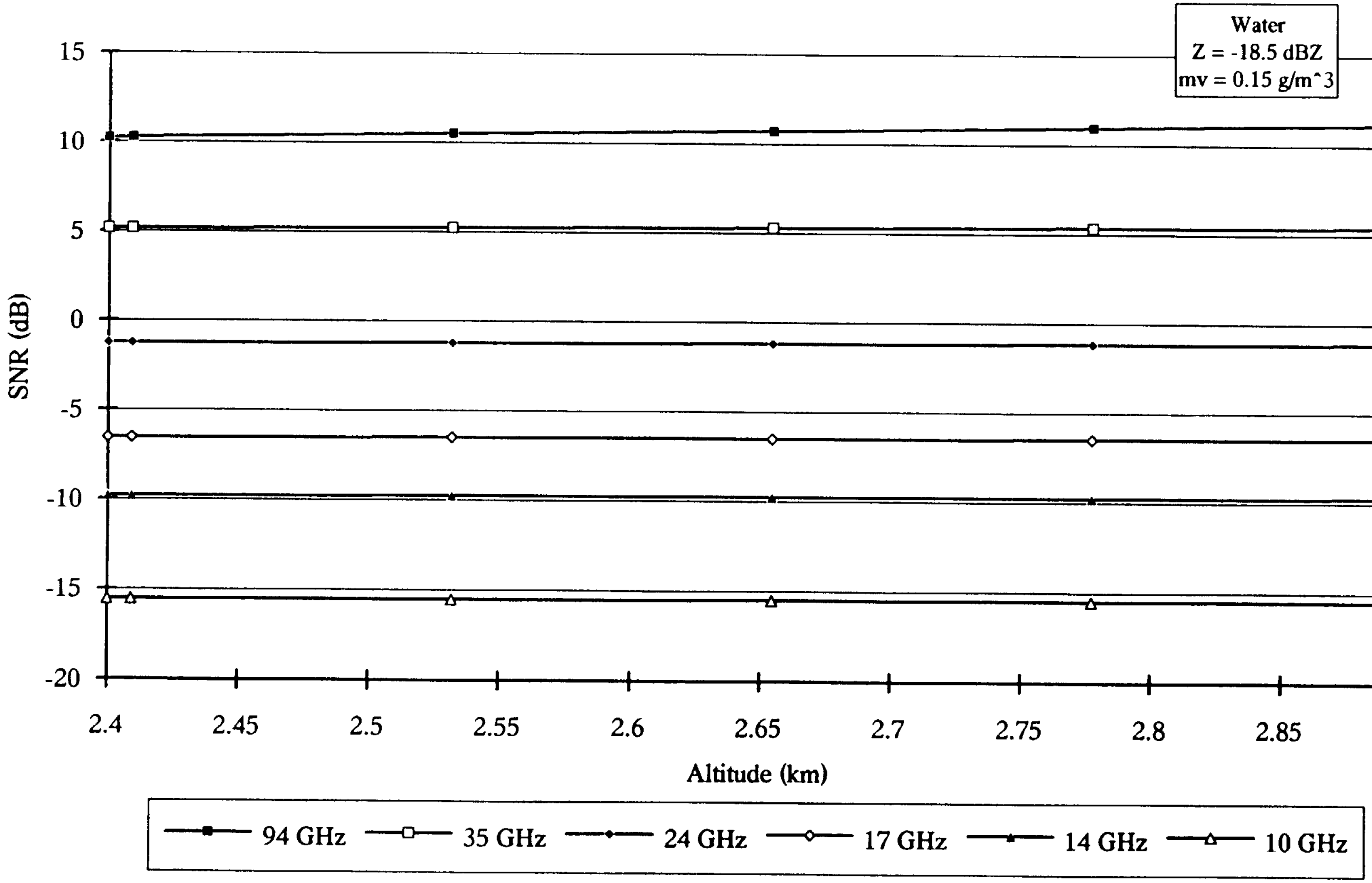

Figure A-6 Mie SNR for Deirmendjian cloud model: 20-1, Low-Lying Stratus

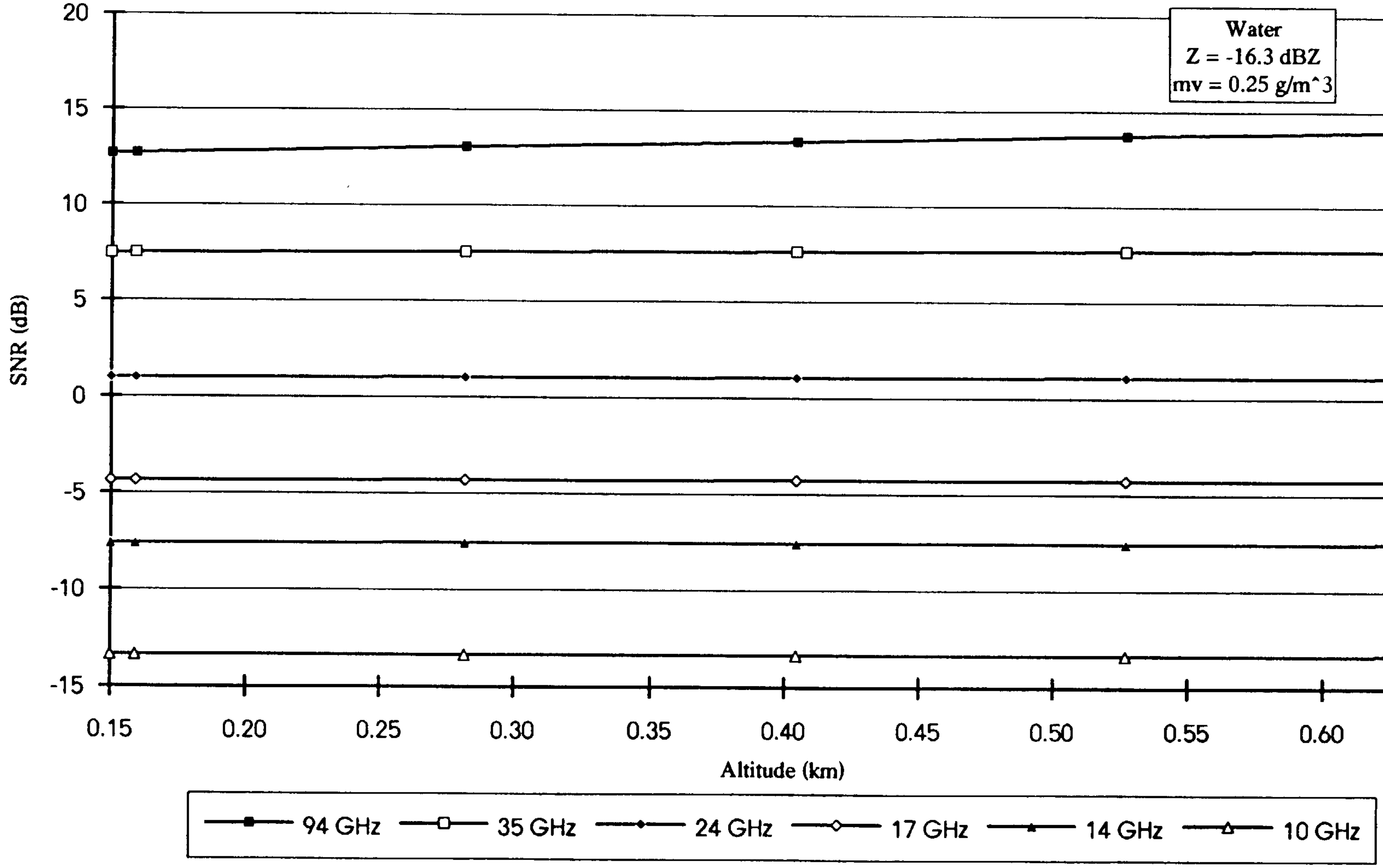

Figure A-7 Mie SNR for Deirmendjian cloud model: Low-Lying Stratus

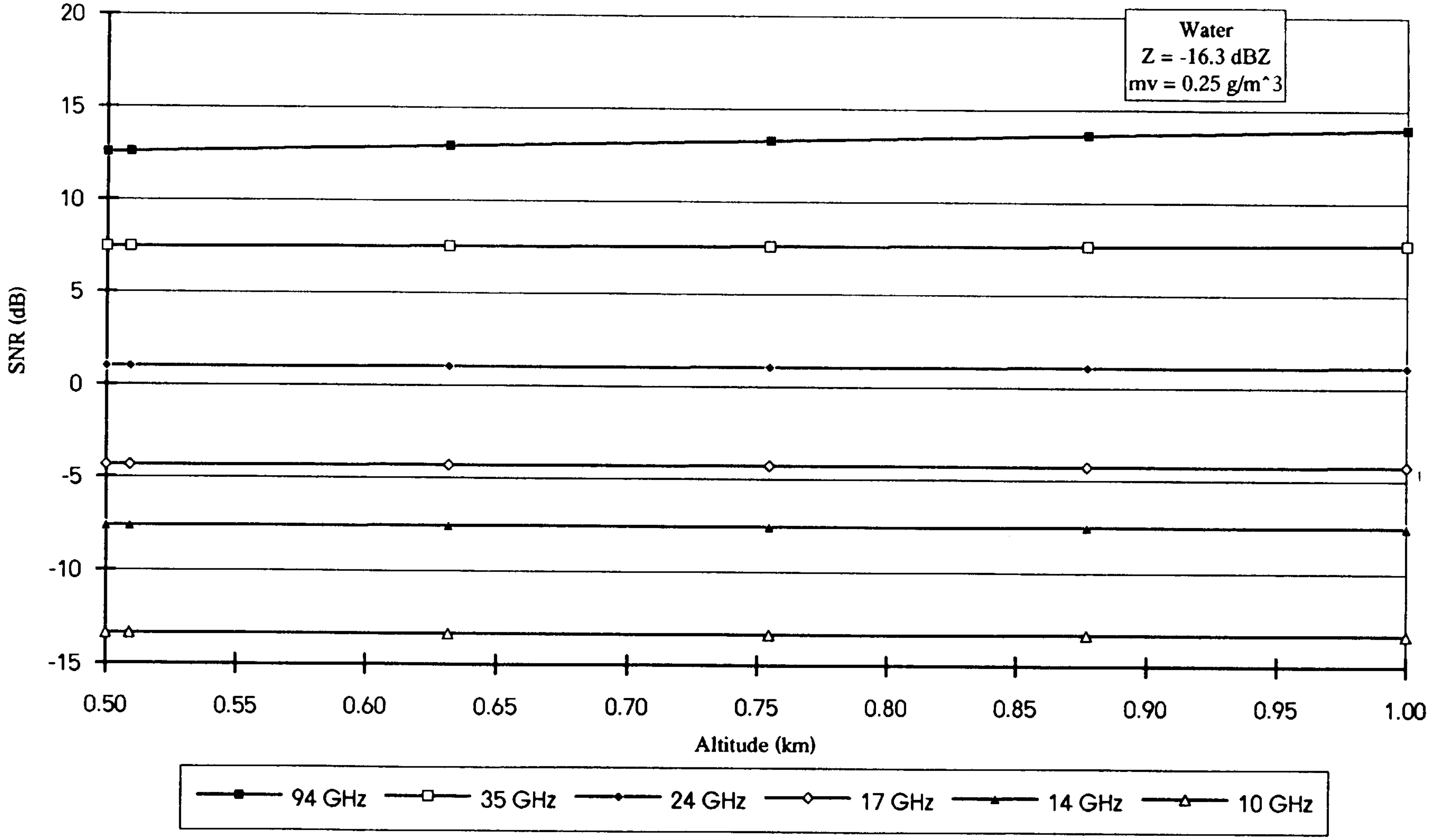

Figure A-8 Mie SNR for Deirmendjian cloud model: 21-1, Drizzle, 0.2 mm/hr

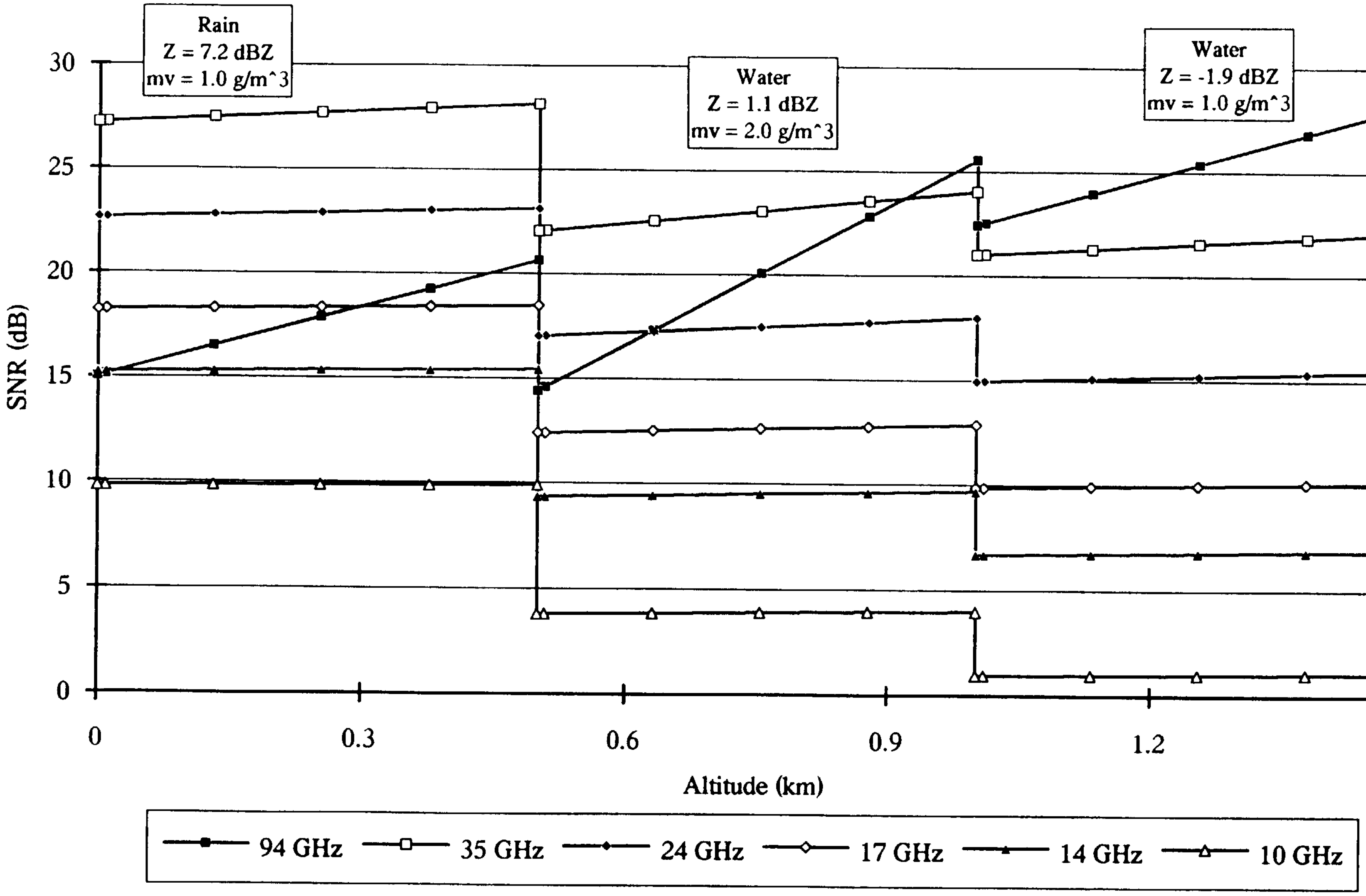

Figure A-9 Mie SNR for Deirmendjian cloud model: 21-2, Steady Rain, 3 mm/hr

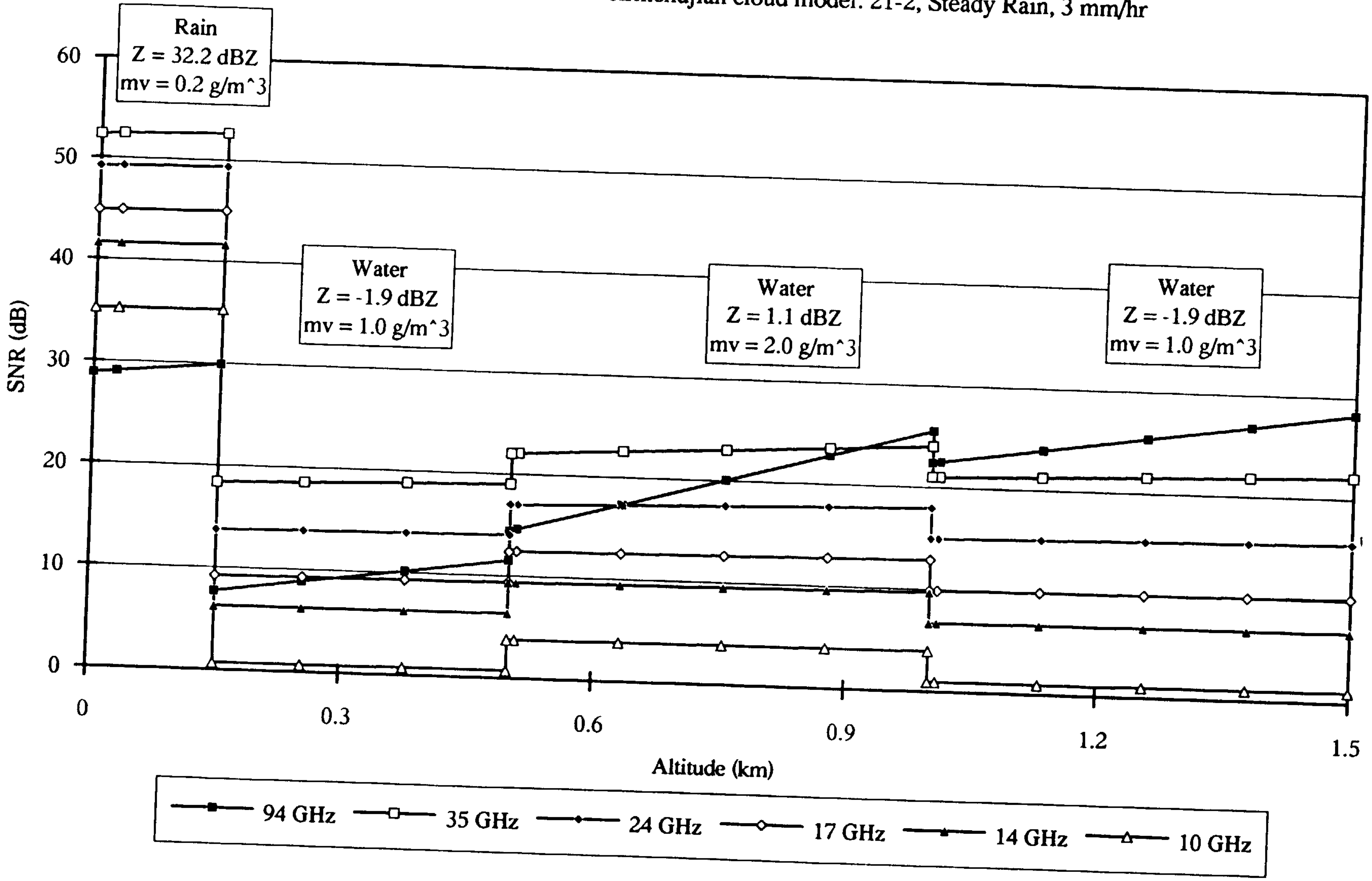

Figure A-10 Mie SNR for Deirmendjian cloud model: 21-3, Steady Rain, 15 mm/hr

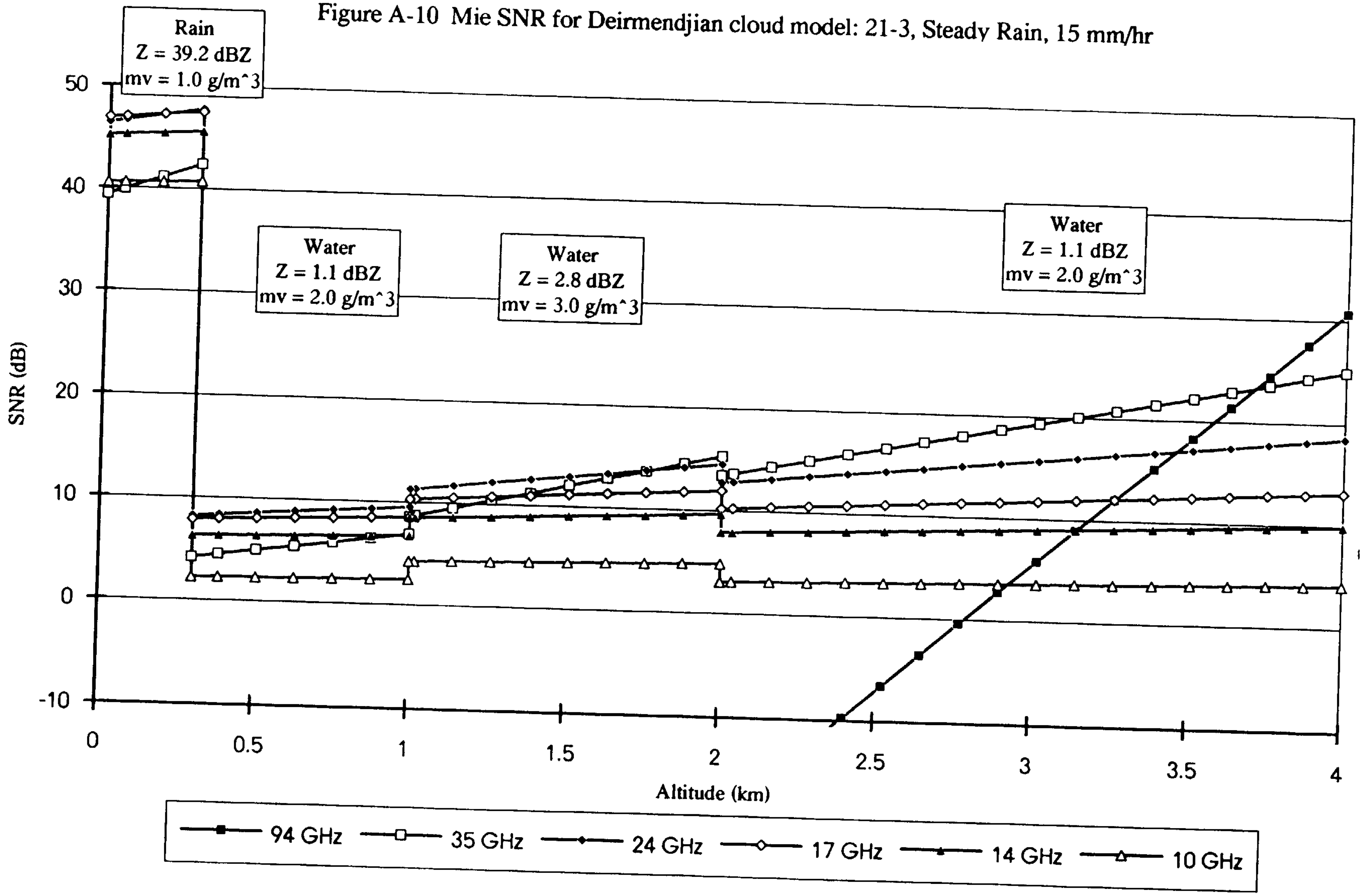

Figure A-11 Mie SNR for Deirmendjian cloud model: 22-1, Stratocumulus

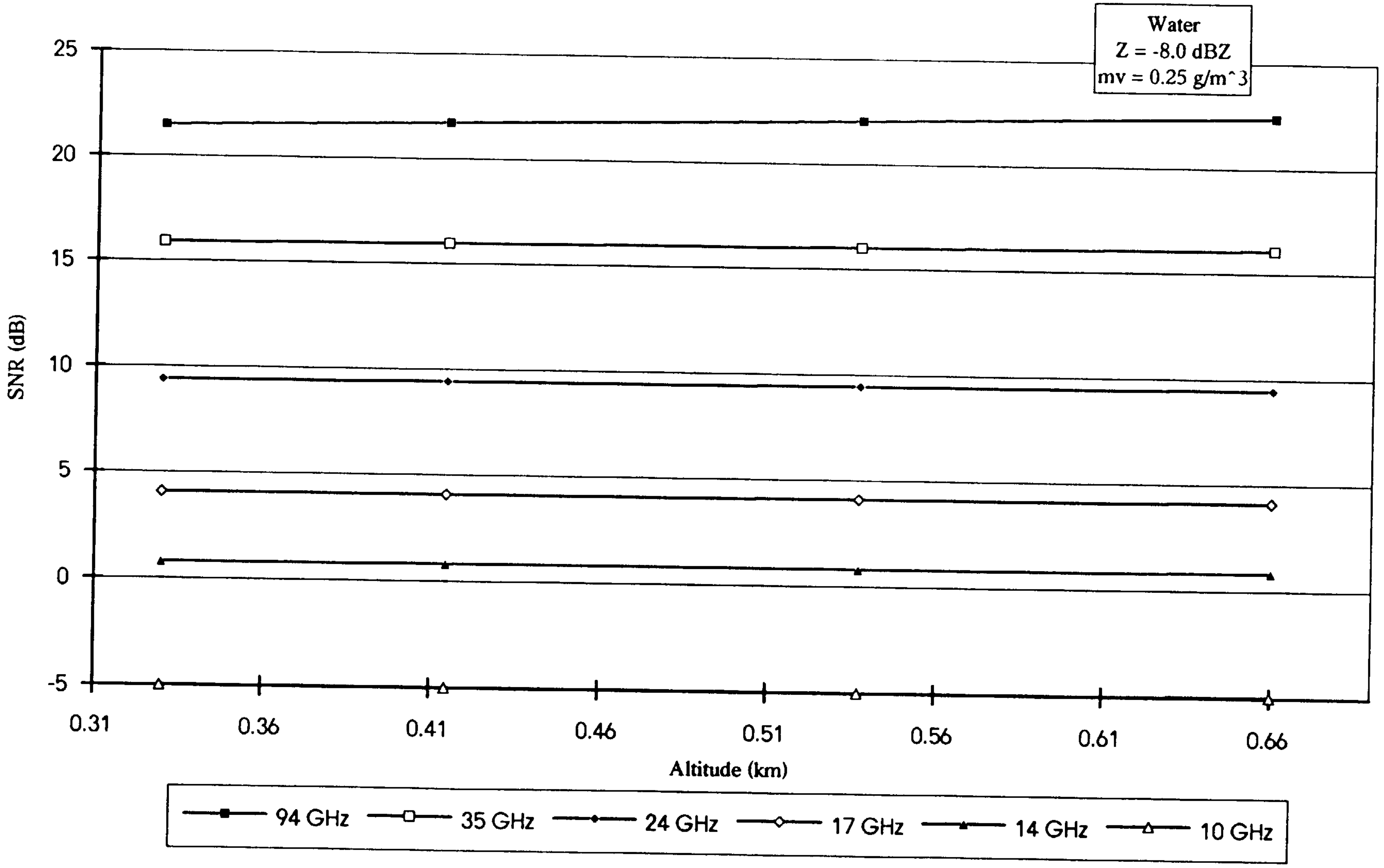

Figure A-12 Mie SNR for Deirmendjian cloud model: 22-2, Stratocumulus

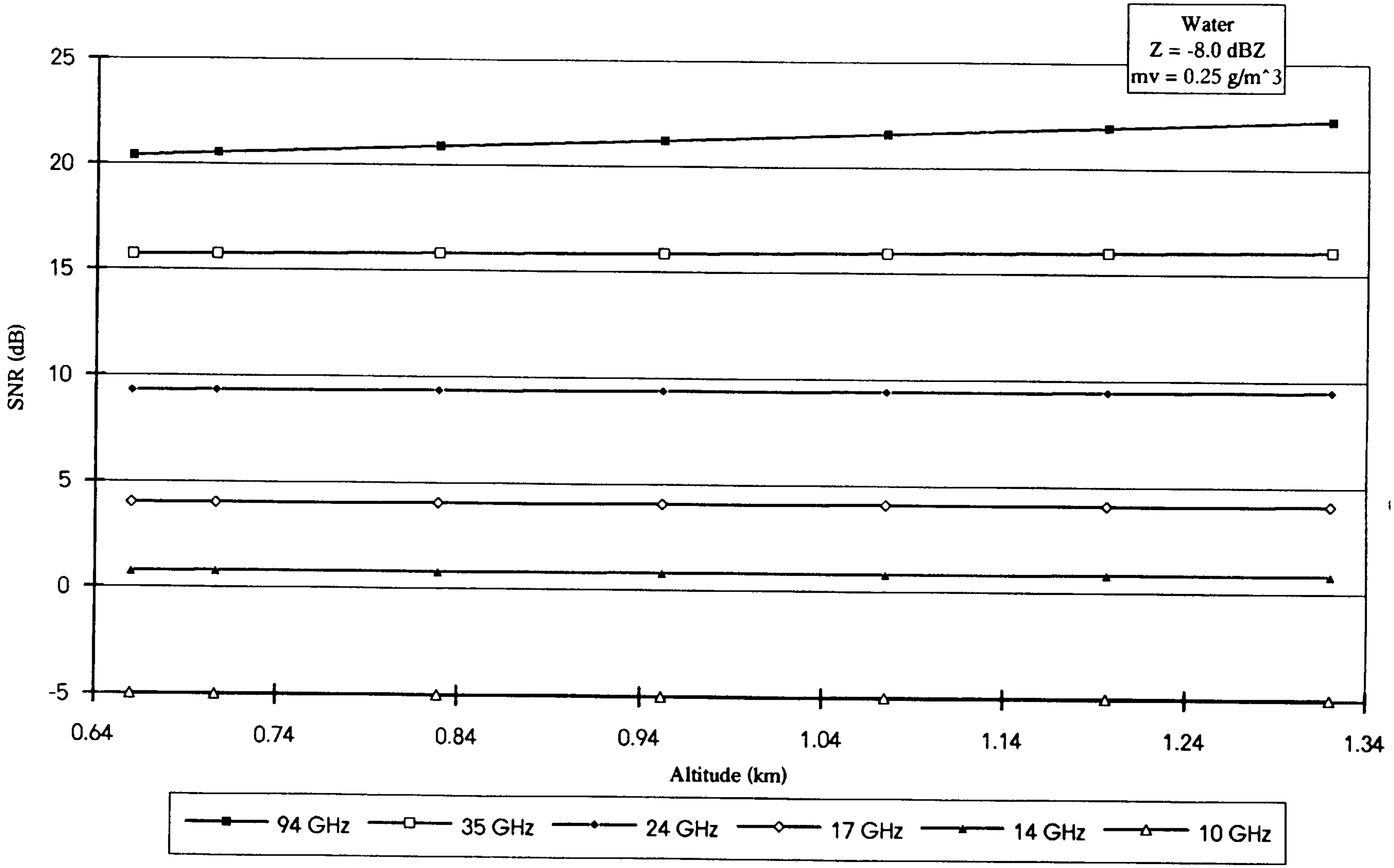

Figure A-13 Mie SNR for Deirmendjian cloud model: 25-1, Fair Weather Cumulus

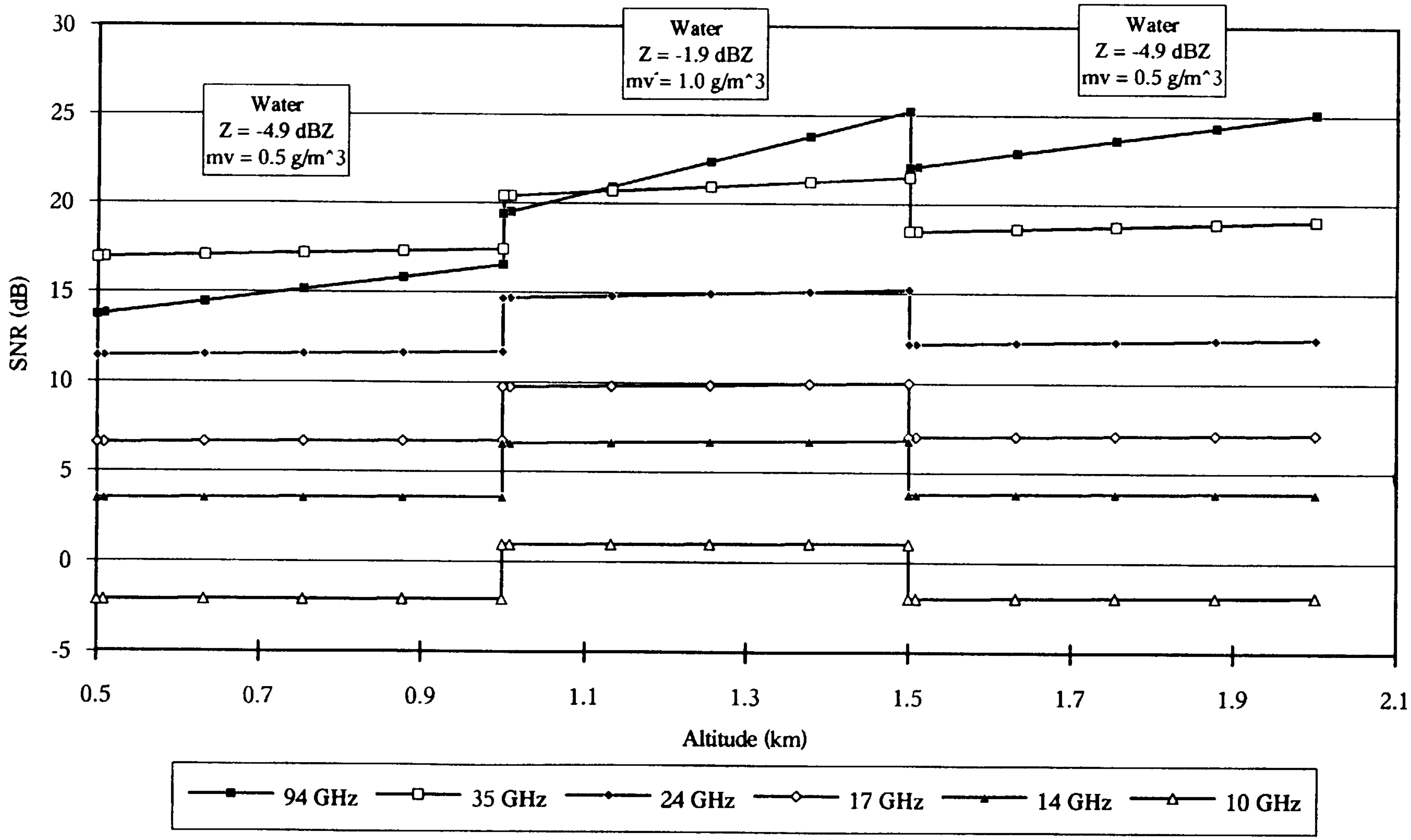

Figure A-14 Mie SNR for Deirmendjian cloud model: 25-2, Cumulus, 2.4 mm/hr

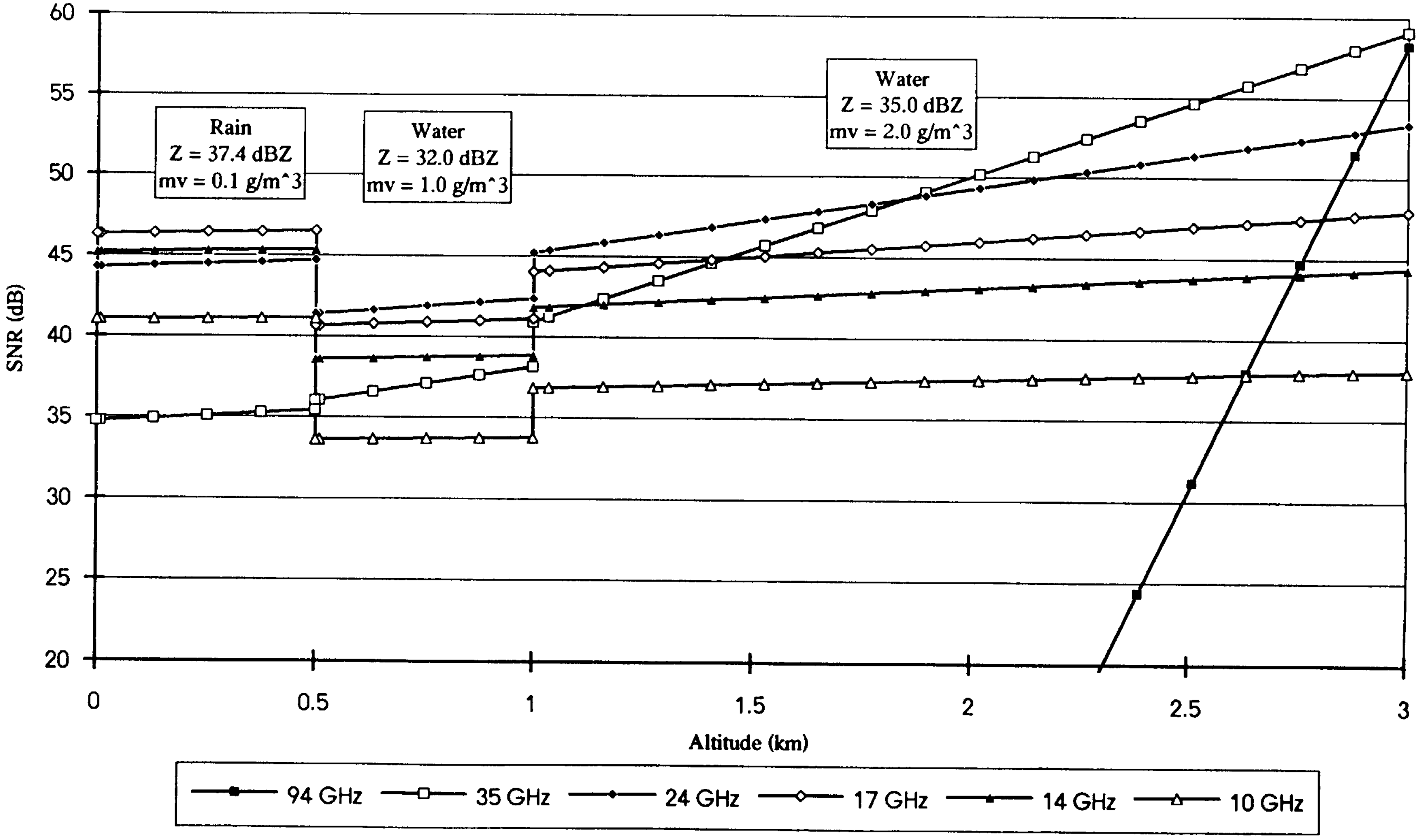

Figure A-15 Mie SNR for Deirmendjian cloud model: 25-3, Cumulus, 12 mm/hr

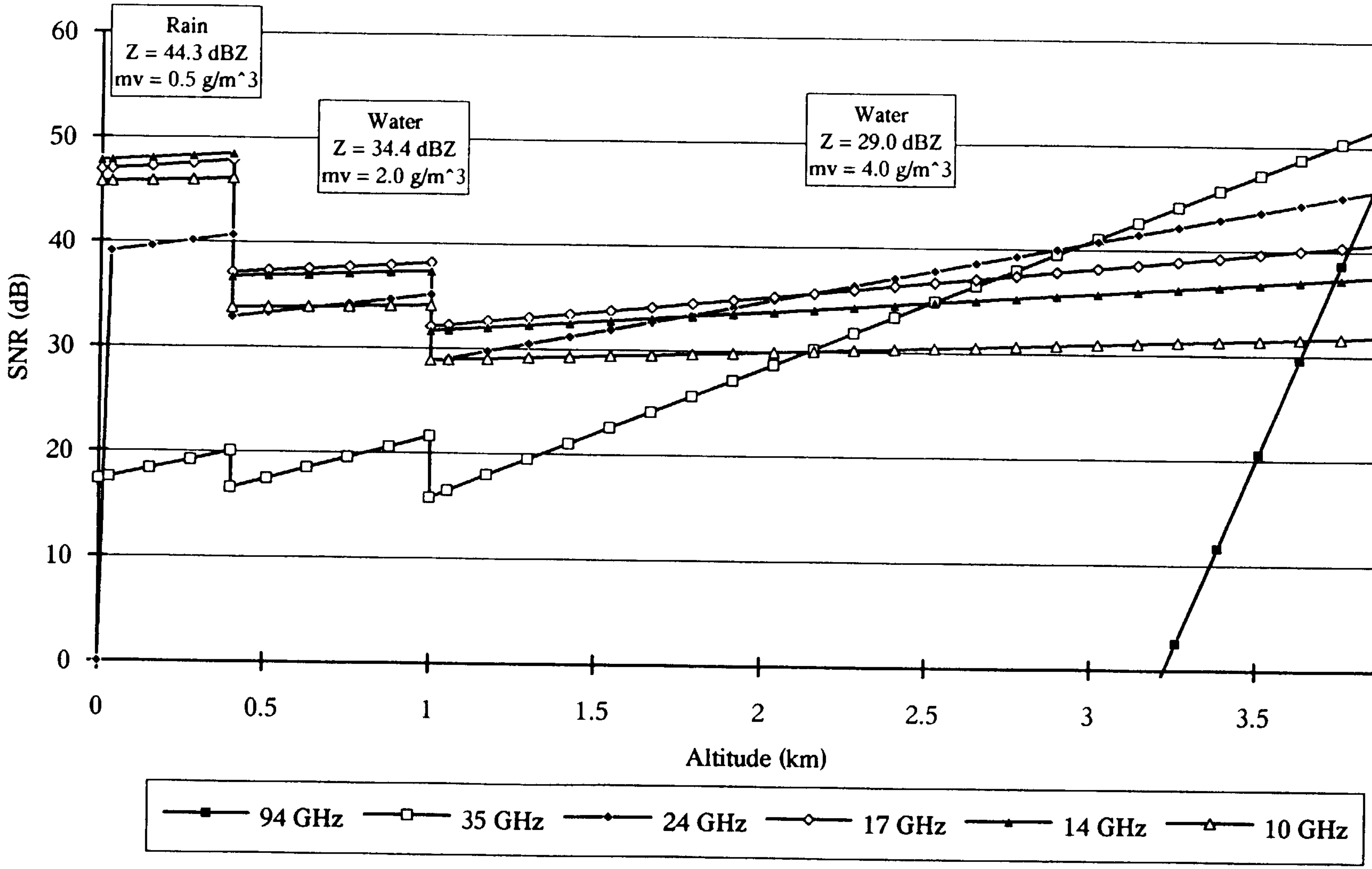

Figure A-16 Mie SNR for Deirmendjian cloud model: 25-4, Cumulus Congestus

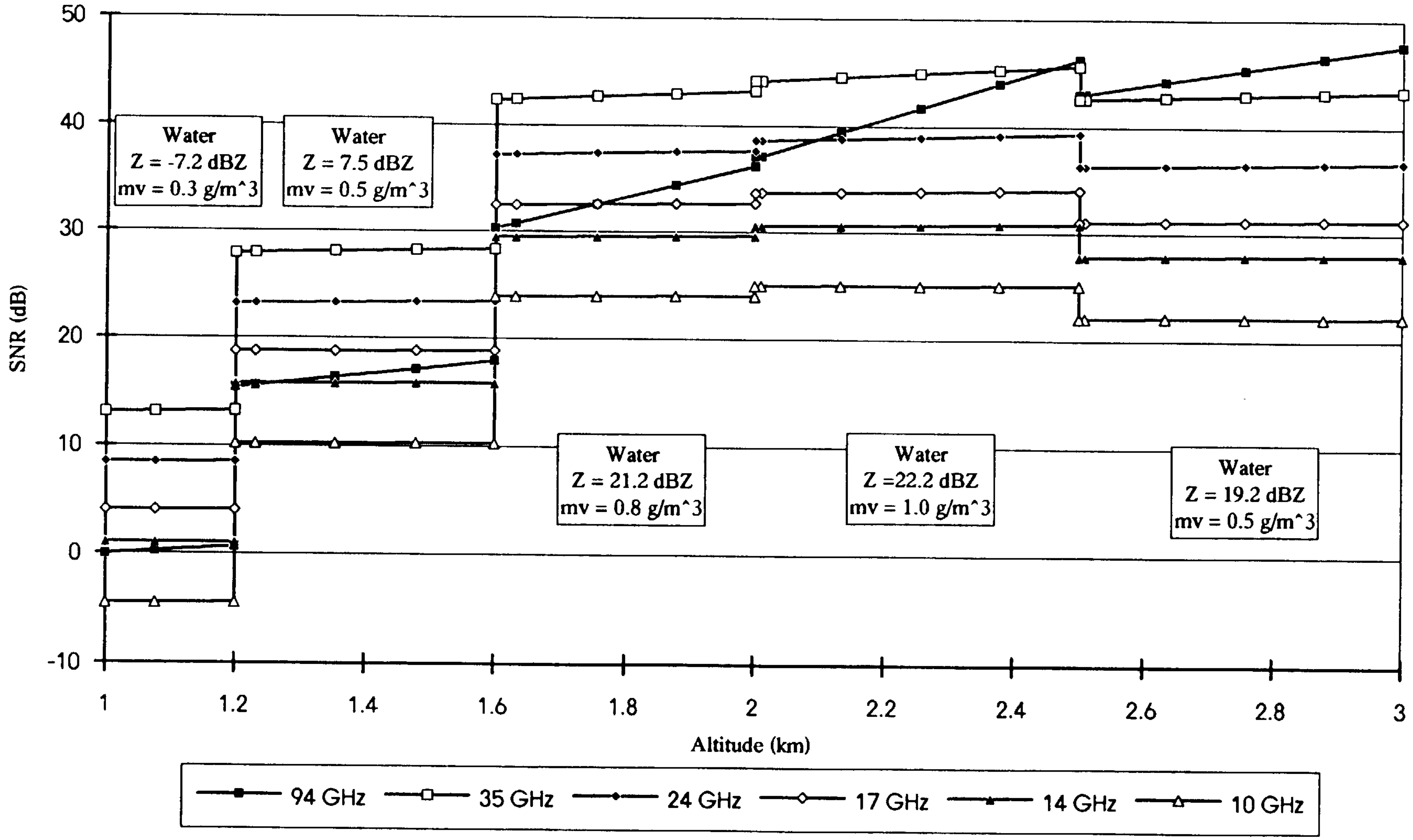

Figure A-17 Mie SNR for Deirmendjian cloud model: 26-1, Cumulonimbus, 150 mm/hr

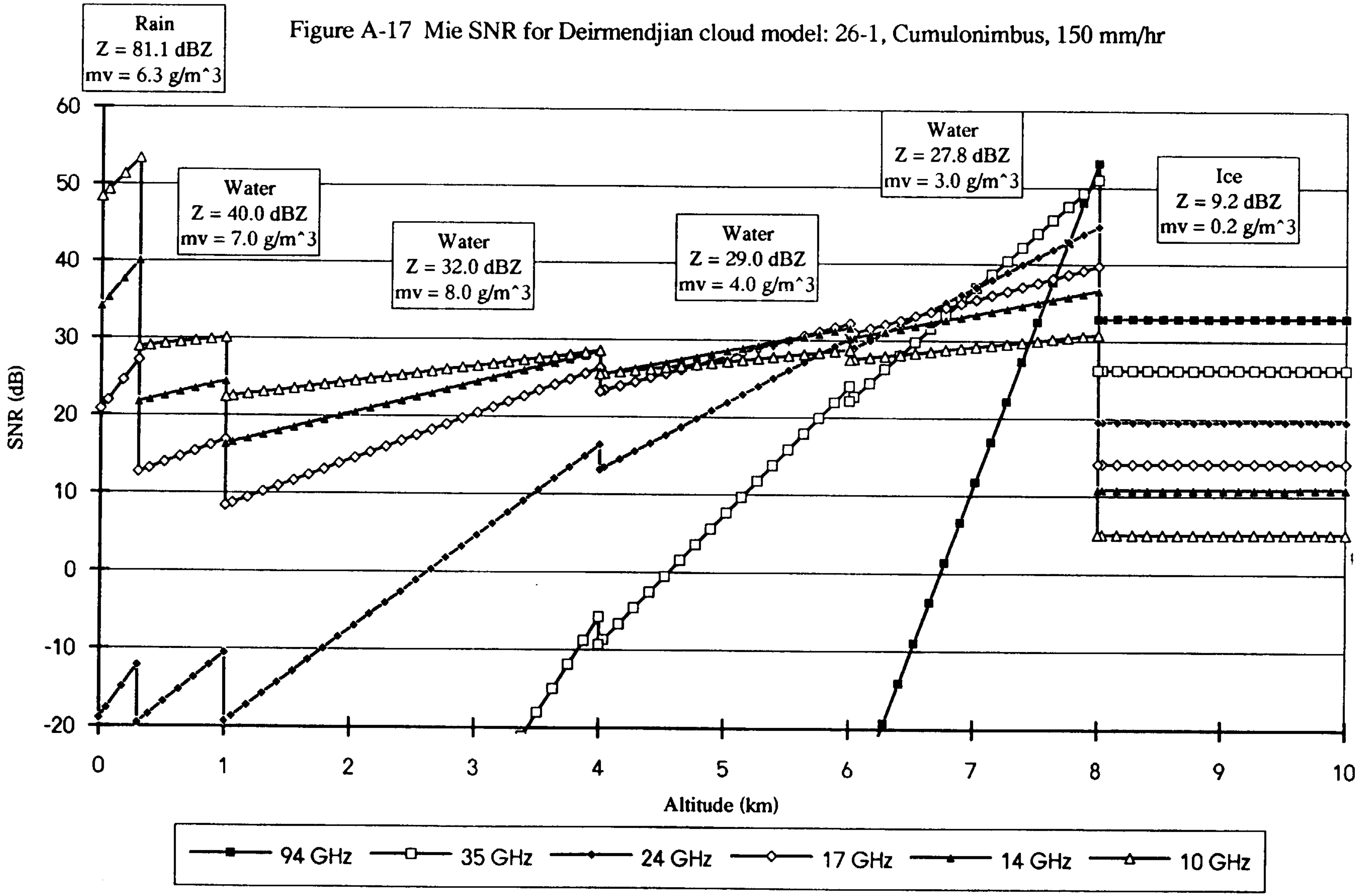

REFERENCES

Atlas, D., and Bartnoff, S., "Cloud Visibility, Radar Reflectivity, and Drop-Size Distribution," *Journal of Meteorology,* vol. 10, p. 143-148, April 1953.

Atlas, D., "The Estimation of Cloud Parameters by Radar," *Journal of Meteorology,* vol. 11, p. 309-317, August 1954.

Atlas, D., "Advances in Radar Meteorology," *Advances in Geophysics,* Landsgerg and Mieghem, eds., Academic Press, p. 488, 1964.

Baker, W.E., and Curran, R.J., eds., *Report of the NASA Workshop on Global Wind Measurements,* STC2081, A. Deepak Publishing, Hampton, VA, 1985.

Battan, L.J., *Radar Observation of the Atmosphere,* University of Chicago Press, Chicago, Illinois, 1973.

Best, A.C., "The Size Distribution of Raindrops," *Quart. J. Roy. Meteor. Soc.,* vol. 76, p. 16-36, 1950.

Breed, D.W., L.O Grant, and J. Dye, "Cloud Droplet Distribution in High Elevation Continental Cumulis," *Proc. Intern. Conf. on Cloud Physics,* Boulder, Colorado, p. 658-664, 1976.

Boucher, R.J., "Empirical Relationship Between Radar Reflectivity, Drop Size Distribution, and Liquid Water Content in Clouds," Mt. Washington Observ., Final Rep. under Contract AF19(122)-399, June 1952.

Chahine, M.T., D.J. McCleese, P.W. Rosnkranz, and D.H. Staelin, *Manual of Remote Sensing,* R.N. Colwell, ed., vol.I, 2ed., Chapter 5, American Society of Photogrammetry, 1983.

Curran, R.J., ed., *Earth Observation System Instrument Panel Report: LAWS Laser Atmospheric Wind Sounder,* vol. IIg, NASA, Washington DC, 1987.

Diem, M., "Messung der Grösse von Wolken-elementen II," *Meteor. Rundschau,* vol. 1, p.261-273, 1948.

Deirmendjian, D., "Scattering and Polarization Properties of Water Clouds and Hazes in the Visible and Infrared," *Applied Optics,* vol. 3, no. 2, p. 187-196, 1964.

Deirmendjian, D., *Electromagnetic Scattering on Spherical Polydispersions,* Chapter 3, American Elsevier Publishing Company, Inc., New York, 1969.

Doviak, R.J., D. Sirmans, D. Zrnic, G.B. Walker, "Considerations for Pulse-Doppler Radar Observations of Severe Thunderstorms," *Journal of Applied Meteorology,* vol. 17, p. 189-205, 1978.

Doviak, R.J., Zrnic, D.S., *Doppler Radar and Weather Observations,* Academic Press, Inc., New York, 1984.

Fraser, K.S., N.E. Gaut, E.C. Reifenstein, II, and H. Sievering, "Interaction Mechanisms - Within the Atmosphere," *Manual of Remote Sensing,* R.G. Reeves, ed., American Society of Photogrammetry, Falls Church, Virginia, Chapter 5, 1975.

Gossard, E.E., R.G. Strauch, *Radar Observation of Clear Air and Clouds,* Elsevier Science Publishers Company, Inc., New York, 1983.

Gossard, E.E., R.G. Strauch, D.C. Welsh, S.Y. Matrosov, "Cloud Layers, Particle Identification, and Rain-Rate Profiles from *ZRV* Measurements by Clear-Air Doppler Radars," *Journal of Atmospheric and Oceanic Technology,* vol. 9, no. 2, April 1992.

Ippolito, L.J., "A Summary of Propagation Impairments on 10 to 100 GHz Satellite Links with Techniques for System Design," *Propagation Effects Handbook for Satellite System Design,* NASA Reference Publication 1082(04), Feb. 1989.

Johnson, R.C., and H. Jasik, *Antenna Engineering Handbook,* 2nd ed., McGraw-Hill Book Company, New York, Chapter 20, 1984.

Kalnay, E., Jusem, J.C., and Pfaendtner, "The relative importance of mass and wind in the present observing system," *Proceedings of the NASA Symposium on Global Wind Measurements,* A. Deepak Publishing, Hampton, VA, 1985.

Kerr, D.E., *Propagation of Short Radio Waves,* Dover Publications, Inc., New York, p. 451-452, 1951.

Kreyszig, E., *Advanced Engineering Mathematics,* 6th ed., John Wiley & Sons, Inc., New York, 1988.

Laws, J.O., and D.A. Parsons, "The Relationship of Raindrop Size to Intensity," *Trans. Am. Geophys. Union,* 24th Annual Meeting, p. 452-460, 1943.

Lhermitte, R.M., "Cloud and Precipitation Remote Sensing at 94 GHz," *IEEE Trans. Geosci. Remote Sensing,* vol. 26, no.3, p. 207-216, 1988.

Marshall, J.S., and W.Mck. Palmer, "The Distribution of Raindrops with Size," *J. Meteorol.*, vol. 5, p. 165-166, 1948.

Mason, B.J., *The Physics of Clouds,* Oxford University Press, Amen House, London, p. 94-95, 1957.

Mie, G., "Beitrage xur Optik truber medien," speziell Koloidaler metalasungen, *Ann. Physik,* vol. 25, p. 377, 1908.

Meneghini, R., T. Kozu, *Spaceborne Weather Radar,* Artech House, Norwood, Massachusetts, 1990.

Reifenstein, E.C., III, and N.E. Gaut, "Microwave Properties of Clouds in the Spectral Range 30-40 GHz," Tech. Rep. No. 12, Environ. Res. and Tech., Inc.

Sauvageot, H., *Radar Meteorology,* Artech House, Boston, Massachusetts, 1992.

Shanmugan, K.S., and A.M. Breipohl, *Random Signals: Detection, Estimation and Data Analysis,* John Wiley & Sons, New York, 1988.

Sirmans, D. and B. Bumgarner, "Numerical Comparison of Five Mean Frequency Estimators," *Journal of Applied Meteorology,* vol. 14, p. 991-1003, 1975.

Skolnik, M.I., *Introduction to Radar Systems,* 2ed., Chapter 13, McGraw-Hill Book Company, New York, 1980.

Skolnik, M.I., ed., *Radar Handbook,* 2ed., McGraw-Hill Book Company, New York, 1990.

Squires, P., "The Microstructure and Colloidal Stability of Warm Clouds. Part I: The Relationship Between Structure and Stability," *Tellus*, vol. 10, p. 256-261, 1958.

Trabert, W., "Die Extinction des Lichtes in einem Trüben Medium (Sehweite in Wolken)," *Meteor. Z.*, vol. 18, p. 518-525, 1901.

Ulaby, F.T., R.K. Moore, A.K. Fung, *Microwave Remote Sensing,* vol. I, Addison-Wesley Publishing Company, Reading, Massachusetts, 1981.

Ulaby, F.T., R.K. Moore, A.K. Fung, *Microwave Remote Sensing*, vol. III, Addison-Wesley Publishing Company, Reading, Massachusetts, 1986.

Weickmann, H.K., H.J. aufm Kampe, "Trabert's Formula and the Determination of the Water Content in Clouds," *Journal of Meteorology*, vol. 9, p. 167-171, 1952.

Weickmann, H.K., H.J. aufm Kampe, "Physical Properties of Cumulus Clouds," *Journal of Meteorology*, vol. 10, p. 204-211, 1953.

Weizhaung, X., "A Satellite Based Radar Wind Sounder", dissertation, University of Kansas, 1990.

Wexler, R., "Rain Intensities by Radar," *J. Meteorol.*, vol. 5, p. 171, 1948.

Zrnic, D.S, "Spectral Moment Estimate from Correlated Pulse Pairs," *IEEE Trans. on Aerospace and Electronic Systems*, vol. AES-13, no. 4, p. 344-354, 1977.